MULTILAYER FILMS FOR COLOURED GLAZED SOLAR COLLECTORS

INAUGURALDISSERTATION

zur
Erlangung der Würde eines Doktors der Philosophie
vorgelegt der
Philosophisch–Naturwissenschaftlichen Fakultät
der Universität Basel

von

Jamila Boudaden
aus Agadir, Marokko

Basel, 2009

Genehmigt von der Philosophisch-Naturwissenschaftlichen Fakultät auf Antrag von

Prof. Dr. P. Oelhafen
Prof. Dr. E. Meyer

Basel, den 22. April 2008

Prof. Dr. Eberhard Parlow, Dekan

ABSTRACT

In this work a solution to the problem of black colour appearance which dominates the external aspect of buildings covered by solar thermal collectors is proposed. Multilayered thin films on the glass surface, consisting of oxides materials such as SiO_2, Al_2O_3, TiO_2 or a mixture of these oxides were deposited by reactive magnetron sputtering on glass and their optical properties were examined. As the interface between the sputtered layers on glass emerged as important, the interfaces formed between TiO_2 and SiO_2 and between Al_2O_3 and SiO_2 were studied by X-ray photoelectron spectroscopy. The reflectivity of the film on glass system was shown to be a narrow band in the visible region while the rest of the sunlight is transmitted through the glass due to the use of a near zero absorption materials. In addition, the desired colour of the reflected light in the visible range was obtained by adapting the oxide film thicknesses. Such optical properties besides the film's stability as demonstrated in accelerated ageing tests make the coloured glazing aesthetically pleasing and suitable as a cover glass for thermal solar collectors.

Table of contents

General introduction 1

CHAPTER I: Experimental techniques and thin film characterisation

1 Thin film deposition method 7
1.1 Magnetron sputtering 7
1.2 Sputter system 9

2 Photoelectron spectroscopy 10
2.1 Introduction 10
2.2 Principle of photoemission and photoelectron spectroscopy 11
2.3 Electron escape depth 13
2.4 Three-step model versus one-step model 15
2.5 Photoelectron spectroscopy applied to insulating materials 16
2.5.1 Analysis of very thin films 17
2.5.2 Calibration by an internal reference 17
2.5.3 Calibration by an external reference (gold layer) 17
2.5.4 Surface charge neutralisation by an electron beam 17
2.5.5 Analysis of the Auger parameter 18
2.5.6 Parameters insensitive to charging effects 18
2.6 Experimental set-up 19
2.7 Data analysis 21

3 Laser reflectometry 22

4 Spectroscopic ellipsometry 23
4.1 Introduction 23
4.2 Principles of ellipsometry 24
4.3 Ellipsometer 26
4.4 Data analysis 27
4.5 Effective medium approximation 28

5 Total reflectivity and transmission 30

6 Optical properties of multilayer films 31
6.1 Solar reflectivity, solar transmission, visible reflectance 31
6.2 Merit factor 33
6.3 Colour coordinates in CIE Lab system 35

CHAPTER II: TiO_2/SiO_2 - SiO_2/TiO_2 interfaces and TiO_2 – SiO_2 multilayers

1 TiO_2/SiO_2 and SiO_2/TiO_2 interfaces 41
1.1 Introduction 41
1.2 Experimental details 42
1.3 XPS results 43
1.3.1 TiO_2 on SiO_2 43
1.3.2 SiO_2 on TiO_2 46
1.4 Discussion 47
1.4.1 TiO_2 on SiO_2 48
1.4.2 SiO_2 on TiO_2 48
1.5 Conclusion 53

2 TiO_2 – SiO_2 multilayers for coloured glazed solar collectors 54
2.1 Introduction 54
2.2 Thin film deposition 55
2.3 Laser Reflectometry 55
2.4 Ellipsometry 56
2.4.1 Single layers on silicon substrate 57
2.4.2 Multilayers on silicon substrate 59
2.5 Transmission Electron Microscopy 61
2.6 Simulation 62
2.6.1 Solar transmission and visible reflectance 62
2.6.2 Peak position of the reflectivity curves 64
2.7 Experimental realisations and ageing tests 65
2.8 Conclusion 67

CHAPTER III: SiO_2/Al_2O_3 - Al_2O_3/SiO_2 interfaces and Al_2O_3 – SiO_2 multilayers

1 SiO_2/Al_2O_3 and Al_2O_3/SiO_2 interfaces 71
1.1 Introduction 71
1.2 Experimental details 72
1.3 XPS results 73
1.3.1 SiO_2 on Al_2O_3 73
1.3.2 Al_2O_3 on SiO_2 74
1.4 Discussion 75
1.5 Conclusion 78

2 Al_2O_3 – SiO_2 multilayers for coloured glazed solar collectors 78
2.1 Introduction 78
2.2 Experimental details 79
2.3 Optical characterisation 80
2.3.1 Laser Reflectometry 80
2.3.2 Ellipsometry 81
2.4 Multilayered films 83
2.4.1 Multilayers on silicon substrate 83
2.4.2 Simulation of the solar transmission and visible reflectance 85

2.4.3 Experimental realisation on glass 87
2.5 Ageing test 89
2.6 Conclusion 91

CHAPTER IV: TiO_2 – SiO_2 and TiO_2 – Al_2O_3 mixed oxides

1 TiO_2 – SiO_2 composite films for coloured glazed solar collectors 95
1.1 Introduction 95
1.2 Experimental details 96
1.3 Results and discussion 98
1.3.1 XPS 98
1.3.2 Laser Reflectometry 102
1.3.3 Ellipsometry 104
1.4 Experimental realization of multilayered films 107
1.4.1 Optical properties 107
1.4.2 Accelerated ageing test 111
1.5 Conclusion 112

2 TiO_2 – Al_2O_3 composite films for coloured glazed solar collectors 113
2.1 Introduction 113
2.2 Experimental details 115
2.3 Results and discussion 116
2.3.1 XPS 116
2.3.2 Laser reflectometry 119
2.3.3 Spectroscopic ellipsometry 120
2.4 Multilayered films with mixed oxide 124
2.4.1 Optical properties of multilayer films on silicon 124
2.4.2 Optical properties of multilayer films on glass 126
2.4.3 Ageing test 131
2.5 Conclusion 132

General conclusion 135

1 General introduction

The low price of fossil fuels is the most important reason for limiting the heavy use of solar thermal energy. However, oil prices have increased by 20% the last ten years. For this principal reason a fast transition to an energy structure based on renewable energy is of utmost importance to limit the high dependency on imported fuels. Solar thermal energy is considered as an adequate alternative energy resource for heating and cooling to replace fossil fuels. In 2005, approximately 10 GWth of solar thermal capacity were in operation in Europe. It could be increased to reach 200 GWth by 2030, when solar thermal energy will be used in the majority of buildings [1]. To meet this realizable objective, it is expected that the solar thermal collectors will cover, together with photovoltaic modules, the entire south-oriented roof area of buildings. In addition to the roof areas, south facing facades also have to be used as active solar absorption surfaces. Therefore, the solar collectors have to be completely integrated into the building envelope components. Building integration is considered to be a huge barrier for their development. It concerns the overall image of the solar system in the building. From the point of view of the architects, the aesthetic aspect is the main reason for talking about building integration.

One motivation in our work is finding a solution to the problem of black colour appearance due to the black body which dominates the external aspect of buildings covered by solar thermal collectors. Until today, no satisfying economically interesting solution to increasing the architectural attractiveness of solar collectors has been found. A study showed that more than 80% of architects and engineers rated as important the possibility to choose a custom colour [2, 3]. For two-thirds of them this is even an essential requirement. On the choice of the actual colours, the majority of architects preferred the colour grey, independent of their geographical origin. Another study conducted by AEE INTEC showed that 85% of architects prefer any colour besides black [4].

One recent idea is the use of coloured glazing of cover glass for thermal solar collectors and building faces by depositing a multilayer thin film on the glass surface. The ideal reflectivity of the glass-film system should be a narrow band of the visible

light while transmitting the rest of the sunlight towards the black body to minimize energy losses, see on Figure 1.

In this way, one part of the solar energy in the visible spectrum is invested to make it more aesthetically pleasing and the other part of energy, most of the energy, will pass through the cover, be absorbed and converted to heat in the black surface of the absorber sheet of the solar collectors [5]. However, a compromise has to be found between a high solar transmission and high colour luminosity. For this purpose the reflecting multilayers consisting of oxides materials have to fulfil some requirements. Firstly, a large amount of power from solar radiation must be transmitted through the coatings. Secondly, there is a need for zero or near zero absorption materials to avoid energy loss within the coating. Another important factor is the stability of colours with respect to a varying angle of reflection. Lastly, another critical factor is a narrow peak reflectivity in the visible range fixing the desired colour of the reflected light.

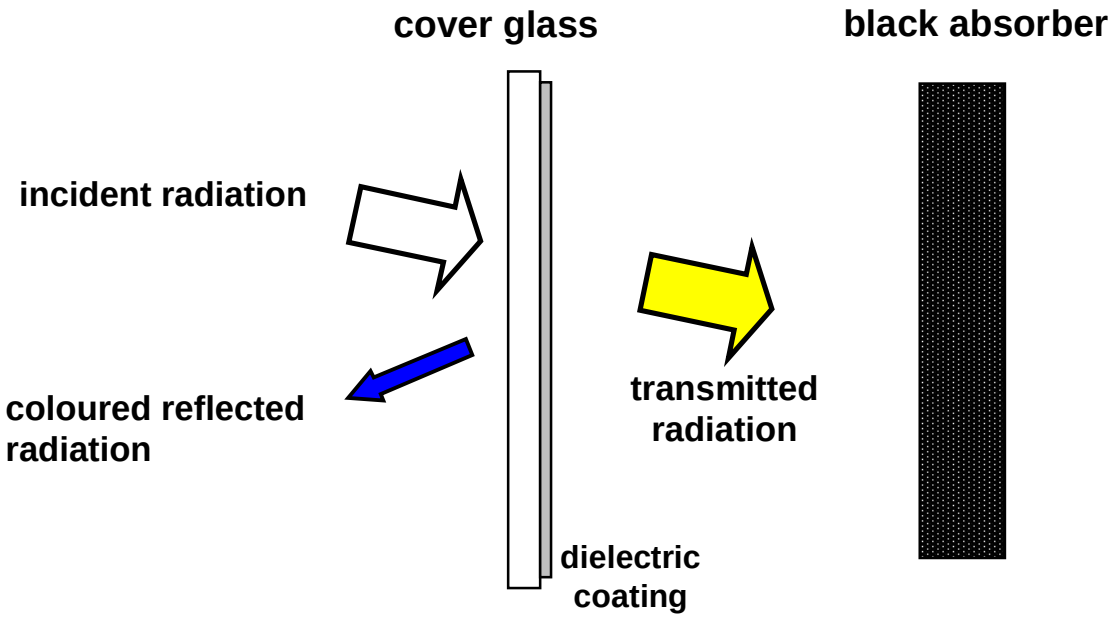

Figure 1: Principle of a coloured thermal solar collector [5]

To obtain coloured reflected light, the cover glass of the collector should be coated on one side or both by thin films. To avoid any absorption, the thin films must be

made by dielectric and transparent materials, such as SiO_2, Al_2O_3, TiO_2 or a mixture of these oxides.

Such optical coatings show a large spectrum of application in every branch of science and technology due to the wide development of the physics and technology of thin films in the beginning of 1930. This includes in particular transparent dielectric coatings for optical filters such as: antireflective coatings for the visible and infrared range with one or more zeros reflectance at a specific wavelength [6], beam splitters [7], band pass filters, high reflectance coating [8], edge filters [9], broadband and narrowband pass filters [9], interference colour-shifting films, low laser damage filters [10], chirped mirrors for ultrashort laser pulse compression [11] and optical sensors [12], hot-cold mirrors and optical waveguides. Worldwide glass production is provided with anti-reflecting coatings, optical filters for thermal control or decorative coatings. In modern architecture, large glass planes are used as facades in commercial buildings and glazing in a residential home for day lighting.

Whatever the application, structural and electronic properties of thin films depend on deposition method and growth conditions, which have to be well understood and controlled. Several criteria should be respected when choosing the material film and the film deposition process for the desired optical application:

- the deposition technique must allow good control and reproducibility of the optical properties of the film, which are strongly dependent on the preparatory conditions. In all optical film application, at least two basic materials with high n_H and low n_L refractive indexes are necessary. A large (n_H-n_L) value may help to reduce the design thickness.
- in most optical coatings application, materials are desired to be amorphous, isotropic, and scattering below 10^{-4}.
- an appropriate deposition technique is required to achieve good film thickness uniformity across the coated substrate, an acceptable deposition rate, and a good environmental stability.

The common techniques for optical filters fabrication are the physical vapour deposition methods such as evaporation and sputtering, frequently assisted by ion bombardment: ion plating, ion beam assisted deposition, unbalanced magnetron sputtering, cathodic arc deposition. Sol-gel deposition is also considered as an interesting alternative route for large-scale surface coatings.

General introduction

In this work, we have chosen the reactive magnetron sputtering for realising the multilayer dielectric films as it is considered as the most used process for the deposition of a wide range of coatings in industry. This project was done in a close and fruitful collaboration with the research group of Dr. Andreas Schüler, LESO-PB, Ecole Polytechnique Fédérale de Lausanne.

The thesis is divided into four parts. In the first part, we describe the basic concept of the techniques used for the realisation of the multilayer films and their characterisation. The second part is devoted to the study of the interfaces formed between TiO_2 and SiO_2 and TiO_2/SiO_2 multilayers. The third part deals with the interface between Al_2O_3 and SiO_2 and Al_2O_3/SiO_2 multilayers. The fourth part is devoted to the optical properties multilayered samples made from mixed oxides TiO_2-SiO_2 and Al_2O_3-SiO_2. At the end, we give a general conclusion of my thesis work.

REFERENCES

[1] European Solar Thermal Technology Platform, Solar Thermal Vision 2030, May 2006, http://esttp.org
[2] MC. Munari-Probst, C. Roecker, A. Schüler, Architectural integration of solar thermal collectors : results of an European Survey, in Proceedings ISES (2005) Orlando, USA
[3] MC. Munari-Probst, C. Roecker, A. Schüler, JL. Scartezzini, in Proceedings EuroSun (2004) Freiburg, Germany
[4] I. Stadler, Industry Workshop und Experts Meeting der Task 26 des Solar Heating and Cooling Program der Internationalen Energieagentur (IEA-SHC) (2001) TNO Building and Construction Research, Delft, Niederlande
[5] A. Schüler, International Patent Application, WO 2004/079278, published on 16.09.2004
[6] J. Mouchart, Appl. Opt. V.17 (1978) 1039
[7] L. Holland, K. Hacking and T. Putner, Vacuum, N. 3 (1953) 159
[8] O.S. Heavens, H.M. Liddell, Appl. Opt. (1966) 373
[9] L. Epstein, J. Opt.Soc. Am. V. 42 (1952) 806
[10] S W Harmer and P D Townsend, J. Phys. D: Appl. Phys.V. 35 *(2002) 2516-19*
[11] D.E. Spence, P.N. Kean, and W. Sibbett, Opt. Lett., V.16 (1991) 32
[12] S.Y. Yurish, Sensors & Transducers Magazine, V. 56 (2005) 326

In chapter I, we describe the basic concept of the techniques used for the realisation of the multilayer films and their characterisation.

1 Thin film deposition method

1.1 Magnetron sputtering

Sputtering is done in a high vacuum chamber pumped down to a base pressure before the deposition starts. Atoms at the surface of the target plate (cathode) are removed by energetic ions generated in glow discharge plasma and bombard the front part of the target.

When power is supplied to the magnetron a negative voltage is applied to the target. Thereby, argon ions are attracted to the target surface and collide with its surface. Target atoms are knocked out of the target surface with mean kinetic energies of 4 to 6 eV. Secondary electrons are emitted from the target surface, become trapped by the magnetic fields and undergo further ionizing collisions sustaining the plasma; see schematically on Figure 1. During the sputtering process a glow is observed, which is caused by excited ions relaxing to a lower energy state and emitting energy in the form of light. Different elements emit the visible light at a different wavelength and therefore different colours may be observed.

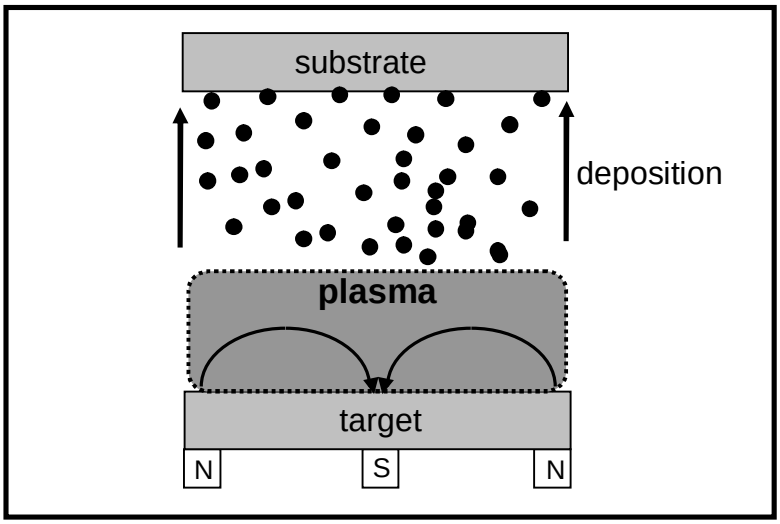

Figure 1: Schematic representation of the plasma confinement observed in conventional magnetrons

The sputtered atoms are driven towards the substrate (anode) where they condensate as a thin film. The magnets of the magnetrons, located behind the target, are arranged in such way that one pole is positioned at the central axis of the target and the second pole is a ring of magnets around the outer edge of the target. The magnets enhance ionisation and effectively direct the sputtered atoms towards the substrate. The magnetic field constrains secondary electron motion to the vicinity of the target. Consequently, the probability of an ionising electron-atom collision occurrence is high.

In our case, all dielectric oxide coatings were produced by reactive magnetron sputtering or pulse magnetron sputtering from a metallic target in a controlled atmosphere of mixed argon-oxygen gas. A radio frequency (RF) power source (RFX-600 and the matching network ATX-600 from Advanced Energy) was used for sputtering silicon dioxide. RF sputtering technique at a frequency of 13.56 MHz is used especially for insulator materials. Although the coating speed is relatively low compared to DC Magnetron Sputtering, its ability to sputter insulator cathodes has adapted this technique to a wide variety of applications, such as silicon dioxide films.

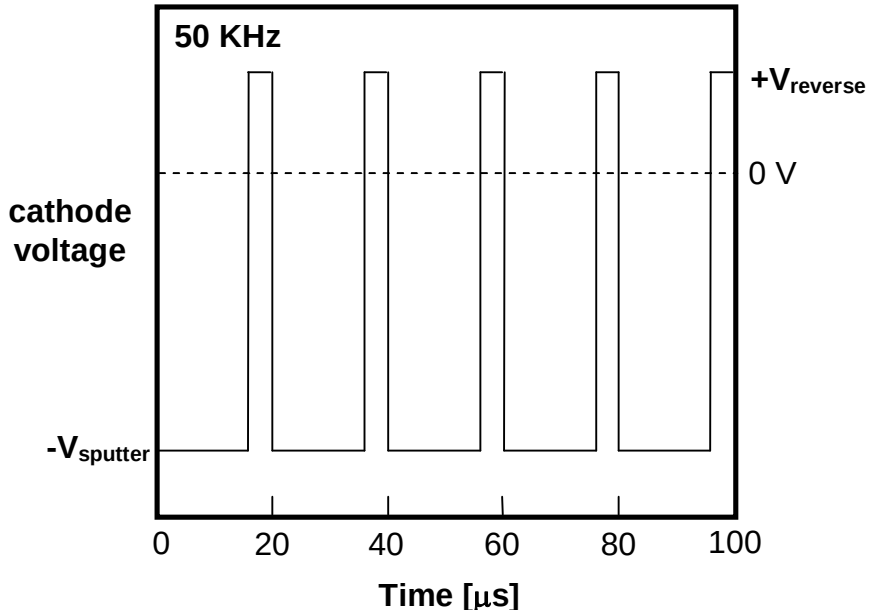

Figure 2: Schematic representation of the power cycle of the bipolar pulsed power supply

The bipolar pulse magnetron (MDX magnetron driver from Advanced Energy) sputtering was used to deposit titanium or aluminium oxides. A direct current (DC)

potential is used to drive the ions towards the surface of the target, causing atoms to be knocked off the target and condense on the substrate surface. A strong magnetic field is applied to contain the dense plasma near the target region, to allow the discharge to be maintained at lower operating pressure (10^{-3} mbar) and at lower operating voltage and to increase the deposition rate. Another advantage of DC sputtering is that the target poisoning is avoided due to the asymmetric bipolar pulsing, as represented in Figure 2. The target poisoning is the coverage of the target by the oxide to be deposited. The poisoned layer charges up until breakdown occurs in the form of arcs. During the periodic short pulses the charging is avoided by plasma electrons attracted to the positive surface.

A home-made ring magnetron was used to deposit mixed oxide films at one time with a high growth rate; see Figure 3. It consists of an inner target and an outer target. It was therefore possible to drive it by two different power sources (DC and RF powers).

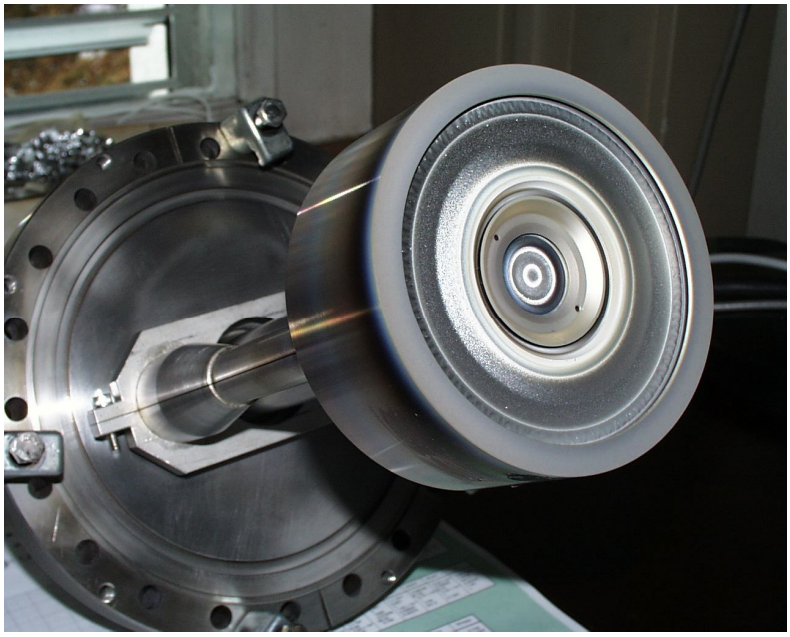

Figure 3: Home-made ring magnetron for sputter deposition of mixed oxides

1.2 Sputter system

All investigated optical coatings were prepared utilizing the existing sputter system in ESCA group at the Institute of Physics in Basel. A ring magnetron or two magnetrons

of planar circular cathodes capped with targets of 3-inch diameter were inserted into the base plate of the cylindrical vacuum chamber. They were bonded to a water cooled copper carrier, ensuring at once electrical and thermal contact. The disposition of the magnetrons in the chamber prevents the targets from being coated during deposition. A rotatable substrate holder is attached to the top cover of the deposition chamber. Up to 10 glass or silicon samples, 40x40 mm^2, can be alternatively coated in different or similar deposition conditions, resulting in a large number of samples prepared in one day without opening the chamber.
Multilayered samples with several stacks of different oxides were produced without breaking the vacuum. The separation distance between target and substrate was approximately 50-80 mm. The substrate to be coated was rotated until a position directly parallel to the target was reached. Then it remained stationary until the desired film thickness was reached. For coating the next substrate, the coated sample was removed manually from the substrate holder and kept in a specific aperture.

2 Photoelectron spectroscopy

2.1 Introduction

The photoelectric process, i.e. the effect of electron extraction from solid surfaces exposed to electromagnetic radiation, was first detected by Heinrich Hertz in 1887 [1]. Wilhelm Hallwachs further developed Hertz' experiments and found evidence that photoelectrons are emitted from an irradiated metal plate [2]. Between 1900 and 1902 Philipp Lenard published his works on photoelectrons in a retarding potential [3]. He got the Noble Prize for his studies on cathode rays in 1905. The photoemission phenomenon was first explained by Einstein in 1905 [4] by introducing the quantum nature of light. His work was honoured by the award of the Nobel Prize in 1921.
In the following years the photoeffect was more extensively studied and laboratory equipment was improved for analytical use in the 1960s, largely due to the pioneering work of Kai Siegbahn's group [5]. Important steps were the development

of better electron spectrometers, the discovery that electron binding energies were sensitive to the chemical state of the atom, and the realization that the technique was surface sensitive. This surface sensitivity, combined with quantitative and chemical state analysis capabilities, have made photoelectron spectroscopy the most broadly applicable surface analysis technique nowadays. It can detect all elements except hydrogen and helium with a sensitivity variation across the periodic table. Samples can be gaseous, liquid, or solid, but the vast majority of electron spectrometers are designed to deal with solids. The depth of the solid material sampled varies from the 2 top atomic layers up to 15-20 layers. Photoelectron spectroscopy is considered to be the least destructive method of all the electron or ion spectroscopy techniques. Analysis times may vary from a few minutes to many hours.

2.2 Principle of photoemission and photoelectron spectroscopy

In photoelectron spectroscopy, the sample to be investigated is irradiated by photons. Electrons are emitted from the sample due to the photoelectric effect and are analyzed with respect to their kinetic energy E_{kin} by an electrostatic analyzer. The irradiated atom in the solid sample material releases an electron according to Einstein's photoelectric law of 1905 [4]; see Fig. 4:

$$photon + atom \rightarrow atom^{+} + e^{-} \qquad \text{(I. 1)}$$

From energy conservation results:

$$h\nu + E(atom) \rightarrow E(atom^{+}) + E_{kin} + \Phi_0 \qquad \text{(I. 2)}$$

Φ_0 is the workfunction of the sample, i.e. the energy to be invested so that the emitted electron leaves the sample reaching the vacuum level E_{vac}.

The binding energy with respect to the Fermi level of the sample can be written:

$$E_B = E(atom^+) - E(atom) \qquad \text{(I. 3)}$$

and the kinetic energy of the free electron becomes:

$$E_{kin} = h\nu - E_b - \Phi_0 \qquad \text{(I. 4)}$$

Since $h\nu$ is known, a measurement of E_{kin} permits to determine E_B. To a first approximation, the E_B of an electron, as determined by the amount of energy required to remove it from the atom, is equal to the eigenvalue (this would be exactly true if, when removing an electron, all the other electrons did not respond in any way). By experimentally determining the E_B, one is approximately determining an eigenvalue, which is specific to the atom concerned, thereby identifying that atom. A photoelectron spectrum also consists of electrons with discrete energy losses (plasmon excitations) and an additional featureless background of inelastically scattered electrons.

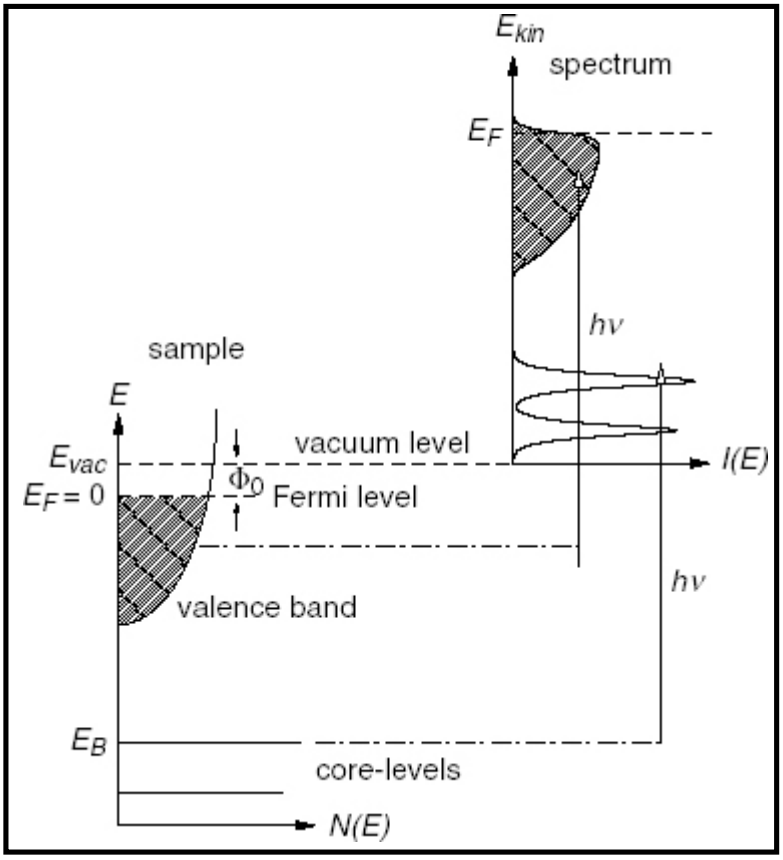

Figure 4: Schematic energy level diagram of an atom and the XPS spectrum after irradiation [6]

It should be noted that it would be practically impossible to know the work function of each analysed sample. As the electrical contact between the sample and the spectrometer equalizes the Fermi level of both [6, 7], the sample Fermi level always occurs at the same energy level.

Photons in the ultraviolet UV spectral range and X-rays can be used for excitation. The techniques are called UV photoelectron spectroscopy (UPS) and X-ray photoelectron spectroscopy XPS or ESCA (Electron Spectroscopy for Chemical Analysis), respectively. Nowadays, synchrotron radiation allows the use of a wide spectral range of excitation energies and photon fluxes several orders of magnitude larger than conventional X-ray tubes.

2.3 Electron escape depth

In photoemission experiments with solids, only electrons originating from a thin surface layer of the sample are normally used in the analysis of the spectra, making photoemission a surface sensitive technique. The reason is that only the electrons which leave the sample without losing energy carry information about the electronic structure.

Photoelectrons ejected from the top atomic layers escape the surface unscattered and appear in the XPS peaks. Electrons originating from deeper layers have reduced chances of escaping the surface unscattered and mostly end up in the background at lower E_{kin} after the XPS peak. These electrons experience energy losses due to electron-electron (excitation of plasmons, scattering or creation of electron-hole pairs) and electron-phonon interactions. The further the photoelectron has to travel, the higher the probability for energy losses. Thus, the peaks come mostly from atoms near the surface, the background mostly from the bulk.

If I_0 is the flux of electrons originating at depth d, the flux emerging without being scattered, I_d, exponentially decreases with depth according to:

$$I_d = I_0 e^{-\frac{d}{\lambda_e \sin\theta}} \qquad \text{(I. 5)}$$

where θ is the angle of electron emission and $\frac{d}{\sin\theta}$ is the distance travelled through the solid at that angle. The quantity λ_e is called the inelastic mean free path length or electron escape depth, which represents the probability for an electron to leave the sample without inelastic scattering. It is a function of the electron kinetic energy, being only in the order of a few Å and is determined by collisions:

$$\lambda_e(E_{kin}) = v(E_{kin})\tau = \frac{\hbar k}{m}\tau \qquad \text{(I. 6)}$$

where v is the velocity, τ is the collision time, k the Boltzmann constant, m the electron mass and $\hbar = h/2\pi$ the reduced Planck constant.

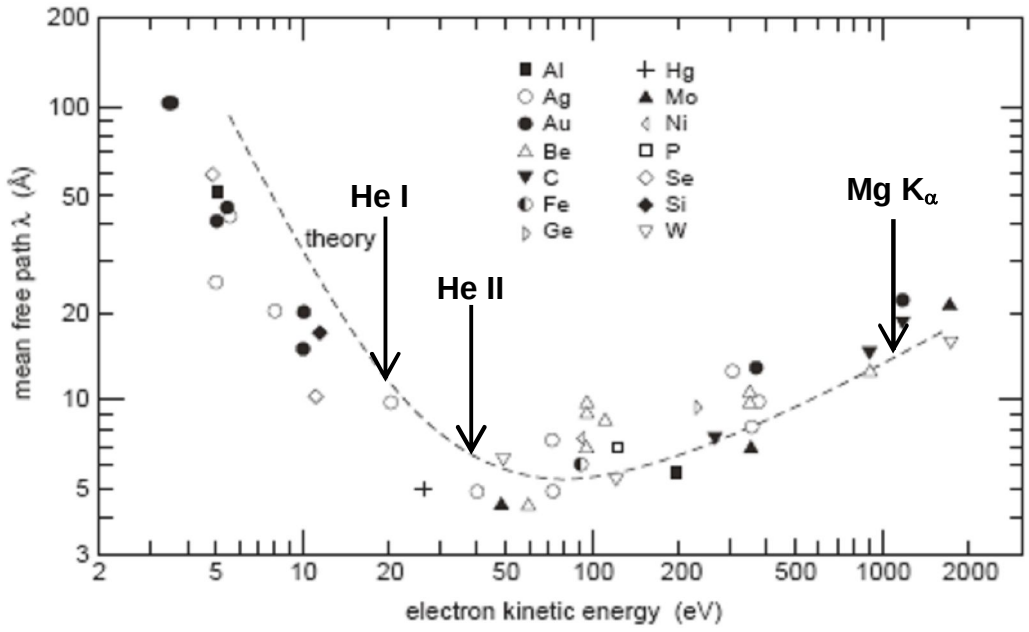

Figure 5: Measured (dots) and calculated (dashed curve) mean free path of the electrons in solids versus electrons kinetic energy [8]

The mean free path of the electrons is an important parameter in PES and is plotted in Fig. 5. The dashed curve shows a calculation of the mean free path independent of the material, and the points are the measured data from many elemental solids. The data points scatter more or less around the calculation. The curve is often called universal curve. The reason for this universality is that the inelastic scattering of electrons in this energy range mostly involves excitations of conduction electrons,

which have more or less the same density in all elements. The mean free path curve has a broad (note the log-log scale) minimum less than 10 Å around a kinetic energy of about 70 eV. This means that if we observe an electron with this kinetic energy which has left the solid without suffering an inelastic scattering event, it must originate from the first few layers. Note that at lower energies other scattering mechanisms will be important, like scattering with phonons. The energy loss associated with a scattering from the valence electrons is rather large. Therefore it is relatively easy to distinguish between inelastically scattered and non-scattered electrons.

2.4 Three-step model versus one-step model

The 'three-step model' [6] was proved to be useful for the interpretation of the complex photoelectron process; see Fig. 6. The first step assumes optical excitation of an electron by the photon, from an occupied valance state to an empty conduction state. The second step is the ballistic transport of the electron to the surface without scattering. The third and last step reports the transmission of the electron across the surface into the vacuum.

For the first step, the transition probability of electrons by the excitation from the initial state *i* (ψ_i) to the final state *f* (ψ_f) per unit time is given by Fermi's Golden Rule:

$$P_{fi} = \frac{2\pi}{\hbar}\left|\langle \psi_f \left| H' \right| \psi_i \rangle\right|^2 \delta(E_f - E_i - \hbar\omega) \qquad \text{(I. 7)}$$

H' is the Hamiltonian for the electron-photon interaction.

During the transfer through the sample towards the surface the photoelectron experiences scattering and energy losses, as we have discussed above. In the last step, the kinetic energy perpendicular to the sample surface has to be large enough to overcome the sample's work function.

A more general description of the photoemission process, the so-called one-step [6] model, consists of the excitation of an initial occupied electronic state inside the solid,

by absorption of the incident photon, into an empty state outside the solid. The excited electron must have its velocity pointing out of the solid so that it can be collected by the detector. This process, which is simple but poses considerable computational problem when quantitative evaluation is attempted, is constrained by conservation laws.

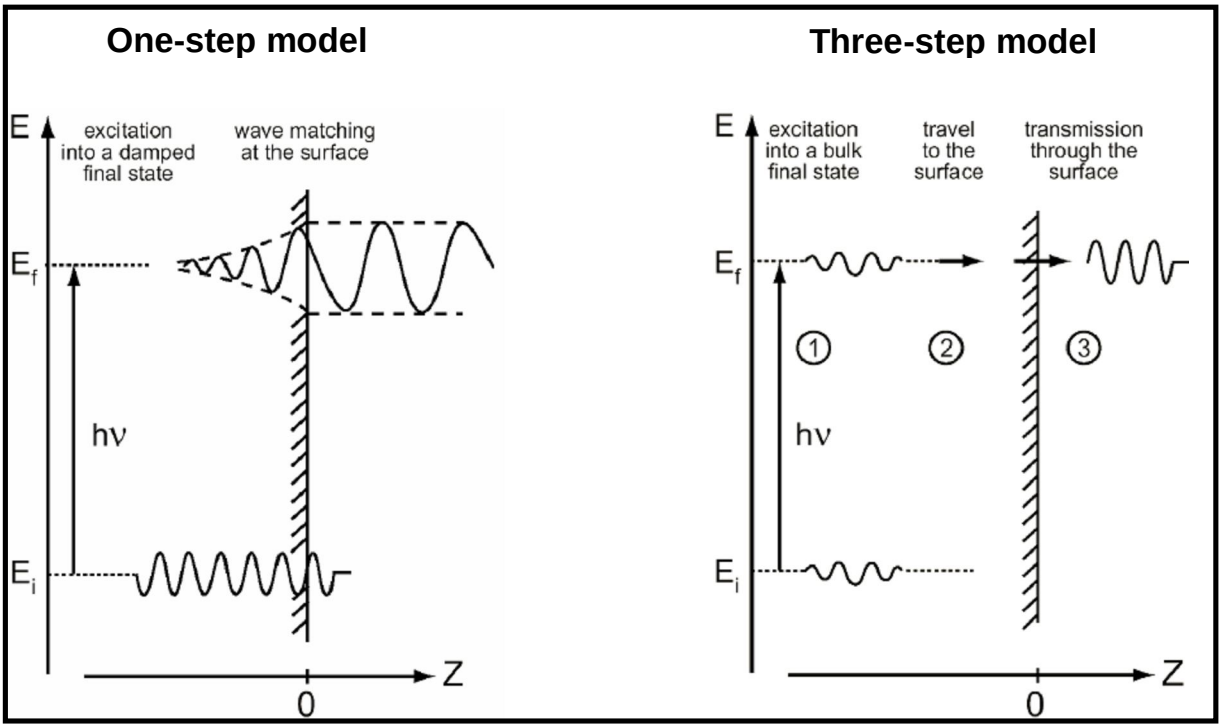

Figure 6: Illustration of the three-step and one-step model [9]

2.5 Photoelectron spectroscopy applied to insulating materials

The positive charges resulting from the photoionization are immediately neutralized by an electron flux in a conductive sample. On the contrary, the neutralization is only partial and a positive charge accumulates at the surface of the insulator sample. Consequently, the sample surface acquires a positive potential and the kinetic energy of the photoelectrons decreases, resulting in a binding energy shift. A satisfactory solution to charging problems has not yet been established. However, several useful and partially successful approaches have been developed and are presented in the following paragraphs.

2.5.1 Analysis of very thin films

The easiest way to alleviate the charging problem is to reduce the thickness of the insulating layer so that electrons from a metallic substrate can tunnel into the dielectric insulating layer. The problem is that the structure of thinner film is not the same as a thicker one.

2.5.2 Calibration by an internal reference

The calibration by an internal reference consists of using intrinsic materials for the reference level problem. For example, the C1s core level of carbon atoms present in the dielectric film can usually be assigned to the binding energy at 285 eV [10]. The carbone calibration is not reliable due to different chemical shifts resulting from different bonding situations. The Si2p core-level binding energy position can also be used for this purpose when depositing SiO_x.

2.5.3 Calibration by an external reference (gold layer)

The calibration consists of depositing a very thin gold layer on the insulating substrate, which is supposed to be at the same potential as the insulating surface. The difference between the binding energies of the Au4f peak and its bulk reference value, 84 eV, gives the value of the charging potential. However, this method supposes that gold is not reacting with the surface and does not form any compound with the surface atoms. In reality, gold deposited on insulating surfaces has a tendency to agglomerate and to grow in the form of 3D clusters. Therefore, the core-level binding energy shift is rather associated to the cluster's size than to the charging effects [11,12].

2.5.4 Surface charge neutralisation by an electron beam

The flood gun is one of the easiest and most common solutions to charging problems. A beam of low energy electrons is directed at the surface and contributes to the neutralization of the surface positive charge. The main difficulty is adjusting the flood gun voltage to balance the positive charge exactly, without getting an excess of

electrons inducing negative sample charging. This is usually done by tuning the voltage for minimum core-level linewidth. One does not have to modify the chemical state of the atoms or induce electron-stimulated decomposition when using the electron beam. For example, silicon oxide decomposition induced by an electron flux is a well-known phenomenon [13, 14].

2.5.5 Analysis of the Auger parameter

One of the most elaborate ideas for extracting chemical information when charging occurs is the Auger parameter approach, which was developed by Wagner et al. [15]. As the charging potential affects the binding energy and the kinetic energy by the same amount, this approach is based on calculating the sum of a core-level binding energy and the kinetic energy of a core Auger peak of the same element:

$$\alpha' = E_B \text{ of the core level peak} + E_{Kin} \text{ of the Auger core level peak} \qquad \text{(I. 8)}$$

In the simple approximation introduced by Thomas [16] and Wagner [17], the modified Auger parameter shifts with respect to the bulk can be expressed as:

$$\Delta\alpha' = 2\,\Delta R = 2\left(\Delta\varepsilon - \Delta E_B\right) \qquad \text{(I. 9)}$$

ε is a term related to the eigenvalue of the level undergoing photoemission and the initial state charge distribution *R* is the extra-atomic relaxation energy of the photohole.

The modified Auger parameter is directly related to the amount of extra-atomic screening of core holes and characterizes the chemical state of the element.

2.5.6 Parameters insensitive to charging effects

This method consists of calculating parameters which are not affected by charging effects—in other words, one look at the binding energy differences between two core levels rather than the absolute value of each one. This difference characterizes the

chemical states of the atoms, when both core levels have the same relaxation energy and are affected by the same manner by the charging effect. Comparison with published values can bring useful information and may allow one to identify a compound or chemical state. For example, the difference between the O1s and Si2p binding energies has been used to characterize the Si-O bond in silica [18].

2.6 Experimental set-up

To observe the inner structure of an atom, one has to be equipped with a dispersion element, capable to distinguish electrons by their kinetic energy and yield—an electron energy spectrum. The group of Prof. Siegbahn from the Uppsala University in Sweden have employed hemispherical electron analyzer to this purpose [19]. This discovery opened new opportunities in solid-state research, and was extensively exploited and developed in the following years. Having an electron analyzer and an excitation source, one obtains a photoelectron spectrum. To extract electrons from the inner shells, excitation photons of the order of 1000 eV have to be employed, falling into the soft X-ray region. For this purpose most often Mg K_α ($h\nu$ = 1253.6 eV) and Al K_α ($h\nu$ = 1486.6 eV) lines are used. Extracting valence electrons from an atom requires lower energy ultra-violet photons, and most frequently employs the vacuum-UV lines from the neutral and single-ionized helium, HeI, $h\nu$ = 21.22 eV, and HeII, $h\nu$ = 40.80 eV, respectively. This results in the valence-band, or UV photoelectron spectrum (UPS).

In this work, we used a electron spectrometer (Figure 7) equipped with a hemispherical analyser (HMA, SPECS EA 10), an X-ray source for core-level spectroscopy (X-ray photoelectron spectroscopy XPS: Mg $K\alpha$ excitation, $h\upsilon$ = 1253.6 eV) and a UV lamp, operating in helium flow at 10^{-5} mbar for He I (21.22 eV) and at 10^{-6} mbar for He II (40.82 eV) excitation of the valence band. The typical resolution is 0.8 eV for the XPS measurements. A gold sample with the Au $4f_{7/2}$ core-level signal at binding energy of 83.9 eV is used as a reference for the electron energy calibration. The work function Φ of our spectrometer, identical to that of the measured sample, is 4.4 eV.

The analyser consists of two concentric hemispheres with radii of 114 mm and 80 mm. The entrance and exit slits are centred at the mean radius of 97 mm. High voltages are applied to the hemispheres to allow only electrons with a chosen kinetic energy (pass energy E_p) to reach the detection device successfully and be counted. Electrons emitted from the sample after X-ray or UV excitation are accelerated or decelerated by the two-stage electrostatic lens system. At the exit slit, a multichannel detector with 18 discrete channels is mounted, counting the number of arriving electrons and converting it into a voltage signal. The analyser can be operated in the constant analyser energy mode (*CAE*) or in the constant retardation ratio mode (*CRR*).

In the *CAE* mode, the voltage between hemispheres—in other words the pass energy—is kept constant, and the electrostatic lens system accelerates or decelerates all electrons to that fixed value. This implies a constant energy resolution ΔE, as ΔE is a function of the slit width, the HMA radius and the pass energy. The overall (analyser and transfer lenses) transmission function T is proportional to $1/\sqrt{E_{kin}}$.

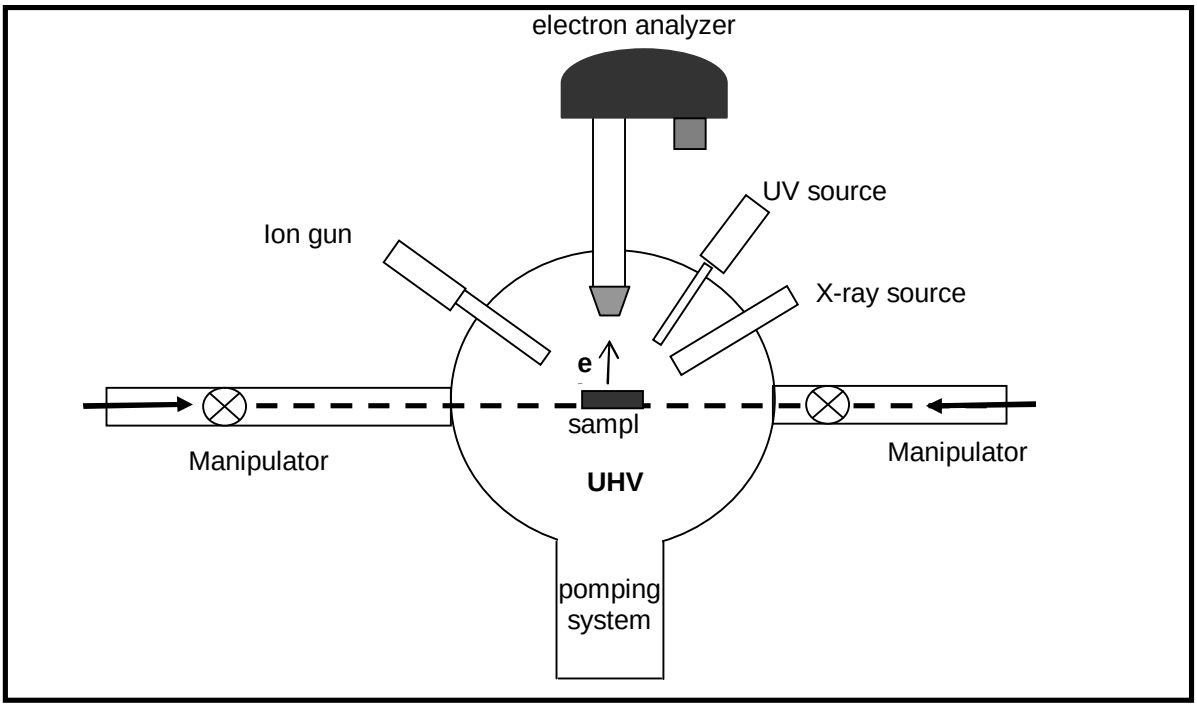

Figure 7: Schematic diagram of ESCA measurement chamber equipped with a non-monochromated X-ray source ($h\upsilon_{MgK\alpha}$ = 1253.6 eV), a UV source ($h\upsilon_{HeI}$ = 21.2 eV, $h\upsilon_{HeII}$ = 40.8 eV) and Ion gun

In the *CRR* mode, electrons arriving to the entrance slit pass the full deflection angle to the exit slit only with a certain kinetic energy. The electron energy spectra are created by scanning the analyzer system over the range of excitation photon energies
by changing the voltage between the hemispheres. In this case, all electrons arrive to the entrance slit with their original energy, decelerated by the same fixed factor E_{kin}/E_p^*. As the pass energy is no longer constant, the resolution is also not constant (proportional to E_{kin}) and the transmission function is proportional to E_{kin}. Traditionally, UPS measurements are done in the CRR, and XPS in the CAE operation mode.

2.7 Data analysis

The shape of a core-level photoelectron peak depends on the peak type as well as on the insulator or metallic nature of the sample. In addition, several overlapping components can be present in the peak due to the coexistence of different chemical states of the same element. The shape of a peak corresponding to a single chemical component should be determined separately for every chemical compound. Practically in most cases (except high-resolution measurements) the peak shape can be well-described by the Gauss-Lorentz (Voight) profile for semiconductors and insulators.
An X-ray photoelectron spectrum of a solid-state sample always contains a background, which is formed by inelastically scattered photoelectrons. To estimate the peak shape and the stoichiometry from an experimental spectrum, first the background should be subtracted. Different models of background shape are in use. A simple linear-type background can be used for fast spectra analysis, while for more accurate line shape and stoichiometry analysis more complicated background types should be used. D. A. Shirley suggested the background shape on the assumptions of a constant energy spectrum of scattered photoelectrons and a constant scattering probability in the peak region.
The stoichiometry of the sample surface can be estimated from the area ratio of XPS peaks. The general formula for the XPS peak area for an element *a* is:

$$I = n f \sigma \theta y \lambda_e A T = nS \qquad \text{(I. 10)}$$

The relative concentration of a given element *a* is then deduced by:

$$[a] = \frac{\frac{I_a}{S_a}}{\sum_i \frac{I_i}{S_i}} \qquad \text{(I. 11)}$$

where n_a is the atomic concentration of the element, f is the X-ray flux, σ is the photoelectronic cross-section for the atomic orbital of interest [20], θ is the angular efficiency factor for the instrumental arrangement, y is the efficiency in the photoelectronic process for formation of photoelectrons of the normal photoelectron energy, λ_e is the mean free path of the photoelectrons in the sample, A is the area of the sample from which photoelectrons are detected, T is the transmission, function or detection efficiency for electrons emitted from the sample and S is the sensitivity factor.

3 Laser reflectometry

Laser reflectometry monitoring consists of focusing a laser spot on the surface of a clean silicon substrate (40x40 mm^2) and then measuring the reflected signal by a detector. The optical reflectivity of a laser beam is continuously measured in-situ during the sputtering process of a thick oxide film of several hundreds of nm on a reflecting silicon substrate.

The experimental set-up involves an incident laser beam at 532 nm with 1 mW power and a beam diameter of 1 mm (Laser compact, model LCM-T-01 ccs) at the angle of incidence of 52°; see Fig. 8 The reflected signal intensity is detected with a synchronous modulator. The measurement technique is based on standard laboratory equipments, such as a chopper, photodiodes, lock-in amplifiers for the sampling of monitor and probe beam [21, 22]. The experimental data is visualised directly on a PC monitor and allows therefore an in-situ control of the sputtering deposition. The fit of the experimental data is numerically performed using the

reflectivity formula of a single layer on the substrate [23] to determine the deposition velocity *r* and the optical constants *n* and *k* at a single wavelength, namely 532 nm.

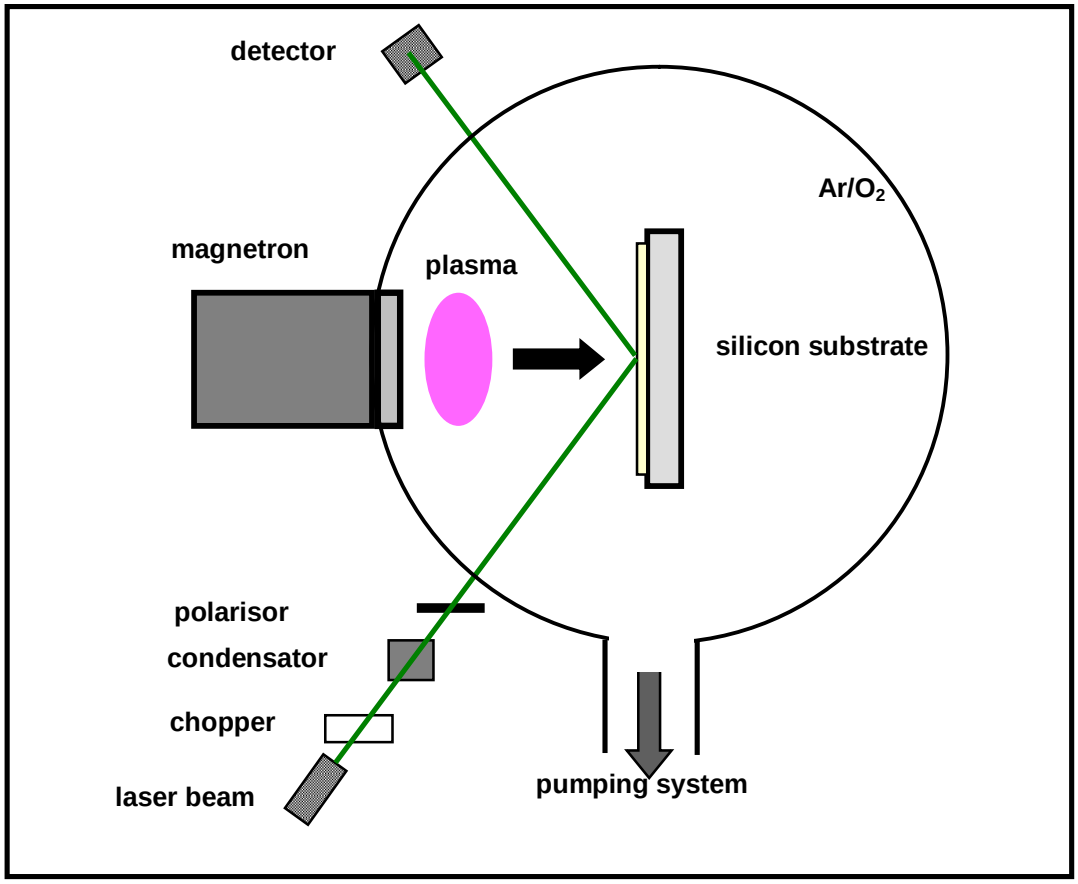

Figure 8: Schematic representation of the laser reflectometry for in-situ measurements during sputtering deposition

4 Spectroscopic ellipsometry

4.1 Introduction

Ellipsometry is a contactless and non-invasive technique to measure changes in the polarization state of light reflected from a sample surface and determine the complex reflection coefficient ratio of the sample, which is dependent on the ratio of the complex reflection coefficient for light polarized parallel and perpendicular to the plane of incidence. Ellipsometry is widely used to determine the thickness and the

optical properties of thin dielectric single or multilayer films [24, 25] on highly absorbing substrates [26].

4.2 Principles of ellipsometry

The mathematical theory for ellipsometric analysis is based on the Fresnel reflection or transmission equations for polarized light encountering boundaries in planar multilayered materials.

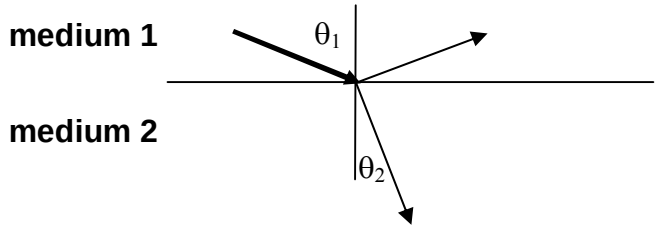

Figure 9: Interface between two mediums

If a light beam is reflected at an interface between mediums 1 and 2 (see Figure 9), the Fresnel coefficients are given by:

$$r_{12}^{p} = \frac{\tilde{N}_2 \cos\theta_1 - \tilde{N}_1 \cos\theta_2}{\tilde{N}_2 \cos\theta_1 + \tilde{N}_1 \cos\theta_2} \text{ and } r_{12}^{s} = \frac{\tilde{N}_1 \cos\theta_1 - \tilde{N}_2 \cos\theta_2}{\tilde{N}_1 \cos\theta_1 + \tilde{N}_2 \cos\theta_2} \qquad \text{(I. 12)}$$

where $\tilde{N}_1 = n_1 - ik_1$ and $\tilde{N}_2 = n_2 - ik_2$ are the complex index of refraction of medium 1 and medium 2; n_1, n_2 being the corresponding refractive indices and k_1, k_2 the respective extinction coefficients. The superscripts *p* and *s* refer to waves parallel or perpendicular to the plane of incidence. The reflected intensities or reflectance are then $\left|r_{12}^{p}\right|^2$ and $\left|r_{12}^{s}\right|^2$.

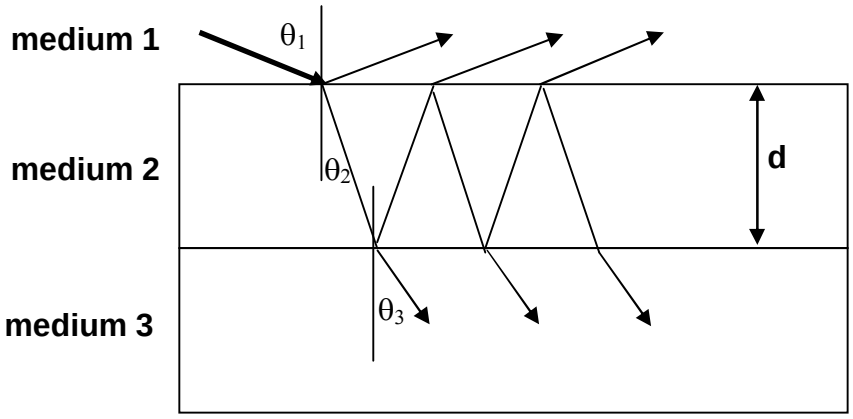

Figure 10: Interfaces between three mediums

In the case of a multiple interface (Figure 10), for example substrate/thin film/air, the complex total reflection coefficients are given by:

$$R^p = \frac{r_{12}^p - r_{23}^p \exp(-i2\beta)}{1 + r_{12}^p r_{23}^p \exp(-i2\beta)} \text{ and } R^s = \frac{r_{12}^s - r_{23}^s \exp(-i2\beta)}{1 + r_{12}^s r_{23}^s \exp(-i2\beta)} \quad \text{(I. 13)}$$

β is the film phase thickness given by: $\beta = 2\pi\left(\frac{d}{\lambda}\right)\tilde{N}_2 \cos\theta_2$, d is the film thickness.

Ellipsometry uses the fact that materials reflect *p* and *s* polarized light differently and determines the ratio of the reflectance of the two polarizations by measuring ψ and Δ as defined by the following equation:

$$\rho = \frac{R_p}{R_s} = \tan\Psi\, e^{i\Delta} \quad \text{(I. 14)}$$

The first ellipsometric parameter Δ defined by $\Delta = \delta_1 - \delta_2$ is the change in phase difference occurring upon reflection and varies from 0° to 360°, δ_1 being the phase difference between the parallel component and the perpendicular component of the incoming wave, δ_2 the respective phase difference for the outgoing wave.

The other ellipsometric parameter Ψ is defined by: $\tan\Psi = \frac{|R^p|}{|R^s|}$

Ψ is the angle whose tangent is the ratio of the magnitudes of the total reflection coefficients. The value of Ψ lies between 0 and 90°.

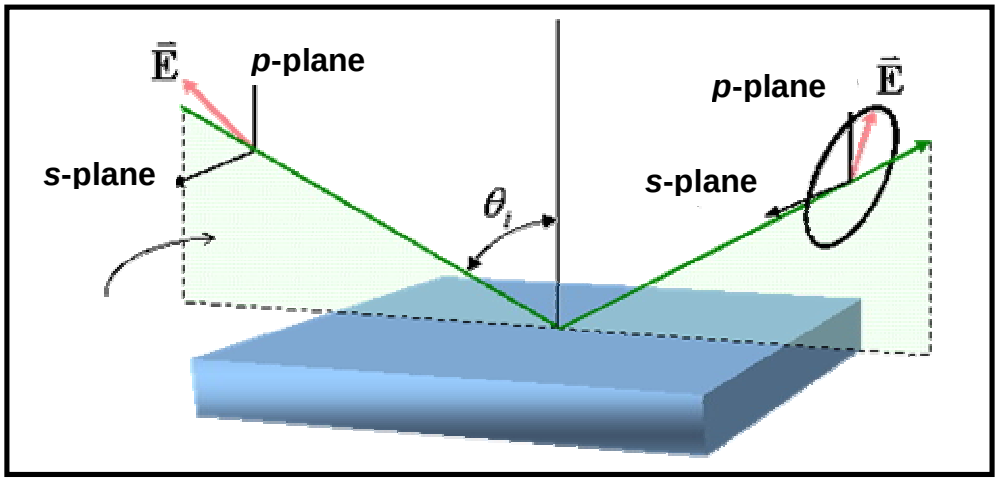

Figure 11: Schematic of the geometry of an ellipsometry experiment

A variable angle spectroscopic ellipsometer performs the measurement of the two ellipsometric parameters as a function of both light wavelength and angle of incidence, see Fig. 11.

4.3 Ellipsometer

The operation principle of an ellipsometer is illustrated by the schematic drawing of Figure 12.

An ellipsometer consists of:

- a monochromatic light source as a laser,
- a polarizer, which is the most important optical element for making ellipsometric measurements. It converts any light beam into linearly polarized light oriented along the transmitting axis,
- an analyzer, which analyzed the reflected light from the sample,
- a detector.

We used a variable angle spectroscopic ellipsometer (SENTECH SE 850). The ellipsometric functions Δ and Ψ can be measured for the wavelength range of 300 -

850 nm with a variable angle of incidence ranging between 40° and 70° with respect to the normal. The optical constants of the film thickness are not measured directly, but have to be extracted through a model based analysis using optical physics.

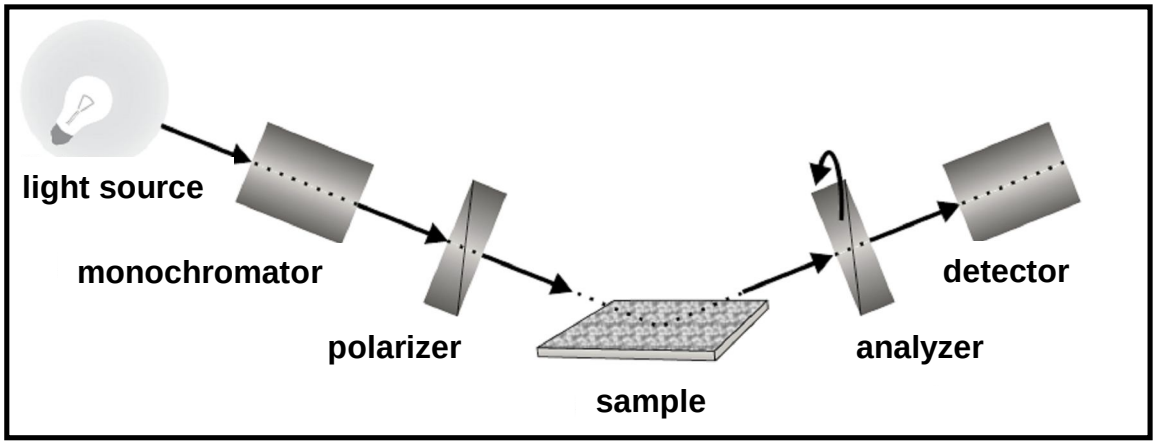

Figure 12: Schematic drawing of an ellipsometer

4.4 Data analysis

SPECTRARAY, SENTECH's software for spectroscopic ellipsometry provides the user a friendly interface to operate the SE 850 ellipsometer. It also comprises easy to use modelling of samples and the important part of spectra fitting to calculate sample parameters like film thickness and refractive indices of multilayer samples. SPECTRARAY is based on Windows and GRAMS which offers the general advantages of the spectroscopic software like data import and export file management, arithmetic manipulation of spectra including display and plot functions.
In the case of a single thin film (for example a dielectric oxide film) on top of a substrate, the experimental ellipsometric data of the deposited thin film were fitted with a widely used Cauchy dispersion formula, where the refractive index *n* and extinction coefficients *k* are given by:

$$n(\lambda) = N_0 + C_0 \frac{N_1}{\lambda^2} + C_1 \frac{N_2}{\lambda^4} \qquad \text{(I. 15)}$$

$$k(\lambda) = K_0 + C_0 \frac{K_1}{\lambda^2} + C_1 \frac{K_2}{\lambda^4} \qquad \text{(I. 16)}$$

N_i, K_i, C_i are constants and λ is the wavelength in nm. $C_0 = 10^2$ and $C_1 = 10^7$ are used to avoid large values of N_1, K_1, N_2 and K_2. The refractive and extinction indices of the substrate are taken from the database of the SPECTRARAY software. The program fits the ellipsometric functions Δ and Ψ using only seven parameters N_0, N_1, N_2, K_0, K_1 and K_2 and the thin film thickness d. Once the refractive and extinction indices are fitted, the software can be used to simulate other optical properties, like the total reflectivity, the angle dependent reflectivity, etc.

In the case of a multilayer thin film consisting of alternating layers of two dielectric materials, the thicknesses of every individual layer is the result of the ellipsometric data fit using the optical properties of the two individual materials.

4.5 Effective medium approximation

In this work, we have also studied thin films consisting of a mixture of two different oxides using an effective medium approximation (EMA), which has been a tool for the evaluation of the optical properties of composite media for a long time.

When doing optical analysis, one frequently encounters mixtures of materials with known optical properties for the constituents. If the local variations of the optical properties are of a much smaller scale than the wavelength of the light, the mixture can be modelled as a continuum; see Figure 13. The optical properties of the mixture can be calculated from the known optical properties of the constituents. For this purpose, the effective medium approximation method has been developed. Several different EMA models have been developed, optimized for different microstructures.

The simplest approach for application in the optical regime, dating back to 1904, was derived by Maxwell- Garnett theory (MGT) [27] and is a replication of the Clausius-Mosotti formula. In the 1930s the more recent self-consistent Bruggemann theory (BT) was developed [28]. The validity of the different approaches to predict the optical properties of composite materials has been discussed frequently. Reviews concerning the subject can be found in [29, 30].

If the wavelength of the electromagnetic radiation is much larger than the particle size, classical theories of inhomogeneous media presume that the material can be treated as a homogeneous substance with an effective dielectric function and

effective magnetic permeability. These quantities depend upon the properties of the constituents, as well as their volume fractions and sizes [31]

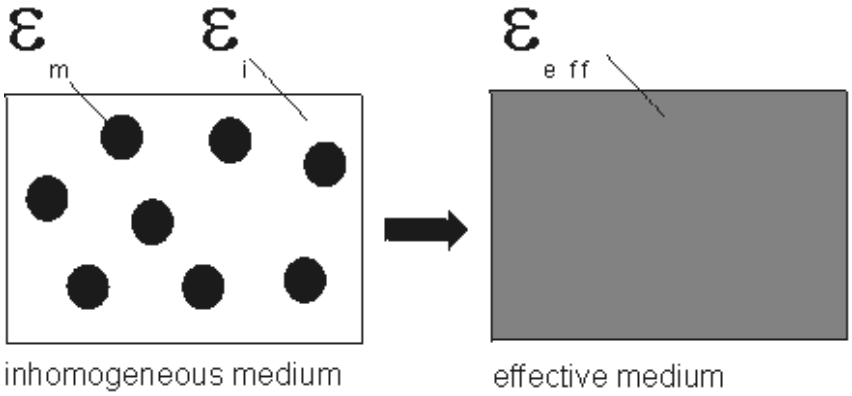

Figure 13: An inhomogeneous system is replaced by a (virtual) effective medium

Essentially, the MGT is a modification of the Lorentz-Lorenz (LL) [31] formula for small particles and the first approach to consider the local field. It was found by averaging the electric fields and polarizations induced by the applied electric field in the composite medium. The Maxwell-Garnett geometry shown in Fig. 14 visualizes, that the quasi-static approximation holds; static with respect to the interaction of light with particles, if $2 R / \lambda << 1$, dynamic with respect to the dielectric properties of the free electrons in the inclusions. The circle with radius R shows the Lorentz-cavity.

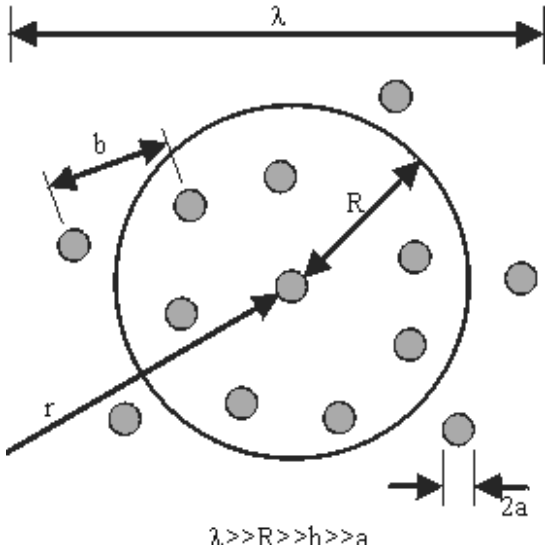

Figure 14: The geometry of a Maxwell Garnett composite material [32]

For the LL, MG and Bruggeman effective medium approximations, the dielectric functions ε_i of the *m* types of inclusions provided with a volume fraction f_i in a host medium having dielectric function $\varepsilon_{host,}$ and the effective dielectric function ε_{ff} fulfil the following equation:

$$\sum_{i=1}^{m} f_i \frac{\varepsilon_i - \varepsilon_{host}}{\varepsilon_i + 2\varepsilon_{host}} = \frac{\varepsilon_{eff} - \varepsilon_{host}}{\varepsilon_{effi} + 2\varepsilon_{host}} \qquad \text{(I. 17)}$$

The LL approximation was developed to describe point polarisable entities embedded in vacuum. In that case ε_{host} = 1. MG corresponds to inclusions in a host background different from the vacuum. At low volume fractions, Maxwell-Garnett and Bruggeman lead to very similar results of the effective dielectric constants, but Bruggeman ensures validity at higher volume fill fractions since it treats both constituents symmetrical [33]. In the Bruggeman model, the host is the effective medium $\varepsilon_{host} = \varepsilon_{eff}$.
Hence, we have:

$$\sum_{i=1}^{m} f_i \frac{\varepsilon_i - \varepsilon_{eff}}{\varepsilon_i + 2\varepsilon_{eff}} = 0 \quad \text{with} \sum_{i=1}^{m} f_i = 1 \qquad \text{(I. 18)}$$

The Bruggeman EMA assumes spherical unit cells for all constituents in the mixture. This model is frequently used to describe both surface roughness [34] and porosity [35]. Only the Bruggeman EMA model is treated here, since it has been proven fairly successful for the applications described in this work.

5 Total reflectivity and transmission

A Varian Cary 5 spectrophotometer was used to investigate the optical properties of the deposited layer or multilayers on glass substrate. The total hemispherical

reflectivity at 7° angle of incidence and transmission at 0° angle were determined at room temperature in the UV, VIS and NIR over the spectral region 250-2500 nm.
The Cary 5 spectrometer is equipped with a built-in lamp powered by the base instrument, which illuminates the sample diffusely, and the reflected or transmitted flux is directed to the instrument's detection system and controlled by a computer. The integrating sphere accessory was used to optically characterise our samples. The theoretical basis for the integrating spheres or ''Ulbricht–Kugeln'' was first described in 1892 by W.E. Sumpner [36], who demonstrated that a perfectly spherical cavity, exhibiting Lambertian reflectance, would diffuse light in such a way that light reflected from the sphere wall at any point would be distributed perfectly evenly over the surface of the sphere. Ulbricht [37] was the first to used it as a photometer in 1900. Perfect spatial integration would therefore be achieved upon a single reflection, and the radiance of the indirectly illuminated sphere wall would be both uniform and proportional to the total reflected flux. Small deviations from the Lambertian ideal can be partially compensated by multiple diffuse reflections. This compensation is most effective when the sphere coating has a high reflectance, permitting a large number of reflections. The Cary integrating sphere coating is a polytetrafluoroethylene PTFE coating, high light diffusive and low light absorbent material, with a density of approximately 1 g/cm^3. PTFE coated spheres will maintain their reflectivity indefinitely if not subjected to smoke or other contaminants.

6 Optical properties of multilayer films

6.1 Solar reflectivity, solar transmission, visible reflectance

As already mentioned, a large fraction of power from the solar radiation must be transmitted through the coatings. The transparency of the film permits avoiding absorption energy losses. At the same time, the multilayer films must present a narrow reflection band in the visible range fixing the colour of the reflected light. To estimate if a multilayer coated glass sample is suitable to be used as a coloured solar

collector glass, it is characterized by its solar transmission T_{sol} and its solar reflectivity R_{sol}, defined respectively by the following relations:

$$T_{sol} = \frac{\int T(\lambda) I_{sol}(\lambda)\, d\lambda}{\int I_{sol}(\lambda)\, d\lambda} \qquad \text{(I. 19)}$$

$$R_{sol} = \frac{\int R(\lambda) \cdot I_{sol}(\lambda) d\lambda}{\int I_{sol}(\lambda) d\lambda} \qquad \text{(I. 20)}$$

$T(\lambda)$ is the transmission of the film, $R(\lambda)$ the total hemispherical reflectivity and I_{sol} the intensity of the solar spectrum AM1.5. The integration range is given by the limits of the solar spectrum. The visible reflectance R_{vis} is determined from the photopic luminous efficiency function $V(\lambda)$, the standard illumination $D_{65}(\lambda)$ and the total hemispherical reflectivity $R(\lambda)$:

$$R_{vis} = \frac{\int R(\lambda) \cdot D_{65}(\lambda) \cdot V(\lambda) d\lambda}{\int D_{65}(\lambda) \cdot V(\lambda) d\lambda} \qquad \text{(I. 21)}$$

The standard illuminant D_{65} closely resembles the relative spectral energy distribution of north-sky daylight and is accordingly important for colour specification in northern Europe. Figure 15 shows I_{sol}, V and V times D_{65} as a function of the wavelength.

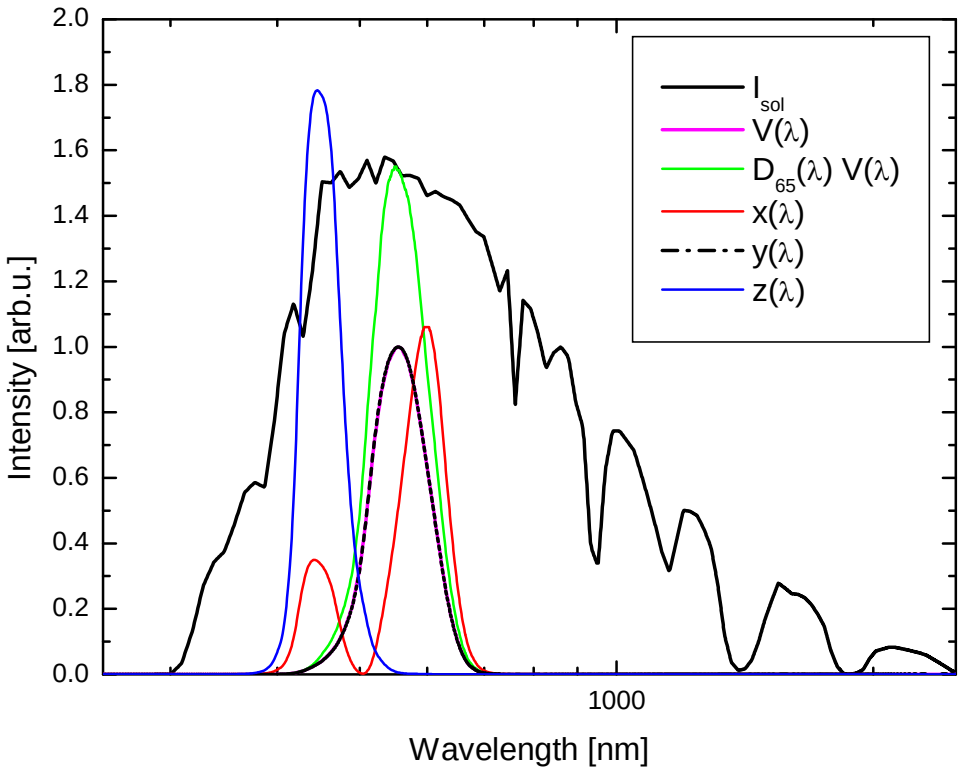

Figure 15: I_{sol}, V and V times D_{65}, and the 1931 CIE Colour Matching Functions $x(\lambda)$, $y(\lambda)$ and $z(\lambda)$as a function of the wavelength

6.2 Merit factor

Schüler et al. [38] introduced a merit factor M defined as the ratio of the visible reflectance R_{vis} and the solar reflectivity R_{sol}. Schüler studied the case of a delta-distribution-shaped reflectivity to derive the upper limit for M. M is then large for a high visible reflectance or low solar energy losses and consequently describes the energy efficiency of the visual perception.

In a more realistic approach, we suppose that the total hemispherical reflectivity $R(\lambda)$ has a Gaussian component superposed to a constant background B.

$$R(\lambda) = B + A\exp\left[-\frac{1}{2}\left(\frac{\lambda-\lambda_0}{W}\right)^2\right] \qquad \text{(I. 22)}$$

A is the height of the Gaussian component, λ_0 is the central design wavelength between 400 and 700 nm and *W* gives the Gaussian peak width. As the film is supposed to be transparent, the transmission is then given by $T(\lambda) = 1 - R(\lambda)$

In the case *B* = 0, the merit factor *M* is independent of the peak height. Fig. 16 shows the factor *M* as a function of the central design wavelength for different values of the Gaussian peak width in the case of *B* = 0. If 510 nm < λ_0 < 610 nm, Fig. 16 shows that *M* is maximum for *W* → 0 and for λ_0 = 550 nm. It should however be noted that in this case R_{vis} → 0, i.e. such a coating would not present any colour.

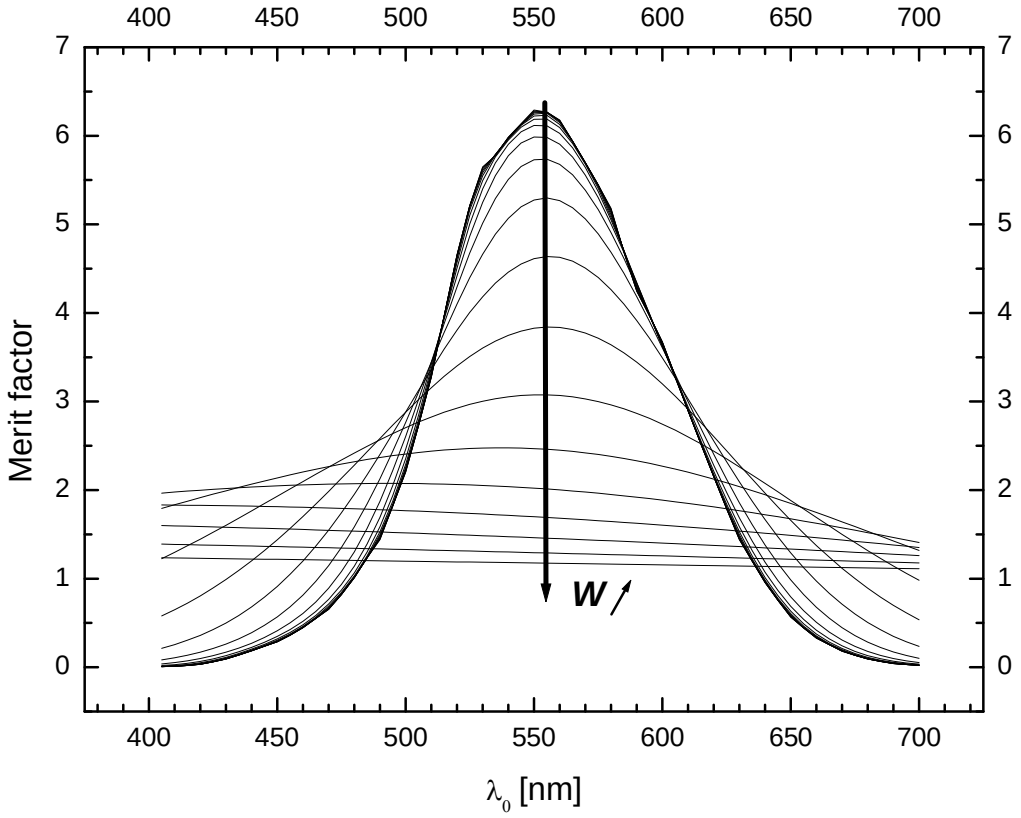

Figure 16: Factor *M* as a function of the central design wavelength for different values of the Gaussian peak width (the arrow indicates the increase of *W*)

For λ_0 < 510 nm and for λ_0 > 610, the highest merit factor is obtained for an optimal peak width W_{opt}, because the solar reflectivity R_{sol} is differently affected by a large peak than the visible reflectance R_{vis}. The value of W_{opt} decreases when λ_0 → 510 nm and increases when λ_0 → 700 nm. For the broadest peak, corresponding to a nearly constant total hemispherical reflectivity, the merit factor is practically independent of λ_0.

If the background reflectance is fixed, for example at 0.1, the merit factor depends on the height of the Gaussian peak and on its central design wavelength. Fig. 17 shows two examples (λ_0 = 550 nm and λ_0 = 700 nm) of merit factor as a function of the peak width *W*. In the first case, when the central wavelength of the reflectivity peak is near the maximum of the photopic luminous efficiency function, the curve presents a maximum which shifts towards lower width values with increasing reflectivity peak height. In the second case, a different behaviour is observed. When *W* is smaller than 105 nm, the merit factor decreases by increasing the peak height *A* and presents a minimum. A maximum is observed for larger peak widths.

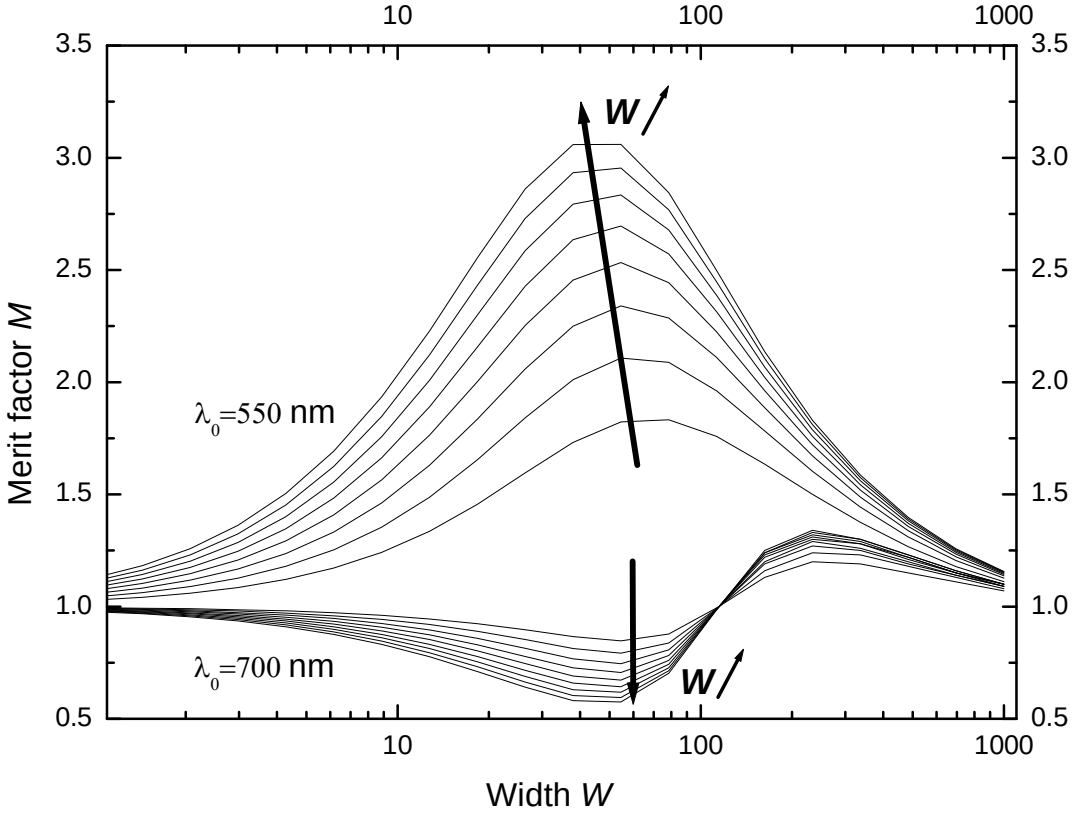

Figure 17: Merit factor as a function of the peak width W for λ_0 = 550 nm and λ_0 = 700 nm

6.3 Colour coordinates in CIE Lab system

A colour model is an abstract mathematical model describing the way colours can be represented as tuples of numbers, typically as three or four values or colour components. When formally defining a colour space, the usual reference standard is

the CIE Lab colour space, which was specifically designed to encompass all colours the average human can see. CIELAB is the most complete colour model used conventionally to describe all the colours visible to the human eye. It was developed in 1976 for this specific purpose by the International Commission on Illumination (**C**ommission **I**nternationale d'**E**clairage). The three parameters in the model represent the luminance of the colour *L* comprised between 0 (black) and 100% (white), its position *a* between red (*a* = 120) and green (*a* = -120) and its position *b* between yellow (*b* = 120) and blue (*b* = -120). All existing colour can be represented using the coordinates *L*, *a* and *b*.

The *Lab* colour model has been created to serve as a device independent, absolute model to be used as a reference. Since the Lab model is a three-dimensional model, it can only be represented properly in a three-dimensional coordinate system with *a* the red/green axis, *b* the yellow/blue axis and *L* the perpendicular luminosity axis. A useful feature of the model *Lab* however is that the first parameter is extremely intuitive: changing its value is like changing the brightness setting in a TV set.

To describe the colour of our multilayer film, we have chosen to use the three-dimensional *Lab* space 1976 (CIE Lab system). The 1931 CIE Colour Matching Functions $x(\lambda)$, $y(\lambda)$ and $z(\lambda)$ (see also Fig. 15) are used to calculate the normalized values X_x, Y_y, Z_z by integration of the spectral distribution:

$$X_x = \frac{100}{95.047}\frac{\int R(\lambda) D_{65}(\lambda) x(\lambda) d\lambda}{\int D_{65}(\lambda) y(\lambda) d\lambda} \qquad \text{(I. 23)}$$

$$Y_y = \frac{\int R(\lambda) D_{65}(\lambda) y(\lambda) d\lambda}{\int D_{65}(\lambda) y(\lambda) d\lambda} \qquad \text{(I. 24)}$$

$$Z_z = \frac{100}{108.883}\frac{\int R(\lambda) D_{65}(\lambda) z(\lambda) d\lambda}{\int D_{65}(\lambda) y(\lambda) d\lambda} \qquad \text{(I. 25)}$$

$D_{65}(\lambda)$ is the standard illuminant. We then define the quantities X_v:

$$\begin{cases} \textit{if} \quad X_x \succ 0.00886 \quad : \quad X_v = \sqrt[3]{X_x} \\ \textit{if} \quad X_x \le 0.00886 \quad : \quad X_v = 7.787 X_x + \dfrac{16}{116} \end{cases} \qquad \text{(I. 26)}$$

The quantities Y_v and Z_v are defined similarly using Y_y and Z_z, respectively. We finally have:

$$\begin{cases} L = 116\,Y_v - 16 \\ a = 500\,(X_v - Y_v) \\ b = 200\,(Y_v - Z_v) \end{cases} \qquad \text{(I. 27)}$$

REFERENCES

[1] H. Hertz, Ann. Physik 31 (1887)
[2] W. Hallwachs, Handbuch der Radiologie, Akadem. Verlagsges. Leipzig (1916)
[3] P. Lenard, Ann. Phys. 2 (1900) 359 and P. Lenard, Ann. Phys. 8 (1902) 147.]
[4] A. Einstein, Ann. Physik 17 (1905) 132
[5] K. Siegbahn (Nobel Prize in Physics), C. Nordling, A. Fahlmann, R. Nordberg, K. Hamrin, J. Hedman, G. Johansson, T. Bergmark, S. E. Karlsson, I. Lindgren, B. Lindberg, ESCA - Atomic, Molecular and Solid State Structures Studied by Means of Electron Spectroscopy, Almqvist and Wiksells, Uppsala, (1967)
[6] S. Hüfner, Photoelectron Spectroscopy (1995)
[7] M. Cardona and L. Ley, Photoemission in Solids I (1978) and Photoemission in Solids II (1979)
[8] A. Zangwill, Physics at Surfaces (1988)
[9] Stefan Hüfner, Photoelectron Spectroscopy, Springer (2003)
[10] A. Dilks, in C.R. Brundle and A.D. Baker (Eds.), Electron Spectroscopy: Theory, Techniques and Applications, Vol. 4, Academic Press, New York (1981) 277
[11] M.G. Mason, Phys. Rev. B, 27 (1983) 748
[12] S. Kohiki and K. Oki, J. Electron Spectrosc. Relat. Phenom., 36 (1985) 105
[13] J.S. Johannesen, W.E. Spicer and Y.E. Stranser, J. Appl. Phys., 47 (1976) 3028
[14] S. Thomas, J. Appl. Phys., 45 (1974) 161
[15] C.D. Wagner, in D. Briggs and M.P. Seah (Eds.), Practical Surface Analysis, Wiley, New York (1983) 477
[16] T. D. Thomas, J. Electron. Spectrosc. Relat. Phenom. 20 (1980) 117
[17] C. D. wagner, Faraday Discuss. Chem. Soc. 60 (19750) 291
[18] F.J. Grunthaner and P.J. Grunthaner, Mater. Sci. Rep., 1 (1986) 3
[19] K. Siegbahn (Nobel Prize in Physics), C. Nordling, A. Fahlman, R. Nordberg, K. Hamrin, J. Hedman, G. Johansson, T. Bergmark, S.-E. Karlsson, I, Lindgren and B. Lindberg, Nova Acta Regiae Soc.Sci., Upsaliensis, Ser. IV, Vol. 20 (1967)
[20] J.J. Yeh and I. Lindau, Atomic Data and Nuclear Data Tables 32 (1985) 1
[21] A. Schüler, C. Ellenberger, P. Oelhafen, C. Haug and R. Brenn, J. Appl. Phys. 87 (2000) 4285
[22] C. Ellenberger, Insitu Laserreflektometrie, diploma thesis (1998) University Basel
[23] S. Heavens, Optical properties of thin solid films, (New York, 1991)
[24] D. Bhattacharyya, N. K. Sahoo, S. Thakur, N. C. Das, Vacuum 60 (2001) 419
[25] D. Bhattacharyya, N. K. Sahoo, S. Thakur, N. C. Das, Vacuum 416 (2002) 97
[26] G.E. Jellison, Thin Solid Films 290-291 (1996) 40
[27] J.C. Maxwell-Garnett, Philos. Trans. R. Soc. London 203, 385 (1904); 205 (1906) 237
[28] D.A.G. Bruggemann, Ann. Phys. Leipzig 24 (1935) 636
[29] R. Landauer, in Electrical Transport and Optical Properties of Inhomogeneous Media, edited by J.C. Garland and D.B. Tanner, AIP Conf. Proc. No. 40 AIP, New York (1978)
[30] C.G. Granqvist and O. Hunderi, Phys. Rev. B 16, 3513 (1977)
[31] T. C. Choy, Effective Medium Theory, Principles and Applications, Oxford University Press (1999)
[32] J. W. Sipe, R. W. Boyd, Phys. Rev. A 46, (1992) 1614

[33] B. Wendling, Preparation and Optical Properties of Mixed Dimensional Gold-Nanostructures, Masters Thesis, UMI 2001
[34] D.E. Aspnes, J.B. Theeten and F. Hottier, Phys. Rev. B 20, (1979) 3292
[35] L.A.A. Pettersson, S. Zangooie, R. Bjorklund and H. Arwin, Mat. Res. Soc.Symp. Proc, 431 (1996) 259
[36] W. E. Sumpner, Phys. Soc. Proc. 12, (1892) 10
[37] R. Ulbricht, Elektrotech. Z. 21 (1900) 595
[38] A. Schüler, International Patent Application, WO 2004/079278, published on 16.09.2004

The results concerning TiO_2/SiO_2 stack layers for coloured glazed solar collectors are presented in this chapter. The first section deals with the interface formation by depositing titanium dioxide on a silicon dioxide substrate (TiO_2/SiO_2) or by sputtering silicon dioxide on a titanium dioxide substrate (SiO_2/TiO_2). The second section concentrates on the optical properties and ageing test of the formed multilayers on glass.

1 TiO_2/SiO_2 and SiO_2/TiO_2 interfaces

1.1 Introduction

Multilayers of transparent oxide films are widely employed as antireflection or high reflection coatings, band-pass filters, narrow-band filters in various optical and electronic devices and laser display technology [1, 2, 3, 4, 5, 6, 7, 8, 9, 10, 11, 12]. The performance of these devices strongly depends on the formed interface between the alternating oxides layers. In many applications of multilayers with discrete refractive indexes, the interface width should be as sharp as possible.

The interface formed by depositing TiO_2 on SiO_2 has received more attention than SiO_2 on TiO_2. Several research groups have studied the electronic interactions between evaporated TiO_2 and SiO_2. Gallas et al [13] investigated the interface formed when evaporating TiO_2 on SiO_2 and SiO_2 on TiO_2 by combining in-situ spectroscopic ellipsometry and X-ray photoelectron spectroscopy (XPS). They concluded that the interface of grown TiO_2 on SiO_2 was sharper than that of SiO_2 on TiO_2. Soriano et al [14] showed the presence of crystal field effects at the interface of evaporated TiO_2 on SiO_2 using X-ray absorption spectroscopy. Lassaletta et al [15] observed the presence of Ti-O-Si bonds at the interface between titanium evaporated in an oxygen atmosphere and SiO_2 layers using UV-VIS absorption spectroscopy, XPS and low-energy ion scattering (LEIS) and reflection electron energy-loss spectroscopy (REELS). Barranco et al [16] used XPS to examine the electronic interaction at the interface formed by evaporating SiO_2 on (110) oriented TiO_2. They used semiempirical quantum mechanical calculations and cluster models to explain the binding energy variations in terms of initial and final state effects.

Most of the previous studies were focused on the oxides deposited by thermal evaporation. To our knowledge, no study was dealing with the interface formed by magnetron sputtered silicon and titanium oxides. In this work, we therefore report an in-situ experimental characterization of the initial growth stage of sputtered overlayer oxide on top of a substrate oxide by systematically monitoring XPS core-level peaks of the substrate (SiO_2 or TiO_2) and the overlayer (SiO_2 or TiO_2) after each deposition step.

1.2 Experimental details

Monocrystalline (100)-oriented silicon wafers were used as substrates. Their native silicon oxide layers were etched using a Kaufman ion gun source. In the high vacuum deposition chamber pumped down to a typical background pressure below 10^{-6} mbar by a turbo pumping system, oxides were deposited at room temperature by magnetron sputtering using two water-cooled magnetrons capped by titanium and silicon targets. The magnetrons were driven by bipolar-pulsed power (50 kHz at 250 W) for the Ti target and by medium frequency RF power (100 W at 13.5 kHz) for the Si target. The target self bias was 290 V for titanium and 255 V for silicon. Both oxides were sputtered in the presence of an argon-oxygen gas mixture at a pressure of 5 x 10^{-3} mbar; the argon-oxygen partial pressure ratio was fixed at 7:1. The distances between titanium target-substrate and silicon target-substrate were fixed at 8 and 5 cm, respectively. The magnetron sources were always operated for some minutes before starting the deposition on substrates to achieve stable plasma conditions.

The growth rates for the above described deposition conditions were determined using laser reflectometry by sputtering a thick oxide film of several hundreds of nm on a silicon substrate (40x40 mm^2) from which the native oxide had been removed previously by Ar ion sputtering. The deposition rates of TiO_2 and SiO_2 were 1.4 nm/min and 0.7 nm/min, respectively, and were confirmed by ex-situ spectroscopic ellipsometry.

To study the interface between two oxides, first a 10-nm thick layer of the first substrate oxide was sputtered on a silicon sample. Thereafter, the deposition of the second overlayer oxide was made in several steps. After each deposition step the

electronic and chemical properties of atomic bonds were studied by monitoring the Ti2p, Si2p and O1s core-level peaks. As the high vacuum deposition system is connected to an ultrahigh vacuum XPS analysis chamber, the samples were subsequently transferred from one chamber to the other without breaking the vacuum to measure the Ti2p, Sip and O1s core levels. The relative concentrations of titanium, silicon and oxygen were determined by integrating the Ti2p doublet, Si2p and O1s core lines after subtracting a Shirley background [17]. From the photoionization cross-sections given by Yeh et al [18], the atomic concentration at the film's surface was calculated using UNIFIT [19].

1.3 XPS results

1.3.1 TiO_2 on SiO_2

First, to study the TiO_2 on SiO_2 interface, a 10-nm thick SiO_2 layer was grown on an (100) oriented silicon substrate (with its native oxide removed). A thin TiO_2 layer was sequentially deposited thereon and the XPS spectra were recorded after each sputtering step. Figure 1 shows the Ti2p, O1s and Si2p core-level spectra for an increasing TiO_2 thickness.

We start describing the Si2p core-level peak on the left graph of Fig. 1. The Si2p core level for the initial 10-nm thick SiO_2 layer is positioned at 104.4 eV. During the growth of TiO_2 layer, the Si2p peak vanished gradually. Furthermore, sputtering a small amount of TiO_2 on SiO_2 shifted the Si2p core level to a lower binding energy of 103.7 eV by about 0.7 eV. No further shift was detected after depositing more than 0.6-nm of TiO_2.

The O1s oxygen peak initially situated at 533.7eV (bottom spectra in the middle graph of Fig. 1) is attributed to 10-nm thick bulk SiO_2 without any TiO_2 layer. The sputtering of TiO_2 on SiO_2 leads to the appearance of another O1s peak, placed at lower binding energies and associated to the TiO_2 phase. The peak related to the TiO_2 phase begins to evolve at 532.2 eV and gains in intensity with increasing the deposited amount of TiO_2. A numerical fit procedure was used to deconvolute the O1s spectrum into two discrete peaks raising from the substrate (SiO_2) and the growing film contributions (TiO_2). The O1s peak was fitted with two symmetric peaks

corresponding to SiO_2 and TiO_2 phases, each curve convoluted with Gaussian-Lorentzian and a Shirley background (dashed line). Figure 2 shows an example of a fitted curve for 1.2-nm thick TiO_2 on SiO_2. The first peak decreases in intensity and shifts to a binding energy of 532.8 eV by increasing the TiO_2 content. This peak completely disappeared for the TiO_2 overlayer thicker than 4.2 nm. The second peak appears at a binding energy of about 532.2 eV for 0.1 nm of TiO_2 on SiO_2 and shifts to lower binding energies by about 1.4 eV for TiO_2 thicker than 4.2 nm. The initial distance between the two O1s peaks is 1.2 eV. For a TiO_2 coverage larger than 0.3 nm, the distance is 2.0 eV and remains constant [13], as summarised in Figure 3.

Next, we describe the Ti2p core-level spectra on the right graph of Fig. 1. The bottom spectrum corresponds to the SiO_2 layer on Si, and therefore no Ti2p peak is visible. Upon sputtering of titanium oxide a Ti2p doublet appeared, increased continuously in intensity and moves towards lower binding energies. A deposition of 0.1 nm of TiO_2 leads to the appearance of the Ti2p peak composed of a doublet, the $Ti2p_{3/2}$ peak being positioned at 460.0 eV. The distance between the $Ti2p_{3/2}$ and the $Ti2p_{1/2}$ peaks stays equal to 5.7 eV independently on the TiO_2 coverage. Increasing the deposited amount of TiO_2 shifts the $Ti2p_{3/2}$ peak position towards lower binding energies by about 0.7 eV. The final position of the peak $Ti2p_{3/2}$, namely 459.3 eV, is reached for a 1-nm thick TiO_2 layer on SiO_2.

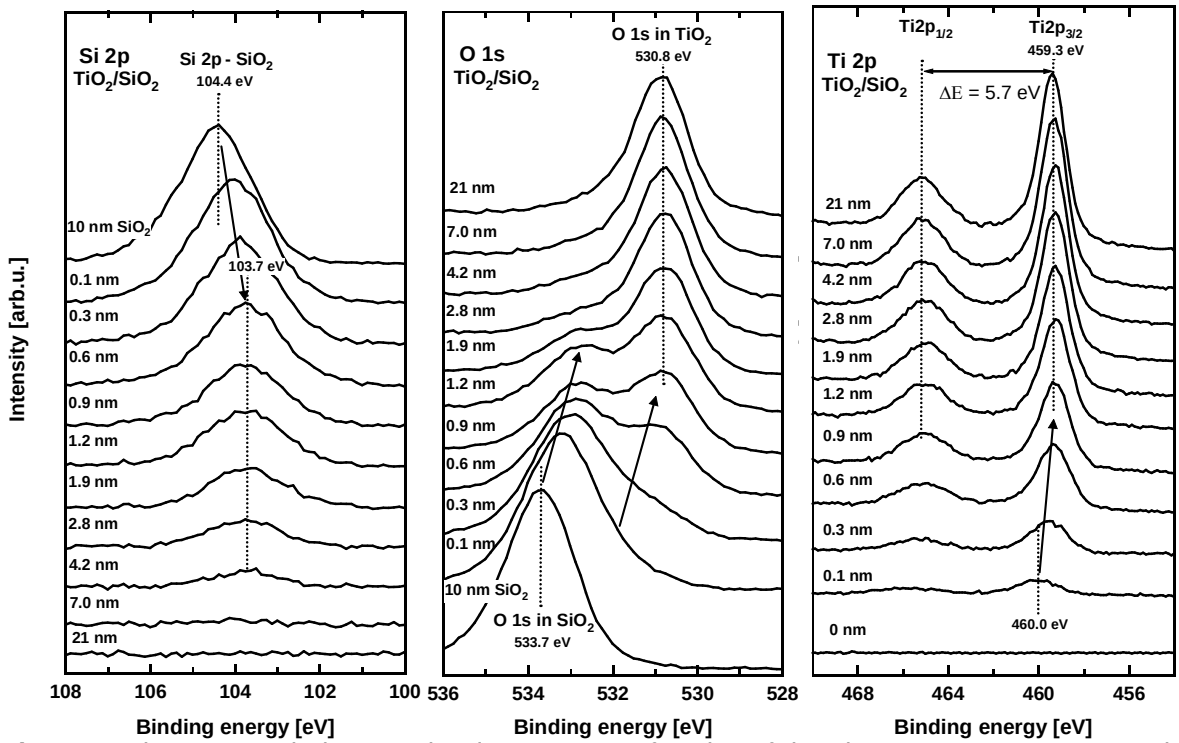

Figure 1: Si2p, O1s and Ti2p core-level spectra as a function of the TiO_2 coverage on a 10-nm thick SiO_2

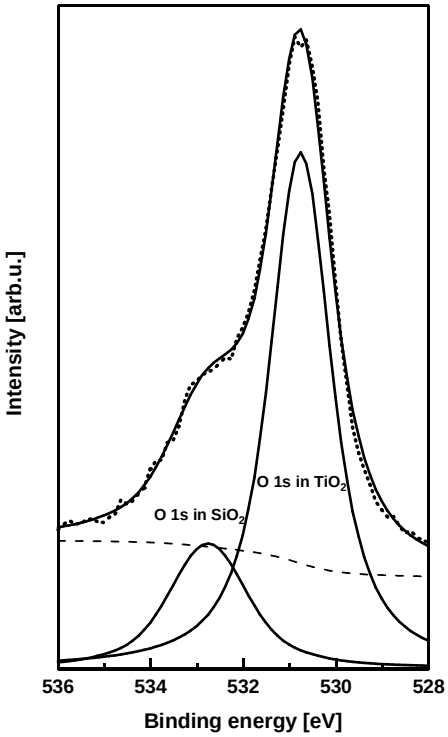

Figure 2: Deconvolution of O1s spectra obtained after sputtering 1.2 nm of TiO_2 on a 10-nm thick SiO_2 substrate after subtracting a Shirley background (dashed line)

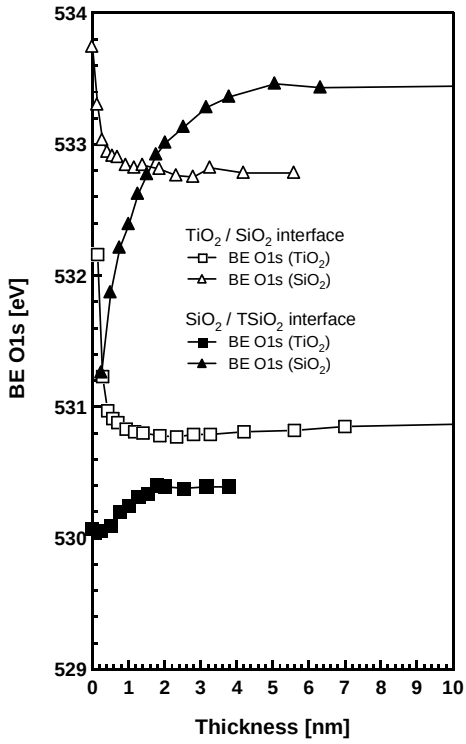

Figure 3: Binding energy of O1s related to SiO_2 and TiO_2 for both TiO_2/SiO_2 and SiO_2/TiO_2 interfaces

1.3.2 SiO_2 on TiO_2

In a complementary experiment, for a second series of samples, a 10-nm thick TiO_2 layer was grown on a (100)-oriented silicon substrate (with its native oxide removed) to study the SiO_2 on TiO_2 interface by sputtering thin SiO_2 layers and recording the XPS spectra after each deposition step. Figure 4 shows the Ti2p, O1s and Si2p core-level spectra for different thickness of the SiO_2 overlayer.

The evolution of Ti2p core level versus deposited SiO_2 thickness, on the left graph of Fig. 4, gives an idea about the substrate behaviour during its coverage by SiO_2. The initial $Ti2p_{3/2}$ core level of sputtered TiO_2 without SiO_2 layer is located at 458.6 eV. The intensity of the Ti2p peak declines with respect to the coverage thickness and the peak shifts to higher binding energies. For coverage larger than 2 nm, the shift is 0.4 eV. The energy distance between the $Ti2p_{3/2}$ and the $Ti2p_{1/2}$ peaks remains constant at 5.7 eV, independently of the SiO_2 content.

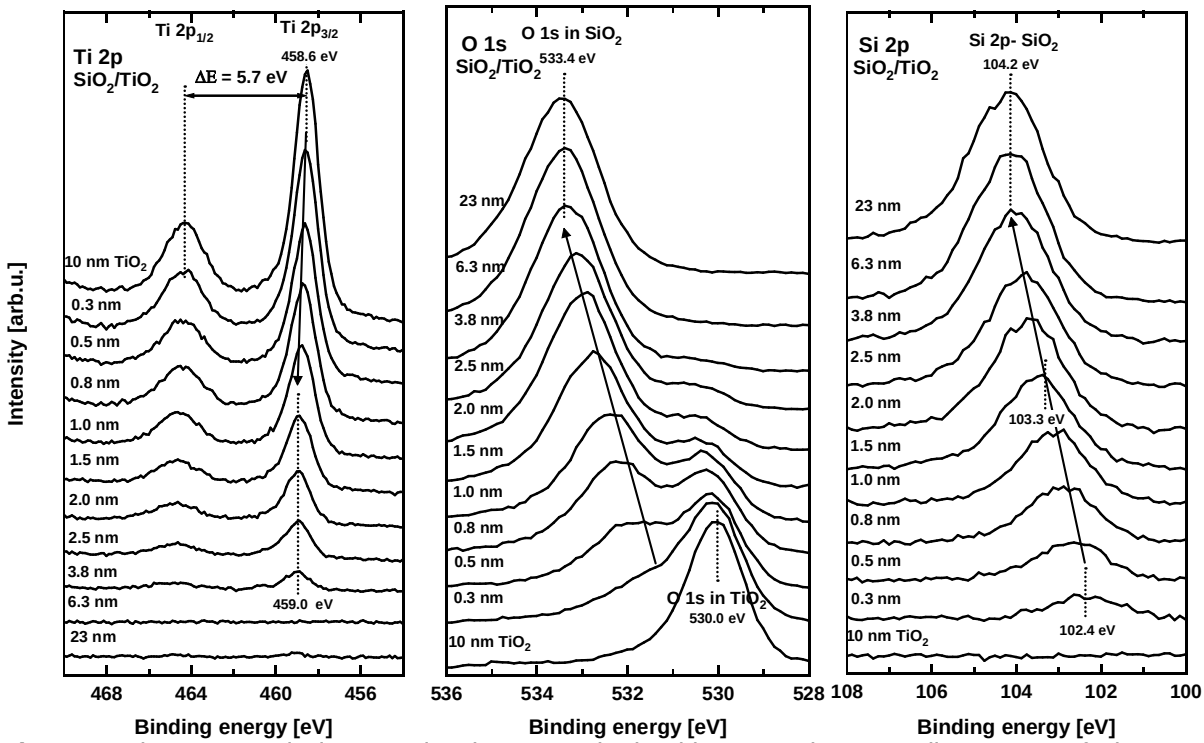

Figure 4: Ti2p, O1s and Si2p core-level spectra obtained by sputtering a small coverage of SiO_2 on a 10-nm thick TiO_2 to study the interface formed when SiO_2 is deposited on TiO_2

The O1s core level, in the middle graph of Fig. 3, corresponding to the TiO_2 phase and initially located at 530.1 eV, is getting broader by sputtering the SiO_2 overlayer. Another peak at a binding energy of 531.3 eV appears as the deposited SiO_2 film thickness on top of TiO_2 increases. The decomposition procedure reveals the

presence of the two O1s peaks attributed to SiO_2 and TiO_2 for coverage less than 7 nm. The first O1s core-level peak shifts to a higher binding energy by 0.3 eV, wherein the second peak shifts by 2.1 eV to the higher binding energy of 533.4 eV. The initial distance between the two O1s peaks is 1.7 eV. For SiO_2 coverages between 0.3 nm and 2.3 nm, this peak energy distance increases from 1.9 eV to 3.2eV (see Figure 3). The curves in the right graph of Fig. 3 represent the recorded Si2p core level on 10 nm pure TiO_2 on which small amounts of SiO_2 are deposited continuously. The binding energy of Si2p was 102.4 eV for a 0.3-nm sputtered amount of SiO_2, which is a low binding energy for Si2p in SiO_2. For SiO_2 coverage above 0.8 nm, the Si2p core-level intensity grows gradually and its binding energy value shifts by 1.9 eV from 103.3 eV to 104.2 eV.

1.4 Discussion

Charging of the sample on poorly conducting surfaces is commonly considered as an experimental obstacle to an accurate determination of binding energies for researchers engaged in the application of photoelectron spectroscopy. In highly insulating thin films, a positive charge left by the outgoing photoelectron is not compensated by electrons. Instead, a positive surface charge is built up and induces an energy shift of the whole spectrum to higher binding energies.

In the interface study of the deposition of TiO_2 on SiO_2 and SiO_2 on TiO_2, core-level shifts resulting from undesired charging effects are expected to appear for the investigated materials due to low electrical conductivity of TiO_2 and especially of SiO_2. As mentioned above, a sample charging manifests itself in a shift of the whole spectrum to higher binding energies. A binding energy calibration by aligning the recorded spectra with respect to the Si2p binding energy position at 103.4 eV or the Ti2p binding energy position at 458.6 eV (in the case of TiO_2 on SiO_2 or SiO_2 on TiO_2) was considered by several studies [13, 15, 20]. However, such a calibration process to correct charging effects does not seem to be straightforward. In our study the reported XPS spectra correspond to the rough measurement without any corrections.

1.4.1 TiO_2 on SiO_2

The obtained binding energy value of the Si2p core level at 104.4 eV for the initial 10-nm thick SiO_2 layer sputtered on Si (100) is larger than the literature bulk value and may therefore result from a charging effect. The Si2p binding energy shifts to the lower value of 103.7 eV by depositing a small amount of TiO_2 up to 0.6 nm on the SiO_2 layer. This binding energy value stays the same for deposited TiO_2 thicker than 0.6 nm. The final Si2p core-level position is quite close to the reported literature value of 103.3 eV for SiO_2.

The O1s peak related to SiO_2 shifts to lower binding energies and is located at 532.8 eV for TiO_2 thicker than 0.6 nm. The final core-level energy corresponds to the literature value. For a TiO_2 coverage below 0.6 nm, the O1s peak related to TiO_2 also moves from 532.2 eV to 530.8 eV and remains at 530.8 eV for TiO_2 coverage above 0.6 nm. The O1s overlapped curves were all fitted with two peaks (one related to SiO_2 and the other to TiO_2). We cannot exclude the presence of a third peak, but there is no evidence of its existence.

After depositing a 0.6-nm thick TiO_2 overlayer, the final binding energies of the Si2p and O1s (related to SiO_2) core levels are close to the literature values. Consequently, it is possible to conclude that an initial surface charging due to the SiO_2 layer is reduced by sputtering a TiO_2 layer thereon.

The Ti2p core-level position at 460.0 eV corresponds to a TiO_2 thickness of 0.1 nm and shifts to a lower binding energy by increasing the deposited amount of TiO_2. For coverage above 0.6 nm TiO_2, the Ti2p binding energy stays at 459.3 eV. The binding energy change of the $Ti2p_{3/2}$ peak position by 0.7 eV is consistent with the observations of Mejias et al. [20] and with the results of Lasseletta et al [15] for evaporated TiO_2 on quartz substrate and oxidised silicon. The distance between the $Ti2p_{3/2}$ and the $Ti2p_{1/2}$ peaks equal to 5.7 eV independently of the TiO_2 coverage is a strong indication that the Ti2p peak originates from Ti^{4+} in stoichiometric TiO_2.

1.4.2 SiO_2 on TiO_2

The initial binding energy of the Ti2p core level for a 10-nm thick TiO_2 layer on Si (100) is 458.6 eV. By sputtering a 1.5-nm thick overlayer of SiO_2 on top of the TiO_2 substrate layer, the Ti2p binding energy moves to the higher value 459.0 eV.

The first O1s peak related to TiO_2 and the second O1s peak related to SiO_2 both shift to higher binding energies by increasing the sputtered amount of SiO_2. For a deposited 10-nm SiO_2, the O1s peak related to SiO_2 is located at 533.4 eV. The final peak position is higher than the literature value.

The binding energy of Si2p appeared at 102.4 eV for a 0.3-nm sputtered amount of SiO_2. Such a low binding energy measured for Si2p in SiO_2 is lower than the literature value (103.3 eV) and may be explained by a deposition of not totally oxidised silicon. For SiO_2 coverage above 0.8 nm, the binding energy of the Si2p peak changes from 103.3 eV to 104.2 eV due to the sample charging.

The final binding energies of Si2p, O1s (related to SiO_2) and Ti2p are larger than the reported literature values for SiO_2. They probably result from a sample charging induced by the deposition of a SiO_2 thick dielectric layer. The same observations were made by other groups when depositing SiO_2 on TiO_2 [13, 16].

For the first sputtered SiO_2 layers, the binding energies of the Si2p and O1s (related to SiO_2) are lower than the bulk values taken from literature. This is probably due to a chemical interaction between the substrate TiO_2 and the sputtered SiO_2. The binding energies of the two mentioned core levels are in accordance with the literature only after depositing a 0.8-nm thick amount of SiO_2.

For both interfaces, the core-level positions of elements in titanium dioxide are in agreement with the literature values. The existence of a SiO_2 layer (a substrate layer or overlayer) appears to incite an undesired sample charging. However, it is possible to sort out the binding energy shift resulting from the surface charging by analysing the difference of the binding energy value of elements from the same layer, for example the Si2p and O1s peak in the case of SiO_2. Examining the difference of the binding energy of elements from the same layer should therefore provide reliable bonding information of an oxide layer deposited on other oxide film.

Figure 5 shows two graphs representing the binding energy distance Δ(BE O1s(TiO_2) – BE $Ti2p_{3/2}$) between O1s related to TiO_2 and $Ti2p_{3/2}$ core levels and the distance Δ(BE O1s(SiO_2) – BE Si2p) between O1s related to SiO_2 and Si2p core levels for TiO_2 on SiO_2 and SiO_2 on TiO_2 interfaces, respectively, as a function of deposited oxide thickness. On the first graph of Figure 5, the distance Δ(BE O1s(TiO_2) – BE $Ti2p_{3/2}$) presents a sharp decrease from 73.0 eV to 71.5 eV within a range of about 0.5 nm thick and stays constant for coverage higher than 0.5 nm while depositing

TiO_2 on SiO_2. On the second graph of Figure 4, the distance Δ(BE O1s(SiO_2) – BE Si2p) increases from 428.9 eV to 429.3 eV and then is constant for thickness higher than 1.5 nm of the deposited SiO_2 on TiO_2. It is important to note that some chemical interaction between the two oxides is happening in the first 0.5 nm and 0.8 nm of the deposited TiO_2 on SiO_2 and SiO_2 on TiO_2, respectively. Probably a formation of a mictamict alloys $Ti_xSi_yO_z$ between TiO_2 and SiO_2 oxides is taking place at the interface region [21, 22].

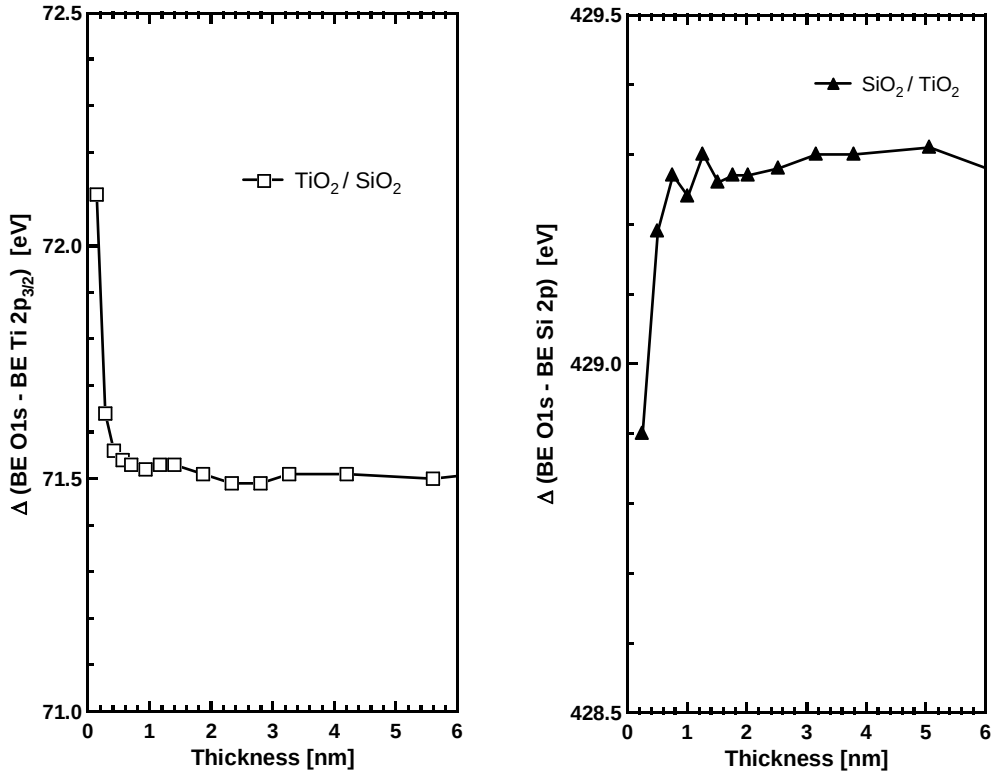

Figure 5: Distance Δ(BE O1s(TiO_2) – BE $Ti2p_{3/2}$) between O1s related to TiO_2 and $Ti2p_{3/2}$ core levels for TiO_2 on SiO_2 interface (left graph) and distance Δ(BE O1s(SiO_2) – BE Si2p) between O1s related to SiO_2 and Si2p core levels for SiO_2 on TiO_2 interface (right graph)

Figure 6 shows the binding energy difference between $Ti2p_{3/2}$ and Si2p Δ(BE $Ti2p_{3/2}$ – BE Si2p) coming from two different layers for both systems TiO_2 on SiO_2 and SiO_2 on TiO_2. It varies from 356.0 eV to 355.5 eV in the case of TiO_2 on SiO_2 interface after only some monolayers (0.5 nm) of deposited TiO_2. The variation is probably due to the presence of interface reaction between the two oxides in this region. For TiO_2 thicker than 0.5 nm, the defined distance stays constant at 355.5 eV. No charging is observed due to the conductive character of TiO_2. This distance which is close to

355.4 eV was found by Gallas et al [13], and corresponds to the situation where Ti2p is situated in the overlayer and Si 2p in the substrate.

For the SiO_2/TiO_2 interface, this distance decreases from 356.2 eV to 355. 8 eV after approximately 1-nm SiO_2 coverage due to the chemical interaction between the two oxide phases. A difference value of about 356.5 eV is attributed to mixed titanium and silicon oxides [23]. For coverage above 1 nm, the distance decreases to become constant at approximately 355.1 eV, probably due to the cumulative charging induced by the SiO_2 oxide. Such value 355 eV corresponds to non-interacting phases between SiO_2 and TiO_2 [13].

According to these results, we can confirm the presence of an interaction between oxides for deposited TiO_2 on SiO_2 and SiO_2 on TiO_2. It is difficult to estimate properly the thickness of the formed reactive interface between TiO_2 and SiO_2 oxides. The interface width for SiO_2 on TiO_2 appears to be larger than for TiO_2 on SiO_2. The same observation was made by Gallas et al [13]. Suggestively, the approximate thickness of the interfacial layer is less than 1 nm for both TiO_2 on SiO_2 and SiO_2 on TiO_2.

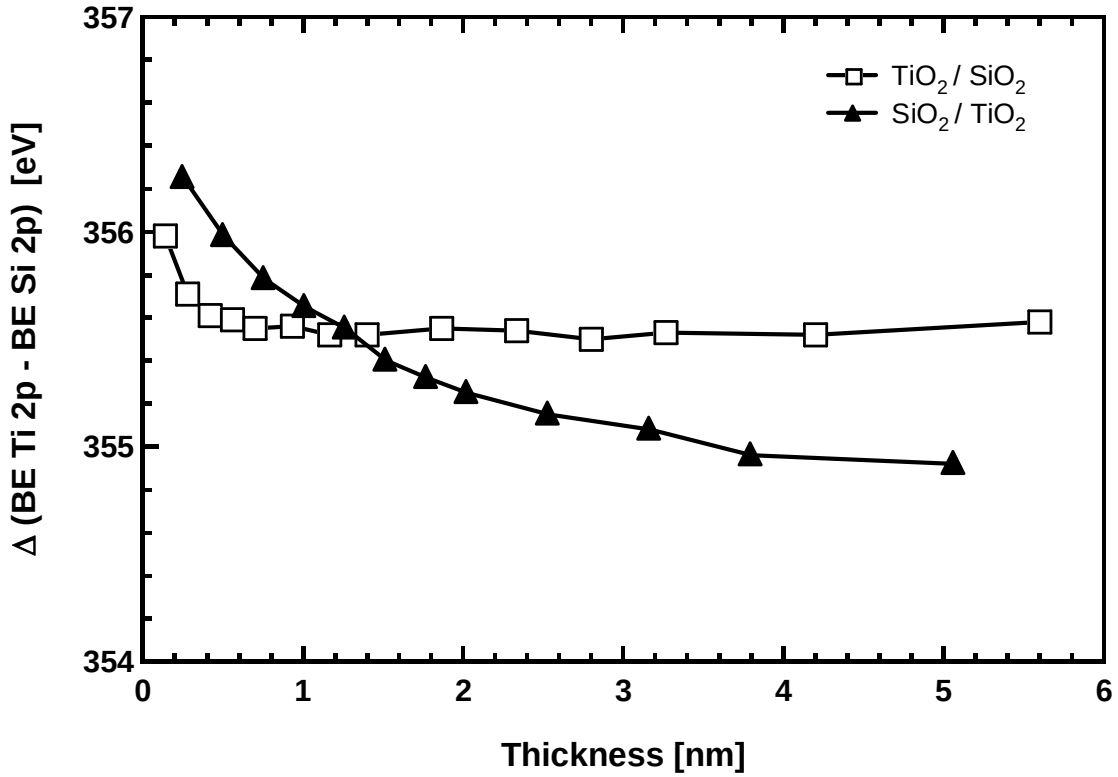

Figure 6: Distance Δ(BE Ti 2p – BE Si 2p) between Ti 2p related to TiO_2 and Si 2p related to SiO_2 core levels for both TiO_2 on SiO_2 and SiO_2 on TiO_2 interfaces

One way to extract information on the growth mode when depositing one oxide on other oxide is to plot the peak intensity of the bulk elements. In the case of a layer-by-layer growth mode the damping of the contribution from the bulk layer can be described by an exponential decreasing function, which only depends on the mean free path of the electrons in the overlayer and its thickness [15]. Figure 7 shows a semi-logarithmic plot of the respective bulk element core-level intensities as a function of the deposited layer thickness. In the case of a sharp interface, we should expect a straight line.

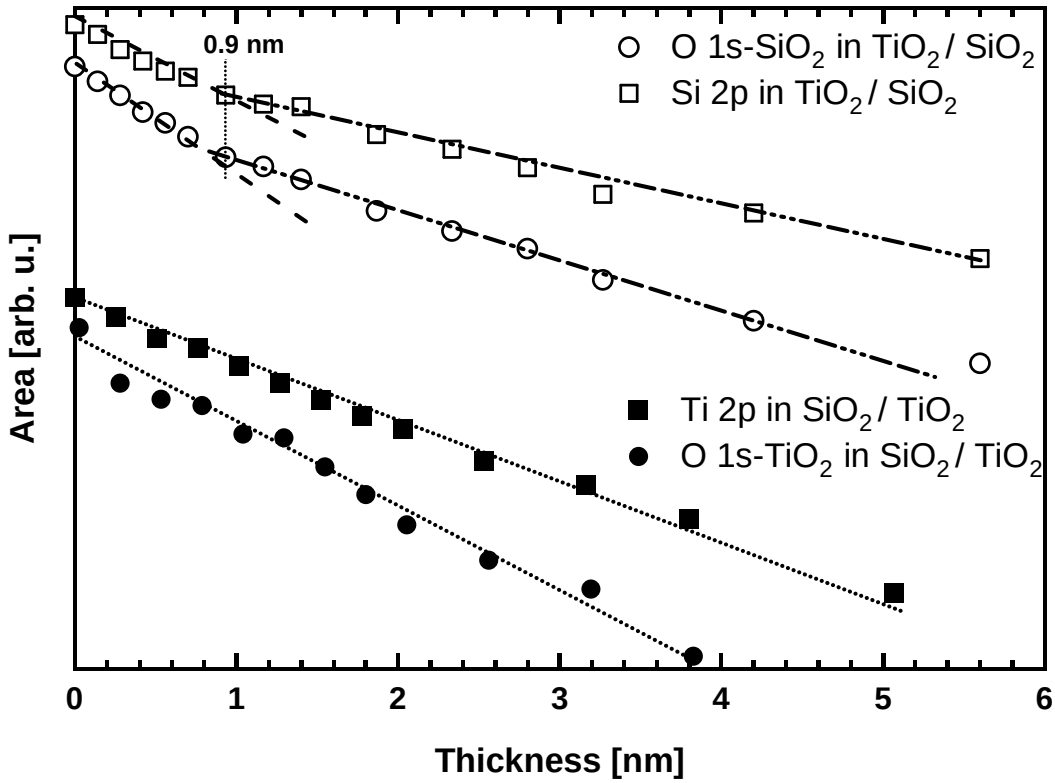

Figure 7: Si 2p, O1s in SiO_2 core levels area in a logarithmic scale as a function of the deposited TiO_2 on 10-nm SiO_2 (the open markers) and Ti 2p and O1s in TiO_2 core levels area as a function of the deposited SiO_2 on 10-nm TiO_2 (the solid markers)

For TiO_2 on SiO_2 interface, the logarithm of the Si2p intensity as a function of coverage shows two linear slopes: one for less than 0.9 nm thick and another for more than 0.9 nm thick. The same tendency is observed for the O1s intensity related to SiO_2. This change of the slope might be related to the formation of mixed oxide for the sputtered TiO_2 less than 0.9 nm. Above 0.9-nm TiO_2 thick, the TiO_2 layer grows layer by layer on the top of the formed interface zone. For SiO_2 on TiO_2 interface no significant slope change is observed for the represented Ti2p and O1s core-level

intensity as a function of coverage. The growth mode of the mixed oxides of TiO_2 and SiO_2 formed directly at the top of TiO_2 layer and that of pure SiO_2 are probably similar.

1.5 Conclusion

We studied the deposition of TiO_2 on SiO_2 and SiO_2 on TiO_2 using photoelectron spectroscopy by measuring Ti2p, O1s and Si2p core levels. We calculated a distance between the core levels of the elements of the deposited layer and the substrate. An interfacial reaction took place in both cases. The deposition process of an oxide on another oxide is dominated by two stages. In the first stage an interface is formed due to the interaction between two different oxides. The second stage is described by the formation of a stoichiometric oxide whose properties correspond to that of the bulk. The amount of oxide needed to achieve the bulk depends on the substrate.

Firstly, we looked at the bi-layer system by plotting the distance Δ(BE O1s(TiO_2) – BE $Ti2p_{3/2}$) between O1s related to TiO_2 and Ti2p core levels and the distance Δ(BE O1s(SiO_2) – BE Si2p) between O1s related to SiO_2 and Si2p core levels for TiO_2 on SiO_2 and SiO_2 on TiO_2 interfaces, respectively. Secondly, we represented the binding energy difference between $Ti2p_{3/2}$ and Si2p Δ(BE $Ti2p_{3/2}$ – BE Si2p) as a function of thickness for both systems, which confirmed the presence of mixed oxide the first monolayers while depositing TiO_2 on SiO_2 and SiO_2 on TiO_2.[2] Finally, a semi-logarithmic plot of the substrate element core-level intensities was used to determine the interface width. The experimental results gave an estimation of the formed interfacial zone between TiO_2 and SiO_2 oxides, which is less than 1 nm for both systems (TiO_2 on SiO_2) and (SiO_2 on TiO_2). Once the interface is formed a layer-by-layer growth is observed for sputtered TiO_2 on SiO_2.

Therefore we believe that TiO_2/SiO_2 multilayers are suitable for optical application due to the thin interfacial zone formed during sputter deposition of TiO_2 on SiO_2 and of SiO_2 on TiO_2.

2 TiO_2 – SiO_2 multilayers for coloured glazed solar collectors

2.1 Introduction

Dielectric TiO_2 and SiO_2 thin films have been used in a variety of applications, such as high-reflection mirrors [1], waveguides [3], narrow-band filters [4], dyes [24] and antireflection or high reflection coatings [2]. The performances of these devices are based on interference effects by alternating layers of high and low refractive indexes. Different optical properties are obtained by depositing multilayers of two different materials. The optical properties of each layer have to be reproducible. The interface between the two layers should be as smooth as possible. Evaporation coating technique underwent rapid development and became a standard method for optical coating [25]. Afterwards, alternative methods, such as chemical vapour deposition [26], dip coating [27], sol gel method [28] and reactive sputtering [29] were extensively studied. The later allows large area coatings and thickness uniformity combined with high rate deposition [30].

TiO_2 is one of the most interesting dielectric materials since it is transparent to visible light, and has a high refractive index (at λ = 550 nm n = 2.54 for anatase and 2.75 for rutile), low absorption [31] and good hardness, and forms a stable device with SiO_2 in discrete and mixed coatings [32]. SiO_2 is a low-index material and transparent from the UV to the NIR [33]. TiO_2–SiO_2 systems have been extensively used to realise a wide variety of optical devices. Ouellette et al, reported on a TiO_2–SiO_2 notch filter prepared by ion beam reactive sputtering [4]. Wong et al reported the possibility of preparing an optical reflection filter using Helicon plasma sputtering [34]. They realised multilayers with a wide range of refractive indexes from (n = 1.47 to 2.2) by mixing TiO_2 and SiO_2.

In the current work, an experimental study for the preparation of optical multilayer coatings based on TiO_2–SiO_2 dielectric films is reported. A combination of different refractive indexes and thicknesses make possible a wide range of reflected colours with an acceptable solar transmission. In the following section, we will concentrate on the optical properties of several types of layers on silicon (Si) and glass (G)

substrates. The ageing test is also reported for the five multilayered TiO_2–SiO_2 systems on glass.

2.2 Thin film deposition

The high vacuum chamber used for the dielectric coatings deposition was pumped down to a typical background pressure below 10^{-6} mbar by the turbo pumping system. The sputtering was carried out in a deposition chamber, using two water-cooled magnetrons. One magnetron was capped by a titanium target and the other by a silicon target. The magnetrons were driven by bipolar-pulsed power (50 kHz at 250 W) for the Ti target and by medium frequency RF power (100 W at 13.5 kHz) for the Si target.

During the thin film deposition carried out at room temperature, an argon-oxygen gas mixture was used as process gas and mass flow ratio argon/oxygen was always set to 7:1. A working pressure of around 5 x 10^{-3} mbar was adjusted by throttling the pumping system. Deposition conditions were always run during the 4 min before starting the deposition on the substrate to achieve stable plasma conditions. Thin TiO_2 and SiO_2 films were deposited either on glass AF45 or on monocrystalline (100)-oriented silicon (with its native oxide) substrates (area 40x40 mm^2) for the various optical characterisation techniques. Silicon substrates were used for in-situ real-time laser reflectometry and ex-situ ellipsometry, while glass substrates were used for ex-situ spectrophotometry. In-situ photoelectron spectroscopy of the thin films deposited on sputter cleaned copper substrates were performed to check the stoichiometry of the films.

2.3 Laser Reflectometry

Real-time laser reflectometry was performed simultaneously during the deposition of single dielectric layers on silicon substrates. Figure 8 shows the acquired reflectivity data during the deposition of stoichiometric TiO_2 and SiO_2. The polarisation of the laser light was parallel to the plane of the reflection (*p* polarized).

The resulting curves exhibit an oscillating behavior (two maxima and one minima for TiO_2; two maxima and two minima for SiO_2 in the case of Figure 8). For transparent

films the oscillations amplitude does not attenuate during the deposition of a thick film. As the maxima show the same value of reflectivity, the extinction coefficient *k* is zero, as expected. We can directly deduce that the deposited films are transparent for both films TiO_2 and SiO_2. A quantitative determination of the optical constants is done by a numerical fit to the experimental data by using the formula for the reflectivity in the case of a single layer on a substrate. The fit is represented as a dashed line in Figure 8.

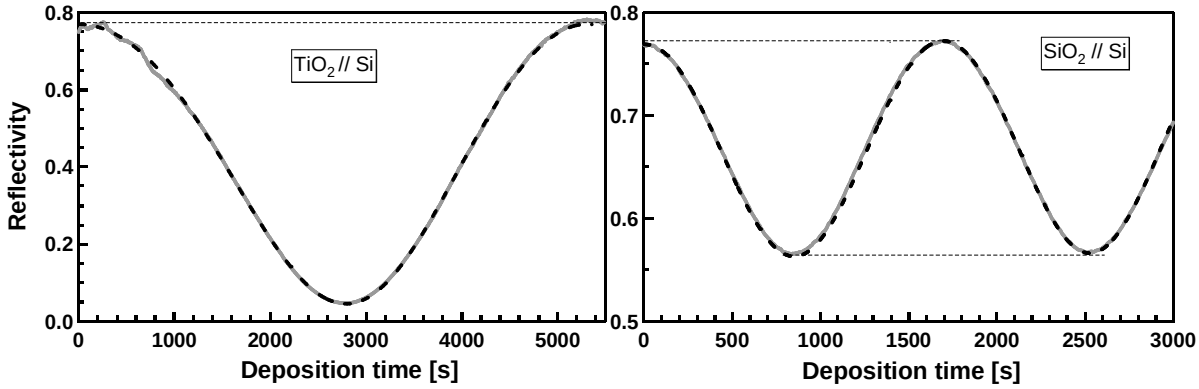

Figure 8: Real-time laser reflectometry curves of sputtered TiO_2 on Si (left) and SiO_2 on Si (right). The solid curves correspond to the experimental data, the dashed ones to the fit curves

In a straightforward way, laser reflectometry provides important information such as growth rate (1 nm/min for TiO_2 and 7.6 nm/min for SiO_2) and refractive *n* (2.20 for TiO_2 and 1.47 for SiO_2) at one wavelength (532 nm).

2.4 Ellipsometry

As the optical ellipsometric characterization of an individual layer needs the choice of the appropriate model, the modelling of multilayer thin films is an even more complex task. The standard approach using reference data in the literature for the dielectric functions could not be applied.

We made a systematic study of the optical properties of individual dielectric layers, then of the more complex system of 2, 3, 4 and 5 layers. In this study, at first the model consists of a single homogeneous dielectric film on a semi-infinite silicon substrate with its 2-nm thick native oxide. The native silicon oxide interlayer was included in the model. Surface roughness was neglected. Silicon and native silicon oxide optical functions were taken from the literature [35]. The ambient refractive

index is n_{amb} = 1. The experimental data was fitted with a widely used Cauchy dispersion formula for both TiO_2 and SiO_2 oxides. For the multilayered sample, only the thicknesses were allowed to fluctuate during the fit procedure.

2.4.1 Single layers on silicon substrate

Figures 9 and 10 show the measured ellipsometric data ψ and Δ for deposited single layer of TiO_2 and SiO_2 on silicon substrates and the best theoretical fits using the Cauchy dispersion model. The collected data range between 350 to 850 nm for different incident angles from 40° to 70°. For better visibility, the measurements and fits were plotted by solid and dashed lines, respectively. A good agreement between the fit and the experimental data is observed, except below 350 nm. The best Cauchy parameters fit in the wavelength range 350-850 nm for TiO_2 individual layer are n_0 = 2.38, n_1 = -899 nm^2, n_2 = 1781 nm^4, $k_0 = k_1 = k_2 = 0$ and for SiO_2 individual layer are n_0 = 1.46, n_1 = 25.3 nm^2, n_2 = 17.5 nm^4, $k_0 = k_1 = k_2 = 0$. The results of the fit parameters confirm that no absorption occurs in the films. The sputtering rate was (0.97 nm/min for TiO_2 and 7.2 nm/min for SiO_2) and refractive index n was (2.28 for TiO_2 and 1.47 for SiO_2) at the wavelength of 532 nm. It should be noted here that the growth rates and refractive indexes at 532 nm of both TiO_2 and SiO_2 are in good agreement with the one measured by the laser reflectometry.

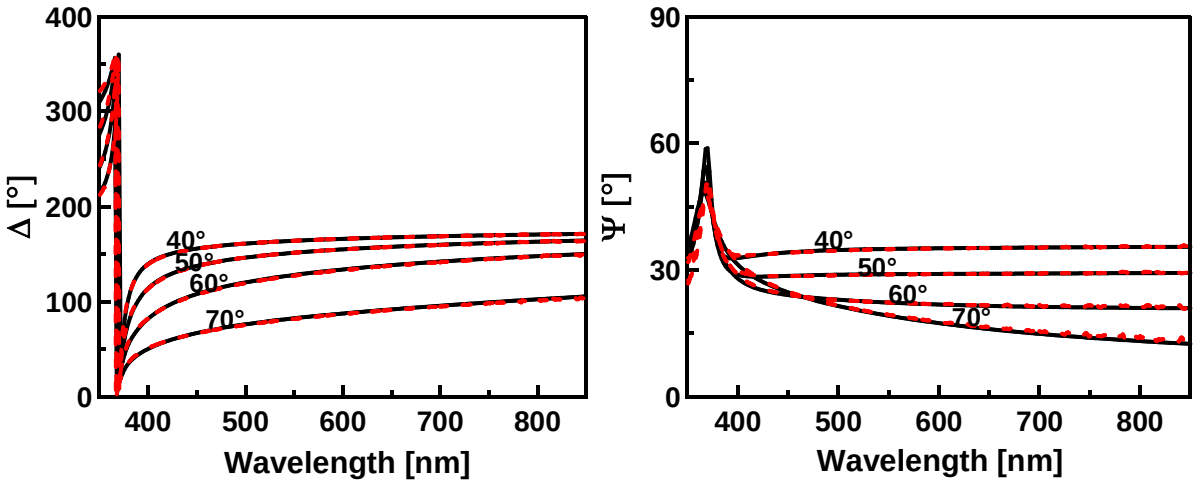

Figure 9: Ellipsometric spectrum of sputtered TiO_2 on silicon substrate

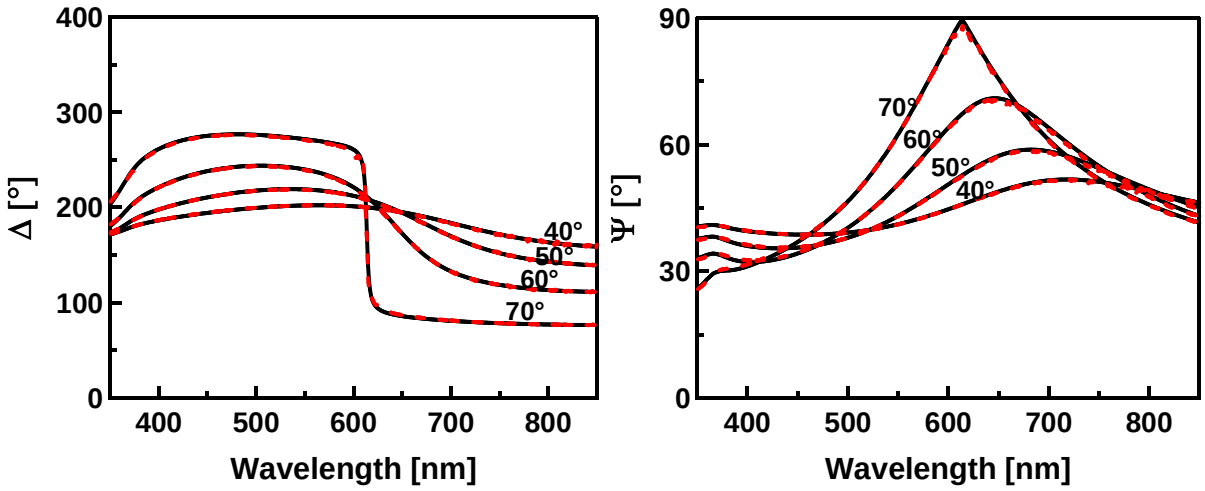

Figure 10: Ellipsometric spectrum of sputtered SiO_2 on silicon substrate

Figure 11 show the refractive index *n* as a function of the wavelength in the UV-Vis for TiO_2 and SiO_2 on silicon substrate as the result of the fit to the ellipsometric measurements. The refractive index of titanium dioxide is lower than the crystalline material (n= 2.9) but corresponds to the obtained one by sputtering technique [36]. The material density influences the refractive index value, which is expected to be lower than in the bulk of crystalline material. In the case of sputtered silicon dioxide the obtained refractive index is the same as the one reported by Palik [35].

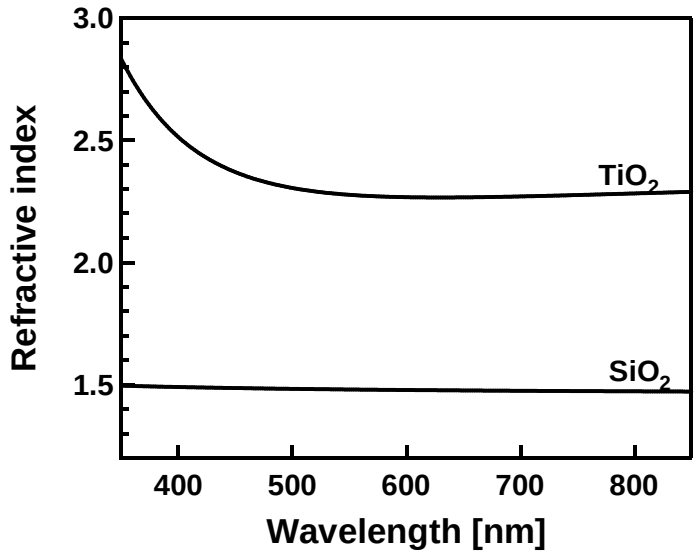

Figure 11: Refractive index dispersion of sputtered TiO_2 and SiO_2

2.4.2 Multilayers on silicon substrate

We then used the optical properties of individual layers of TiO_2 and SiO_2 to fit the ellipsometric functions of sample comprising two or more alternating oxide layers deposited on a silicon substrate. The fit parameters were then only the layer thicknesses. Figures 12-15 show the measured ellipsometric functions ψ and Δ and the corresponding fits for multilayered films with respectively 2, 3, 4 or 5 alternating layers.

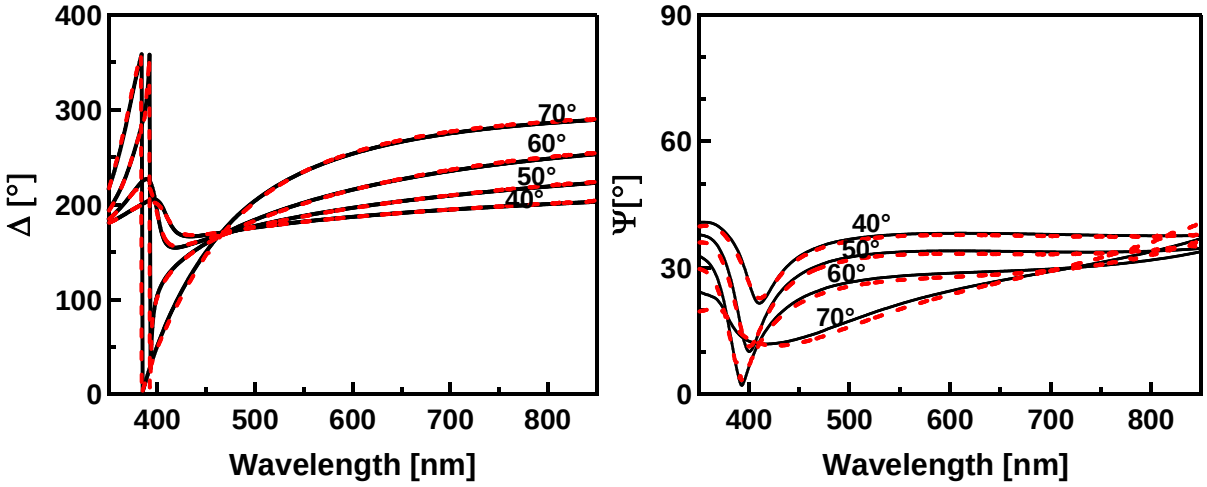

Figure 12: Ellipsometric spectrum of SiO_2 / TiO_2 // Si sample. The dashed line is the measure and the continuous line the fit

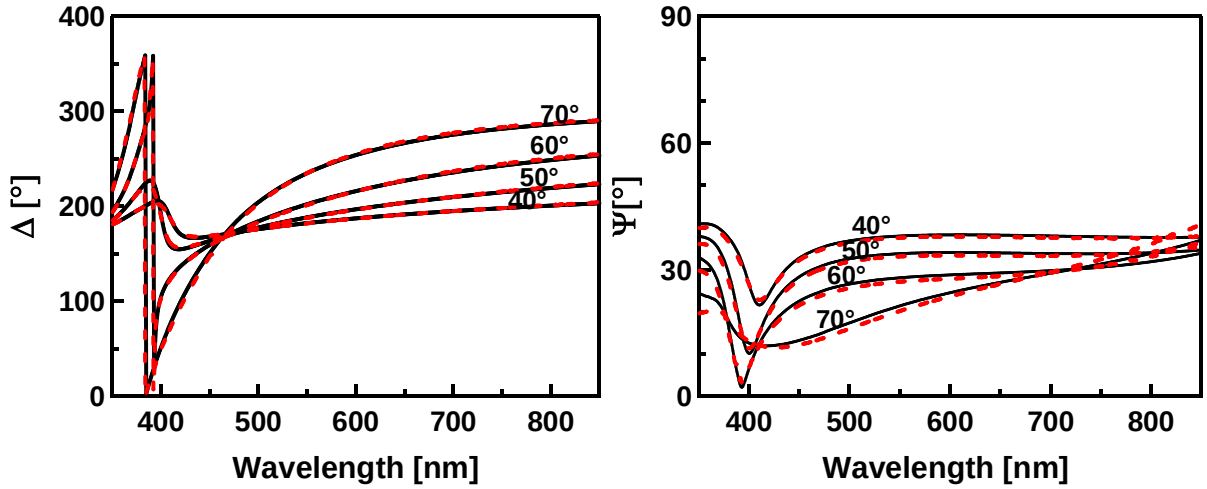

Figure 13: Ellipsometric spectrum of TiO_2 / SiO_2 / TiO_2 // Si sample. The dashed line is the measure and the continuous line the fit

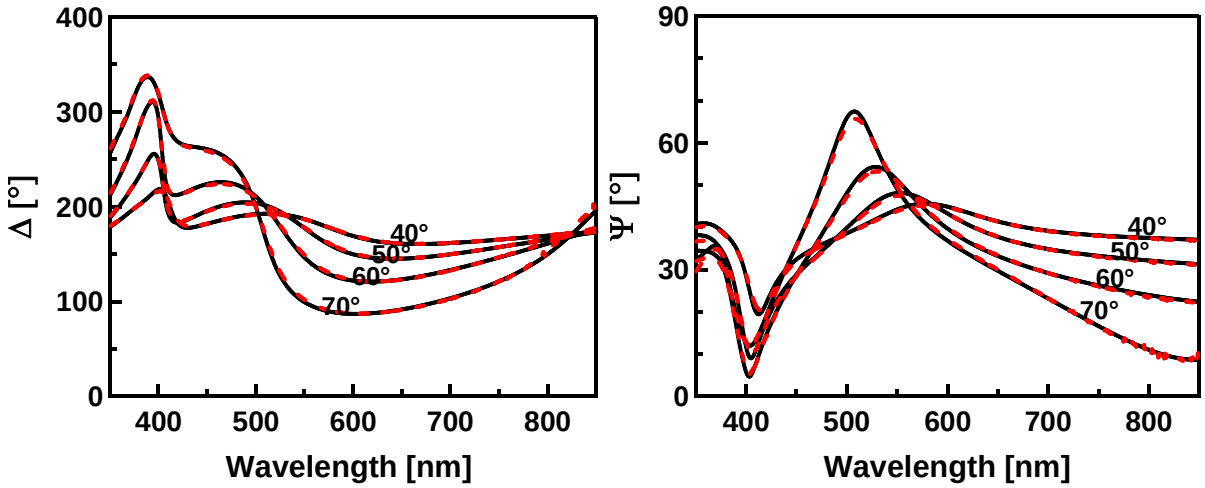

Figure 14: Ellipsometric spectrum of SiO_2 / TiO_2 / SiO_2 / TiO_2 // Si sample. The dashed line is the measure and the continuous line the fit

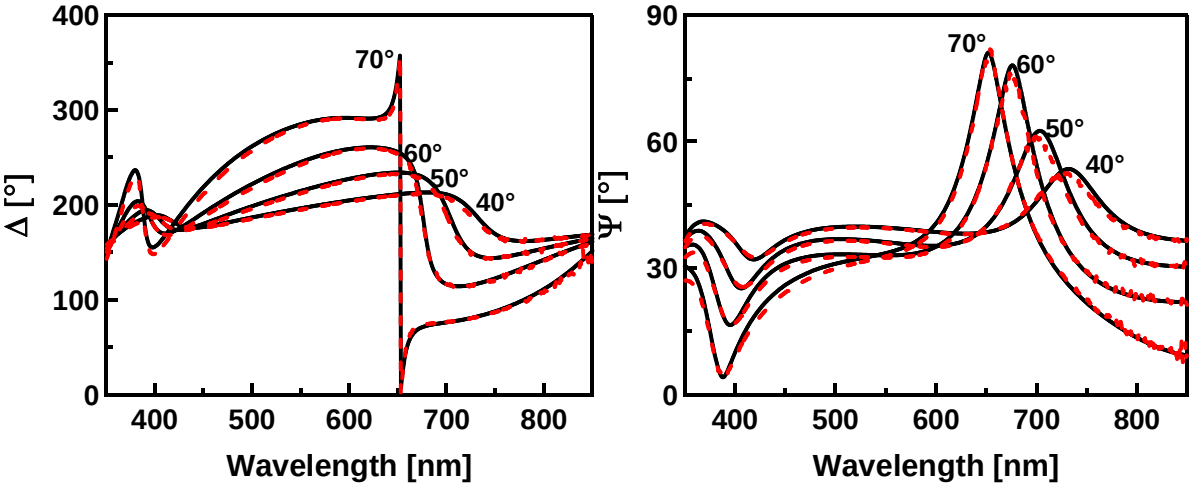

Figure 15: Measured ellipsometric spectra of SiO_2 / TiO_2 / SiO_2 / TiO_2 // Si sample. The dashed line is the measure and the continuous line the fit

We observed a good agreement between the experimental and the fitted data. Table 1 shows the expected layer thicknesses calculated by the deposition velocities deduced from laser reflectometry and ellipsometry for individual layers and the fitted thickness for the multilayer samples with 2, 3, 4 and 5 layers. The good agreement between the data indicates reproducible sputter deposition and optical properties of the dielectric materials as well as the validity of our model with abrupt interfaces between the SiO_2 and TiO_2 layers.

Layer (L) number	Thickness by Laser Reflectometry (nm)	Thickness by Ellipsometry (nm)	Fit results (nm)
1L TiO_2	30	31	31
1L SiO_2	140	133	133
2L	-	-	30/129
3L	-	-	27/132/29
4L	-	-	30/132/27/131
5L	-	-	28/128/28/126/29

Table 1: Deduced thickness by ellipsometry and laser reflectometry for individual layers and of the TiO_2–SiO_2 multilayers (of figures 12-15) by the fit procedure.

2.5 Transmission Electron Microscopy

Figure 16 shows the cross-section image of the same five layered system which is mentioned above. The layer on the bottom of the image is the monocrystalline silicon substrate with the native oxide layer of about 2 nm. The dark layers are the sputtered titanium oxide, while the bright layers are the sputtered silicon oxide layers. The amorphous SiO_2 layers appear structurally uniform and featureless. The first TiO_2 layer deposited directly on silicon substrate appears structurally uniform. The following TiO_2 layers seem to be porous and columnar with axes parallel to the growth direction.

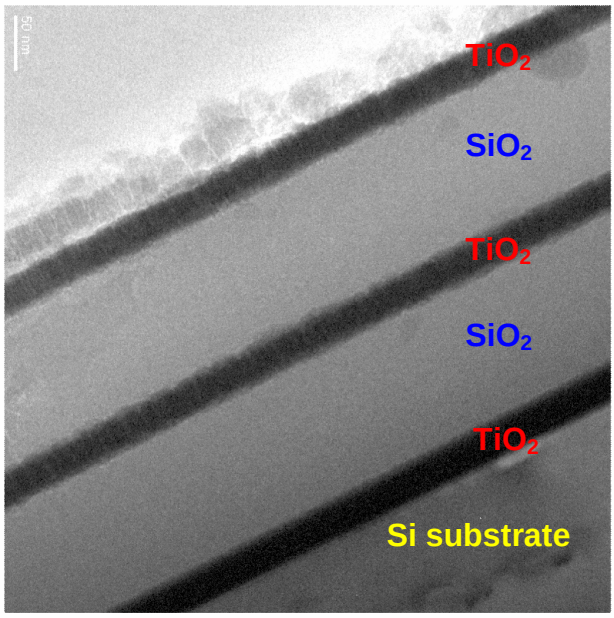

Figure 16: TEM cross section image of the multilayered TiO_2–SiO_2 film on silicon

Figure 17 shows the film thicknesses of five layered TiO_2–SiO_2 obtained using two different methods, nondestructive spectroscopic ellipsometry and destructive transmission electron microscopy. The thickness deviation between the two methods is within 5% for SiO_2 and 10% for TiO_2. The good agreement result of the two methods confirms the feasibility and the control of the multilayer thickness using sputtering deposition process.

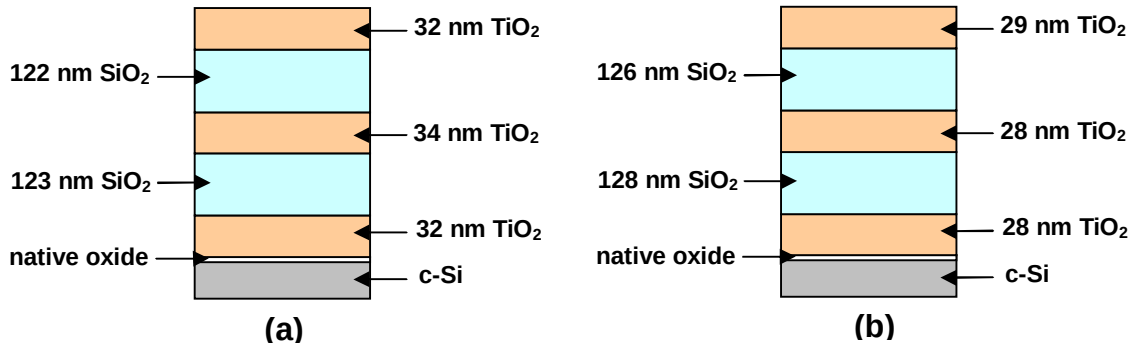

Figure 17: Thickness of five alternative TiO_2 and SiO_2 sputtered layers on silicon deduced from cross section TEM image (a) and from the fit of the ellipsometric data (b)

2.6 Simulation

2.6.1 Solar transmission and visible reflectance

After controlling the optical properties and the growth velocities of both TiO_2 and SiO_2 oxides, it was then possible to estimate the optical parameters of a multilayered coating as a function of the thickness of the employed oxides. The solar transmission T_{sol} as well as the visible reflectance R_{vis} are the most important parameters for the TiO_2–SiO_2 multilayers for their application on coloured glazed solar collectors. It is of great interest to know how many layers are needed to achieve a high solar transmission (more than 85%) and at the same time a high visible reflectance (larger than 12%). To meet the fixed goal, we simulated with the software *Advanced Fit* the optical properties of TiO_2–SiO_2 multilayered systems formed by three or five alternating layers on glass. The obtained refractive index dispersion of individual layers TiO_2 and SiO_2 by ellipsometry spectroscopy were used (Figure 11) to realise the simulation. The results, solar transmission and visible reflectance, are

represented in cartographic form on Figures 18 and 19 for varying thicknesses of TiO_2 and SiO_2 layers ranging from 10 to 100 nm and from 10 to 300 nm, respectively.

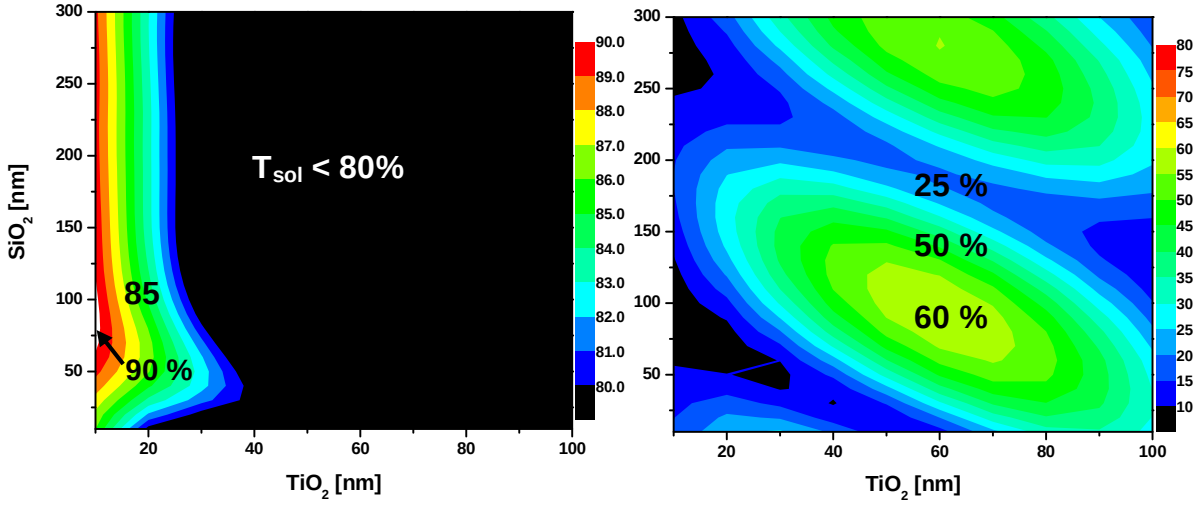

Figure 18: Solar transmission (left) and visible reflectance (right) cartographies for 3-layered sample $TiO_2/SiO_2/TiO_2$//Si depending on the thicknesses of TiO_2 and SiO_2

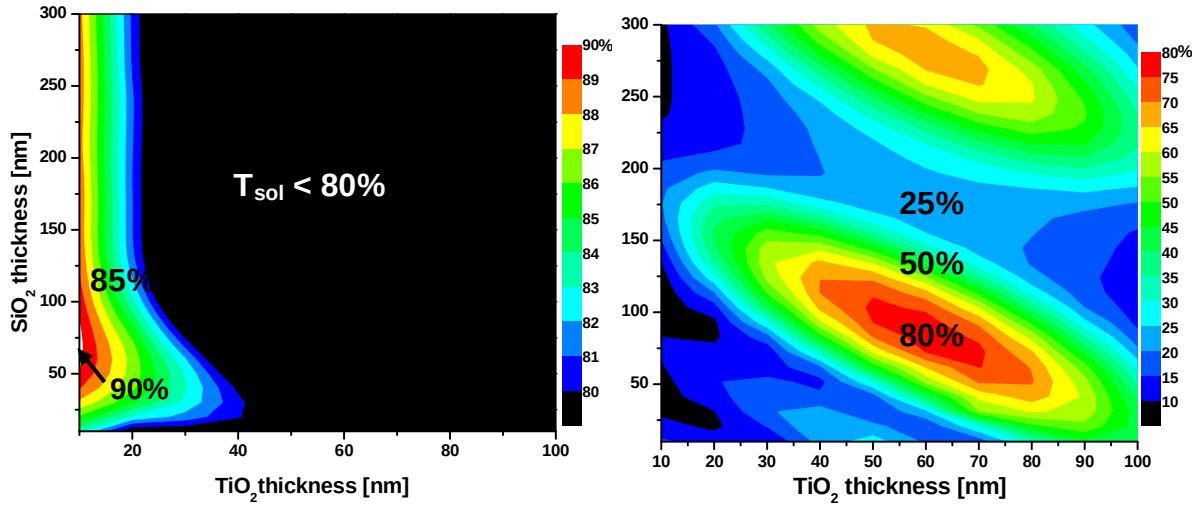

Figure 19: Solar transmission (left) and visible reflectance (right) cartographies for 5-layered sample $TiO_2/SiO_2/TiO_2/SiO_2/TiO_2$//Si depending on the thicknesses of TiO_2 and SiO_2

A TiO_2 thickness larger than 25 nm results in a solar transmission less than 85% and a visible reflectance larger than 35%. The best compromise between a high solar transmission (more than 85%) and the sufficiently high visible reflectance (more than 12%) is found for a TiO_2 thickness less than 25 nm and a SiO_2 thickness between 140 and 200 nm. These cartographies show that adding layers has a strong effect on increasing the visible reflectance value but reducing at the same time the area where the solar transmission is higher than 85%.

2.6.2 Peak position of the reflectivity curves

Once the optimized thickness of the individual layers for the 5 layered TiO_2–SiO_2 film is obtained, it was important to know at which wavelength the peak maximum is situated in the total reflectivity curve to deduce the reflected colour of the multilayered film on glass. Figure 20 presents the peak position depending on the thickness of TiO_2 (from 10 to 20 nm) and SiO_2 (from 140 to 200 nm) under a normal illumination. This cartography allows us to choose the desired reflected color ranging from the blue to the red. The ab color coordinates corresponding to the 5 layered films is represented in Figure 21. The TiO_2 and SiO_2 thicknesses are reported inside the graph. Different reflected color from the 5 layered films under normal illumination can be obtained, depending on the TiO_2 and SiO_2 thickness.

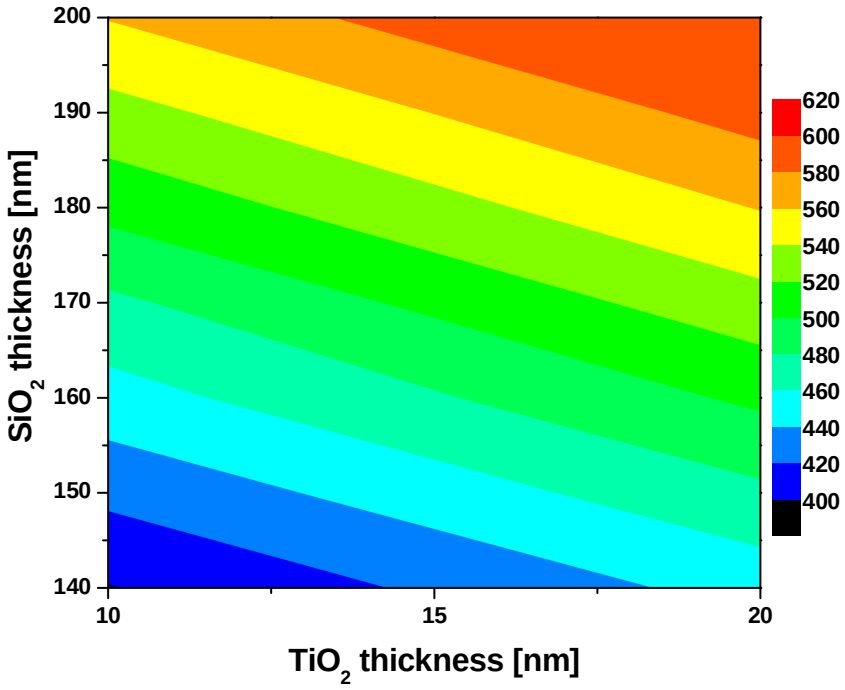

Figure 20: Cartographies of the peak position of the total reflectivity curves for 5 layered sample $TiO_2/SiO_2/TiO_2/SiO_2/TiO_2$//Si having a higher solar transmission than 85% and a pronounced visible reflectance between 20-40% as a function of the TiO_2 and SiO_2 thicknesses

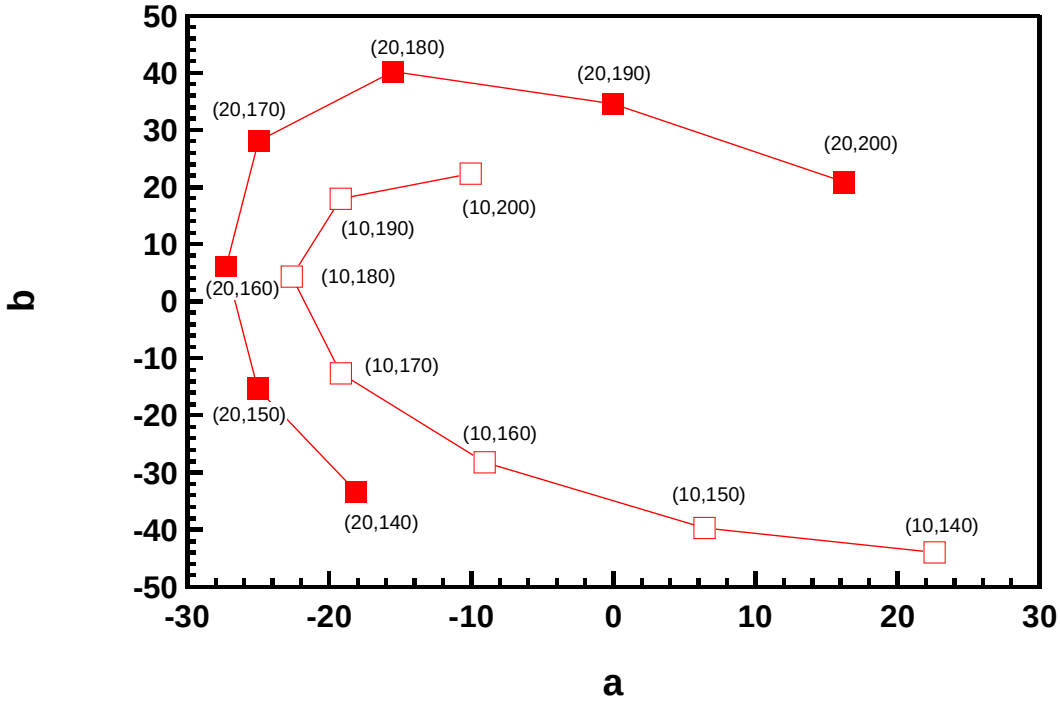

Figure 21: ab colour coordinates in LAB system for the 5 layered sample $TiO_2/SiO_2/TiO_2/SiO_2/TiO_2$//Si under a normal illumination. The thicknesses range between 10 and 20 nm for TiO_2 layer and 140 and 200 nm for SiO_2 layer.

2.7 Experimental realisations and ageing tests

Based on the simulation results, we experimentally realised a couple of multilayered films with the best compromise. Figure 22 shows the experimental total hemispherical reflectivity and transmission of three different samples with a fixed thickness of TiO_2 at 15 nm and that of the SiO_2 between 160 and 200 nm. The position of the reflected peak shifts to a higher wavelength when the thickness of SiO_2 is increased. The solar transmission of the three different samples is in the order of 85%. Hence, we obtained a solar transmission 7% lower than that of the uncovered glass, combined with a pronounced visible reflectance. Different colours of the reflected light can be obtained by slightly changing the TiO_2 and SiO_2 thicknesses.

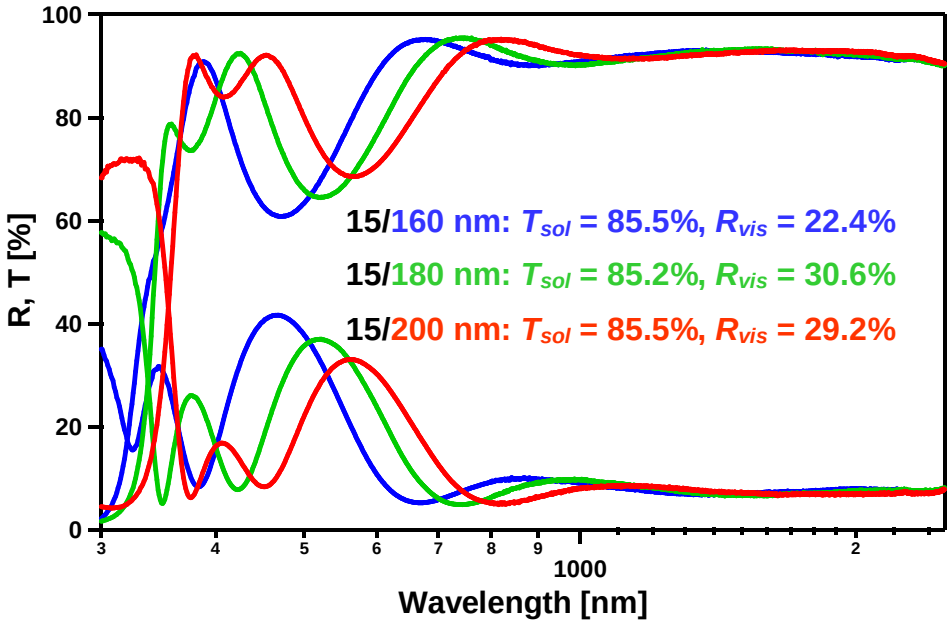

Figure 22: Total hemispherical reflectivity and transmission of three different 5-layered samples. The thicknesses of TiO_2 layers were fixed at 15 nm. Three different thicknesses of SiO_2 layers were taken: 160 nm, 180 nm and 200 nm. The resulting solar transmission and visible reflectance for each sample is also shown

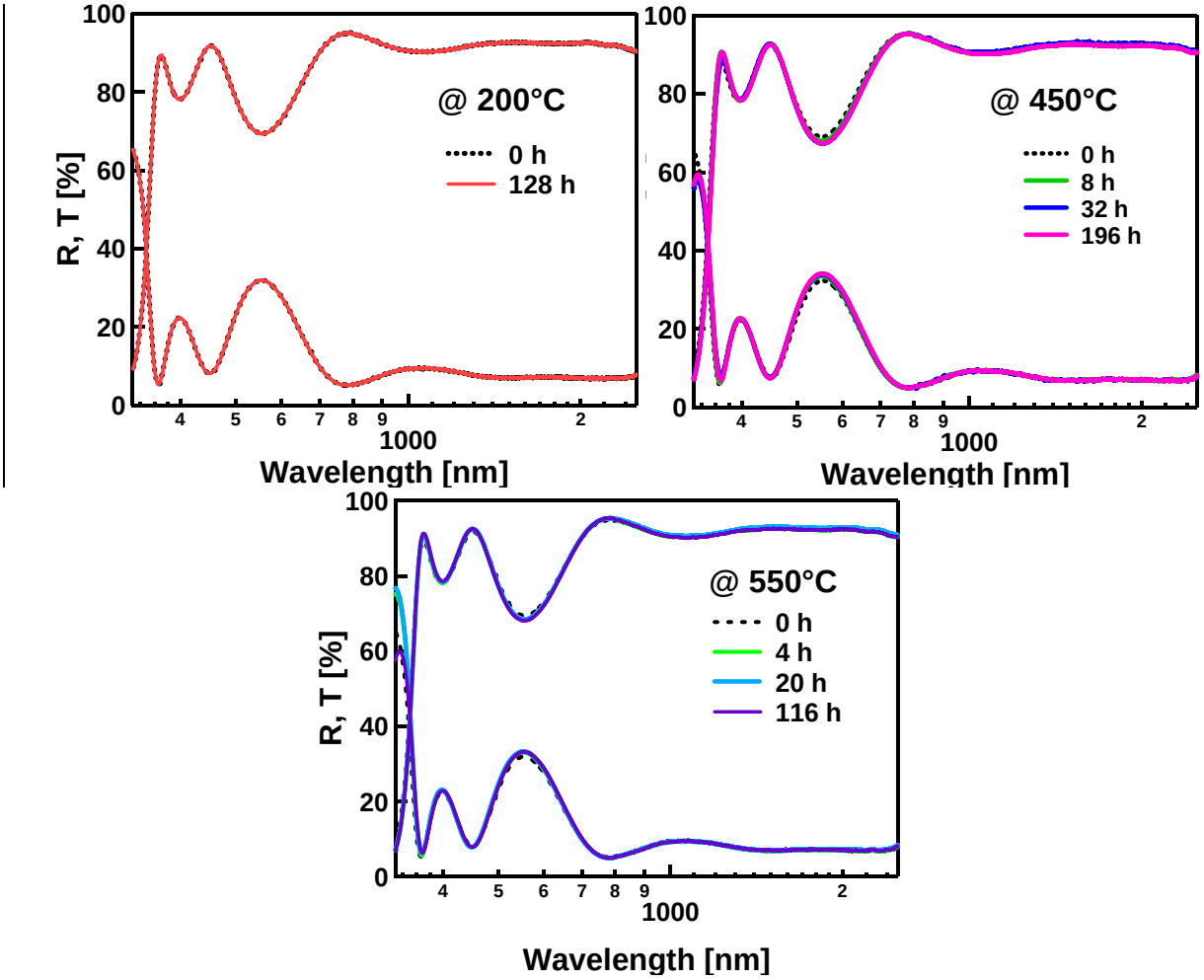

Figure 23: Total hemispherical reflectivity and transmission after an ageing test of 5 layered sample $TiO_2/SiO_2/TiO_2/SiO_2/TiO_2$//Si on glass in air at high temperature 200°C for 128 h (a) and at 450°C (b) for 8, 32 and 196 h and at 550°C for 4, 20 and 116h

Ageing tests were performed under different temperatures ranging from 200°C up to 550°C in a Joule effect oven. The samples were exposed to a constant temperature under air. Directly after the heating period, the sample was taken out of the oven. The total hemispherical reflectivity and transmission were monitored before and after undergoing an annealing at specific temperatures and for different durations.

Figure 23 displays the total hemispherical reflectivity and transmission of TiO_2–SiO_2 multilayer film with five layers on glass heated at 200°C, 450°C and 550°C for different ageing times. At different ageing temperatures, no change of the optical properties was observed even for a long heating time. The oscillations of the T_{sol}, R_{sol} and R_{vis} values did not exceed 6% of the initial values after ageing tests. The ageing properties of the 5 layered TiO_2–SiO_2 films show a good resistance and lifetime stability at elevated temperature in atmospheric air.

Samples	Temp/duration	R_{sol} (%)	T_{sol} (%)	R_{vis} (%)
Sample 1	as deposited	14.2	85.6	28.2
	200°C / 128 h	14.2	85.6	28.2
Sample 2	as deposited	14.3	85.7	28.6
	450°C / 8 h	14.5	85.5	29.7
	450°C / 32 h	14.6	85.4	29.9
	450°C / 196 h	14.7	85.2	30.1
Sample 3	as deposited	14.2	85.6	28.2
	550°C / 4 h	14.6	85.4	29.3
	550°C / 20 h	14.6	85.6	29.4
	550°C / 116 h	14.6	85.4	29.4

Table 2: Solar reflectivity, solar transmission and visible reflectance of three identical 5 layered samples $TiO_2/SiO_2/TiO_2/SiO_2/TiO_2$//Si after the ageing test at different temperatures and annealing time

2.8 Conclusion

In this part, coloured glass to cover solar collectors was obtained by alternative deposition of dielectric layers with high and low refractive indices. The deposition rate was controlled by in-situ laser reflectometry and confirmed by ex-situ ellipsometry for simple systems with one layers. The optical properties of the titanium oxide and

silicon oxide were determined. A Cauchy dispersion model is adequate for extracting the refractive and extinction index in the case of sputtering deposition.

The colour coordinates using the three-dimensional *Lab*space, blue, blue-green and green-yellow colours were calculated for a layered system. The reflected colour and the solar transmission depend on the thickness and the number of the alternative dielectric layers.

In conclusion, we have succeeded in showing that a sputtered multilayer coating can fulfill the requirements:

- quasi-zero absorption
- coloured reflectivity peak in the visible
- acceptable solar transmission

More effort has to be directed to optimize the thickness of individual layers and the number of layers for thermal solar collectors to get higher solar transmission results, a reflected light accommodated in a narrower band and an appropriate colour for architectural integration in building.

REFERENCES

[1] D. Bhattacharyya, N.K. Sahoo, S. Thakur, N.C. Das, Vacuum 60 (2001) 419
[2] H. Selhofer and R. Müller, Thin Solid Films 351 (1999) 180
[3] C. Garapon, J. Mugnier, G. Panczer, B. Jacquier, C. Champeaux, P. Marchet and A. Catherinot, Appl. Surf. Science 96-98 (1996) 836
[4] M.F. Ouellette, R.V. Lang, K.L. Yan, R.W. Bertram, R.S. Owies and D. Vincent, J. Vac. Sci. Technol. A. 9 (1991) 1188
[5] C. Rickers and M. Vergöhl, Thin Solid Films, 442 (2003) 145
[6] F. Hamelmann, G. Haindl, J. Schmalhorst, A. Aschentrup, E. Majkova, U. leineberg, U. Heinzmann, A. Klipp, P. Jutzi, A. Anopchenko, M. Jergel, S. Luby, Thin Solid Films, 358 (2000) 90
[7] X. Wang, H. Sumoto, Y. Someno, T. Hirai, Appl. Phys. Lett. 72 (1998) 3264.
[8] J. Szczyrbowski, G. Brauer, G. Teschner, A. Zmelty, Journal of Non Crystalline Solids. 218 (1997) 25
[9] M. Alvisi, L. Mirenghi, L. Tapfer, A. Rizzo, M.C. Ferrara, S. Scaglione, L. Vasanelli, Applied Surface Science, 157(1-2) (2000) 52
[10] L. Martinu, D. Poitras, Journal of Vacuum Science & Technology A Vacuum, Surfaces, and Films, 18 (2000) 2619
[11] J. Boudaden, R. S-C. Ho, P. Oelhafen, A. Schüler, C. Roecker and J. - L. Scartezzini, Solar Energy Materials and Solar Cells, 84 (2004) 225
[12] A. Schüler, C. Roecker, J. - L. Scartezzini, J. Boudaden and P. Oelhafen, Solar Energy Materials and Solar Cells, 84 (2004) 241
[13] B. Gallas, A. Brunet-Bruneau, S. Fisson, G. Vuye and J. Rivory, J. Appl. Phys., 9 (2002) 1922
[14] L. Soriano, G. G. Fuentes, C. Quiros, J.F. Trigo, J.M. Sanz, P.R. Bressler, and A.R. Gonzalez-Elipe, Langmuir, 16 (2000) 7066
[15] G. Lassaletta, A. Fernandez, J.P. Espinos and A.R. Gonzalez-Elipe, J. Phys. Chem., 99 (1995) 1484
[16] A. Barranco, F. Yubero, J.A. Mejias, J.P. Espinos, and A.R. Gonzalez-Elipe, Surface Science, 482-485 (2001) 680

[17] D.A. Shirley, Phys. Rev. B., 5 (1972) 4709
[18] J.J. Yeh and I. Lindau, Atomic Data and Nuclear Data Tables 32 (1985) 1
[19] R. Hesse, T. Chassé, R. Szargan , Unifit 2002 - universal analysis software for photoelectron spectra, Anal. Bioanal. Chem. 375 (2003) 856
[20] J.A. Mejias, V.M. Jimenz, G. Lassaletta, A. Fernandez and A.R. Gonzalez-Elipe, J. Phys. Chem., 100 (1996) 16255
[21] M.-A. Nicolet, P.H. Giauque, Microelectronic Engineering, 55 (2001) 357
[22] P.H. Giauque, H.B. Cherry, M.-A. Nicolet, Thin Solid Films, 394 (2001) 136
[23] A. Brunet-Bruneau, S. Fisson, B. Gallas, G. Vuye and J. Rivory, Proc. SPIE 3738 (1999) 188
[24] M.M. Gomeza, N. Beermannb, J. Lua, E. Olssona, A. Hagfeldtb, G.A. Niklassonb, C.G. Granqvista, Solar Energy Mater. Solar Cells 76 (2003) 37
[25] Z.D.X. Guangzhong and L. Wi, Vacuum 42 (1991) 1087
[26] C. Martinet, V. Paillard, A. Gagnaire and J. Joseph, J. Non-Cryst. Solids 216 (1997) 77
[27] H. Köstlin, G. Frank, H. Auding and G. Hebbinghaus, J. Non-Cryst. Solids 218 (1997) 347
[28] W. Que, W. Sun, Y. Zhou, Y.L. Lam, Y.C. Chan and C.H. Kam, Thin Solid Films 359 (2000) 177
[29] R.J. Hill, J. Non-Cryst. Solids 218 (1997) 54
[30] M. Vergöhl, N. Malkomes, T. Staedler, T. Matthée and U. Richter, Thin Solid Films 351 (1999) 42
[31] D. Mardare and G.I. Rusu, Mater. Lett. 56 (2002) 210
[32] N.S. Gluck, H. Sankur, J. Heuer, J. DeNatale and W.J. Gunning, J. Appl. Phys. 69 (1999) 3037
[33] A. Tabata, N. Matsuno, Y. Suzuoki and T. Mizutani, Thin Solid Films 289 (1996) 84
[34] W. Wong, H. Masumoto, Y. Someno, L. Chen and T. Hirai, J. Vac. Sci. Technol. B. 18 (2000) 933
[35] E.D. Palik, Handbook of Optical Constants of Solids, (Orlando, 1985)
[36] H. Poelman, D. Poelman, D. Depla, H. Tomaszewski, L. Fiermans, R. De Gryse, Surf. Sci. 482-485 (2001) 940

Chapter III is divided into two sections. The first one deals with in-situ initial-stage growth of sputtered silicon oxide on an aluminium oxide substrate (SiO_2/Al_2O_3) and sputtered aluminium oxide on a silicon dioxide substrate (Al_2O_3/SiO_2). The second one concentrates on the optical properties of formed Al_2O_3/SiO_2 multilayers on silicon or glass as well as ageing tests.

1 SiO_2/Al_2O_3 and Al_2O_3/SiO_2 interfaces

1.1 Introduction

An increasing interest in studying the oxide–oxide interface has been noticed in recent years. To understand the specificity of these interfaces, several studies were carried out recently by growing thin oxide on the surface of another oxide. X-ray photoelectron spectroscopy and other electron spectroscopies were used to study the electronic interactions appearing at different oxide/oxide interfaces.

The development of high dielectric constant (high-k) materials is one of the crucial subjects for future complementary metal-oxide-semiconductor (CMOS) devices [1, 2]. Alumina (Al_2O_3) has emerged as one of the promising substitutes for the SiO_2 dielectric layer currently used in semiconductor manufacturing processes, due to its higher dielectric constant. The electrical properties of CMOS devices depend not only on the properties of the Al_2O_3 film but also on the formed interface between Al_2O_3 and the Si substrate. The aim of several studies was to focus on the interfacial formation between Al_2O_3 and SiO_2. O. Renault et al [3] studied the interface characteristics when depositing ultra-thin Al_2O_3 layers on Si or SiO_2 surfaces. They found that the interfacial region depends on the Al_2O_3 thickness: the thicker the layer the larger the interface region. The interface zone was significantly reduced for Al_2O_3/SiO_2 compared to Al_2O_3/Si. R. Reiche et al [4] showed that in very thin films of Al_2O_3 evaporated on the surface of SiO_2, the coordination state of Al_{2p} ions varies from tetrahedral to octahedral up to a coverage of about 1 monolayer. The same observation was established for alumino-silicate compounds, where Al holds these two types of coordination. A. Barranco et al [5] focused on the study of the electronic interaction at SiO_2/Al_2O_3 interface by X-ray photoemission spectroscopy. The

observed shift in the Si2p binding energy was attributed to the electronic/chemical interactions with the support for the first monolayers of SiO_2. The oxygen ions acting as a bridge between the two oxide phases are less polarisable than those of bulk SiO_2, which agrees with the polarisabilities of oxide ions in alumino-silicate compounds.

1.2 Experimental details

SiO_2 and Al_2O_3 oxides were deposited at room temperature by magnetron sputtering in a high vacuum deposition chamber. The two magnetrons used were capped by aluminium and silicon targets. One was capped by aluminium target and driven by bipolar-pulsed power (50 kHz at 95 W); the other was driven by medium frequency RF power (100 W at 13.5 kHz). The sputtering was operated in the presence of a mixture of argon-oxygen gas at a pressure of 3×10^{-3} mbar. The argon-oxgen mass flow ratio was fixed at 35:5 for silicon oxide and 37:3 for aluminium oxide.

The distances for the aluminium target—substrate and silicon target—substrate were 8 and 5 cm, respectively. Stable plasma conditions were achieved after operating the magnetron source for some minutes. Laser reflectrometry was employed to estimate the growth rate of the sputtered oxides by depositing a thick oxide film of several hundreds of nm on a silicon substrate (40x40 mm^2). The deposition rates of Al_2O_3 and SiO_2 were 6.0 nm/min and 7.4 nm/min, respectively, and were confirmed by ex-situ spectroscopic ellipsometry.

To study the early stages of aluminium oxide growth on silicon oxide (Al_2O_3/SiO_2) or vice versa (SiO_2/Al_2O_3), first a 6-nm thick layer of the first substrate oxide was sputtered on a monocrystalline (100)-oriented silicon substrate. The native silicon oxide layer was etched using a Kaufman ion gun source from the silicon substrate.

Thereafter, the deposition of the second overlayer oxide was made in several steps. After each deposition step, the surface characterisation was studied by monitoring the Al2p, Si2p and O1s core-level peaks

1.3 XPS results

1.3.1 SiO_2 on Al_2O_3

Figure 1 shows the evolution Si2p core level as a function of SiO_2 thickness deposited on Al_2O_3 substrate.

The Si2p binding energy shifts to a higher value by increasing the SiO_2 coverage on Al_2O_3. For SiO_2 thickness less than 5 nm, a large shift of 0.8 eV is observed for the Si2p binding energy. For a higher coverage, the final binding energy of the Si2p is 103.9 eV.

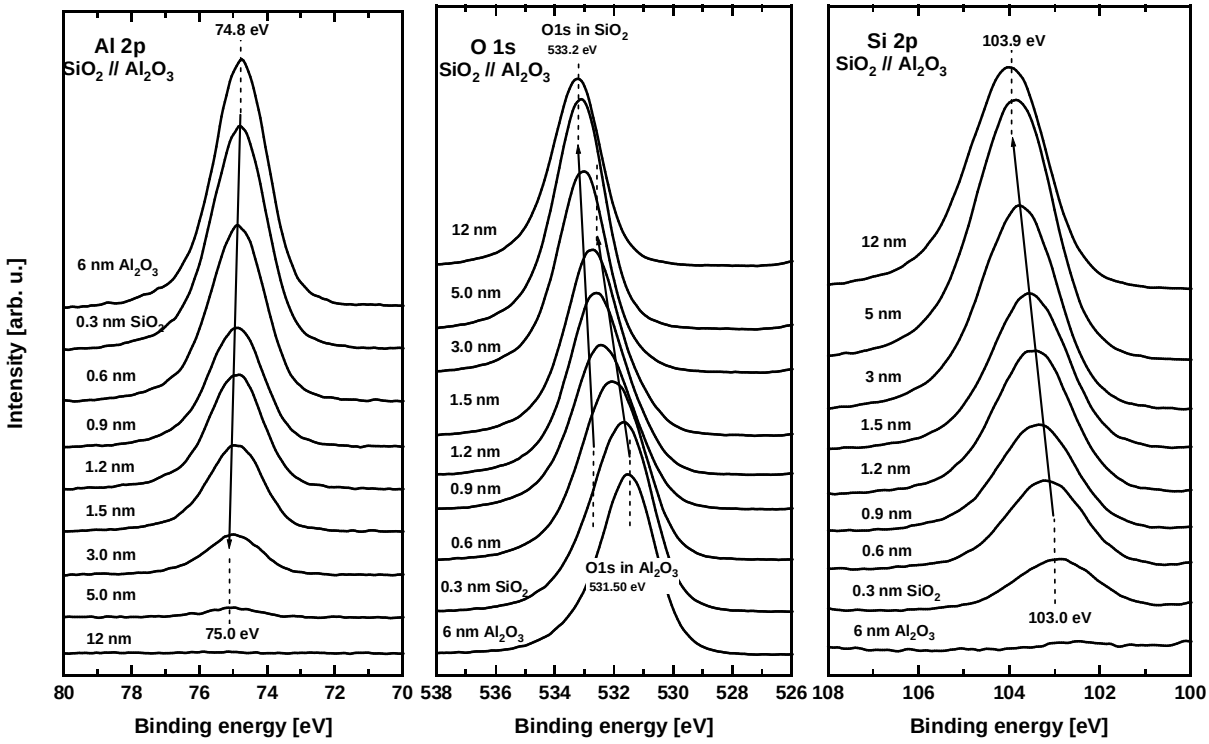

Figure 1: Al2p, O1s and Si2p core-level spectra obtained by sputtering a small coverage of Al_2O_3 on a 6-nm thick SiO_2 to study the interface formed when SiO_2 is deposited on Al_2O_3

O1s peak related to the 6-nm thickness of sputtered Al_2O_3 on Si (100) is situated at 531.5 eV. A continuous sputtering of SiO_2 on Al_2O_3 leads to the appearance of a second O1s peak at 533.2 eV, which is associated with the SiO_2 phase. To determine the position of O1s peaks originating from the Al_2O_3 and SiO_2 phases, a fit procedure using two peaks was done to separate the contribution of each material. Figure 2 shows an example of a fitted curve for 0.9-nm thickness of SiO_2 on Al_2O_3. Each O1s peak was fitted with two Gaussian-Lorentzian curves after subtracting a

Shirley background. The intensity of the O1s peak related to the SiO_2 enlarged as the SiO_2 content increased. It appeared first at a binding energy of 532.8 eV and shifted then to higher binding energies by about 0.4 eV. The O1s peak related to the Al_2O_3 phase diminished in intensity and shifted to the higher binding energy of 532.3 eV. It disappeared completely for SiO_2 thickness larger than 5 nm.

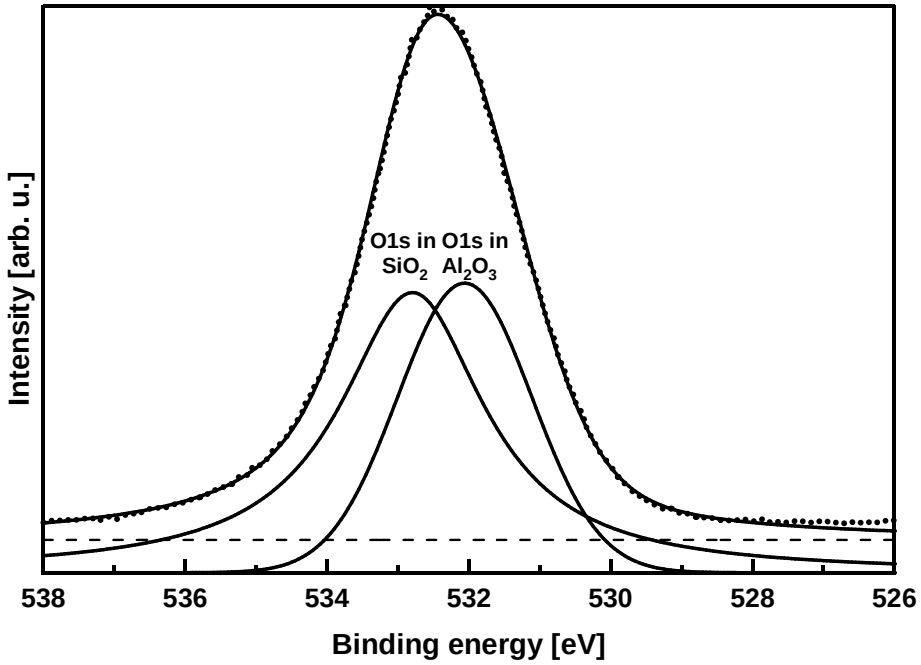

Figure 2: Deconvolution example of O1s spectra obtained after sputtering 0.9 nm of SiO_2 on a 6-nm thick Al_2O_3 substrate. The O1s peak was deconvoluted into two peaks, one related to SiO_2 and the second one related to Al_2O_3 after subtracting a Shirley background (dashed line)

1.3.2 Al_2O_3 on SiO_2

Spectra of the Si2p, O1s and Al2p from the SiO_2 substrate layer and the increasing amount of the deposited Al_2O_3 layer are represented in Figure 3.

The Si2p peak position shows a small shift to the lower binding energies from 103.4 eV to 103.2 eV as the amount of the deposited Al_2O_3 increases and reaches 2 nm thick.

The Al2p binding energy value slightly shifts from 75.3 eV to 75 eV as the deposited amount of Al_2O_3 is thicker than 2 nm.

To determine the position of O1s peaks originating from the Al_2O_3 and SiO_2 oxides, a fit procedure using two peaks is done to separate the contribution of each material. We have used two curves for the deconvolution of O1s peak, each convoluted with Gaussian-Lorentzian after subtracting the Shirley background. Increasing the Al_2O_3

content decreases the intensity of the O1s peak related to SiO_2. It shifts from 532.7 to 533.8 eV. It disappears completely for a deposited Al_2O_3 thicker than 5 nm. The peak related to Al_2O_3 gains in intensity and shifts to the lower binding energies. It appears first at a binding energy of 532.3 eV and shifts to lower binding energies by about 0.6 eV.

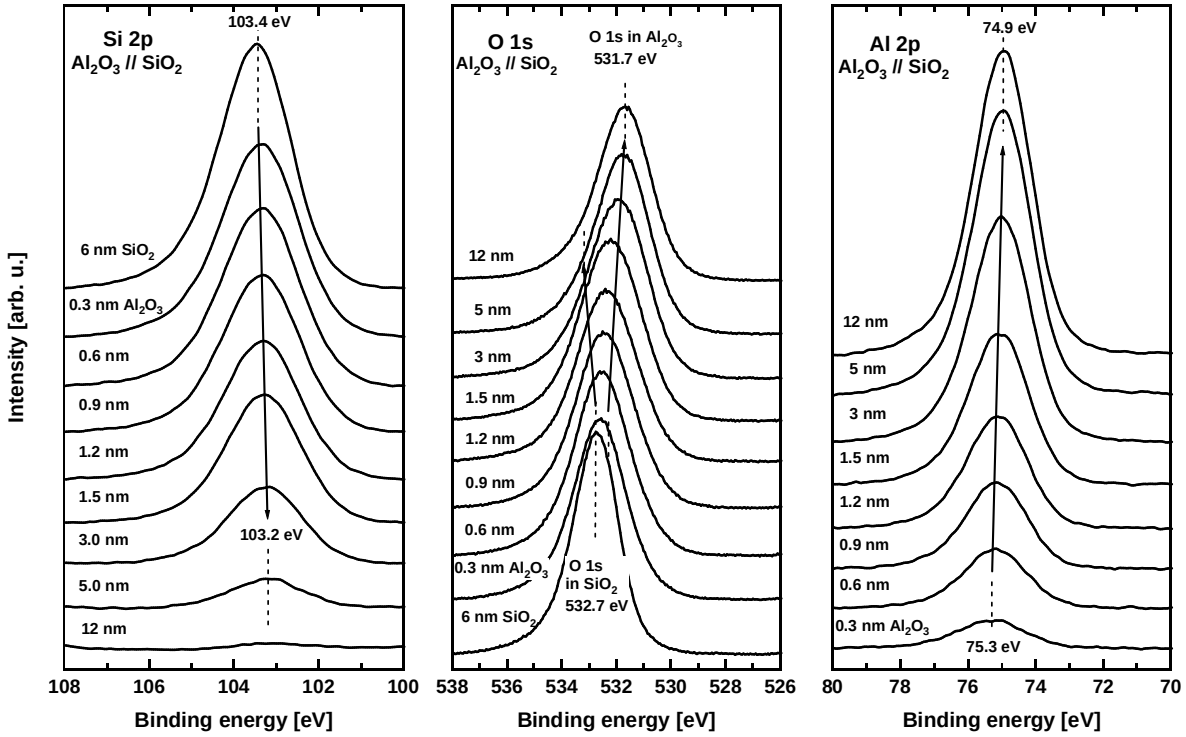

Figure 3: Si2p, O1s and Al2p core-level spectra obtained by sputtering a small coverage of SiO_2 on a 6-nm thick Al_2O_3 to study the interface formed when SiO_2 is deposited on Al_2O_3

1.4 Discussion

For SiO_2 sputtered on Al_2O_3, we found that the binding energy of the Si2p increases with coverage. The evolution of the electronic parameters of SiO_2 on Al_2O_3 follows the reverse trend to that found for TiO_2 [6] and Al_2O_3 oxides deposited on the SiO_2. Barranco et al [5] presented the same observation while studying the electronic interaction at the SiO_2/Al_2O_3 interface.

XPS measurement on the oxides suffers from charging phenomena, which is considered as an experimental obstacle to an accurate determination of binding energies of chemical elements in oxides. The results of XPS support the fact that the binding energy positions of the chemical elements are not sufficient to ascertain the

presence or the absence of an interfacial zone between the SiO_2 and the Al_2O_3. To overcome this problem, we defined the difference of the binding energies for two elements of the same layer.

Figure 4 shows two graphs representing the binding energy difference between the O1s peak related to the oxide in the overlayer and the Si2p or Al2p peaks as a function of deposited oxide thickness.

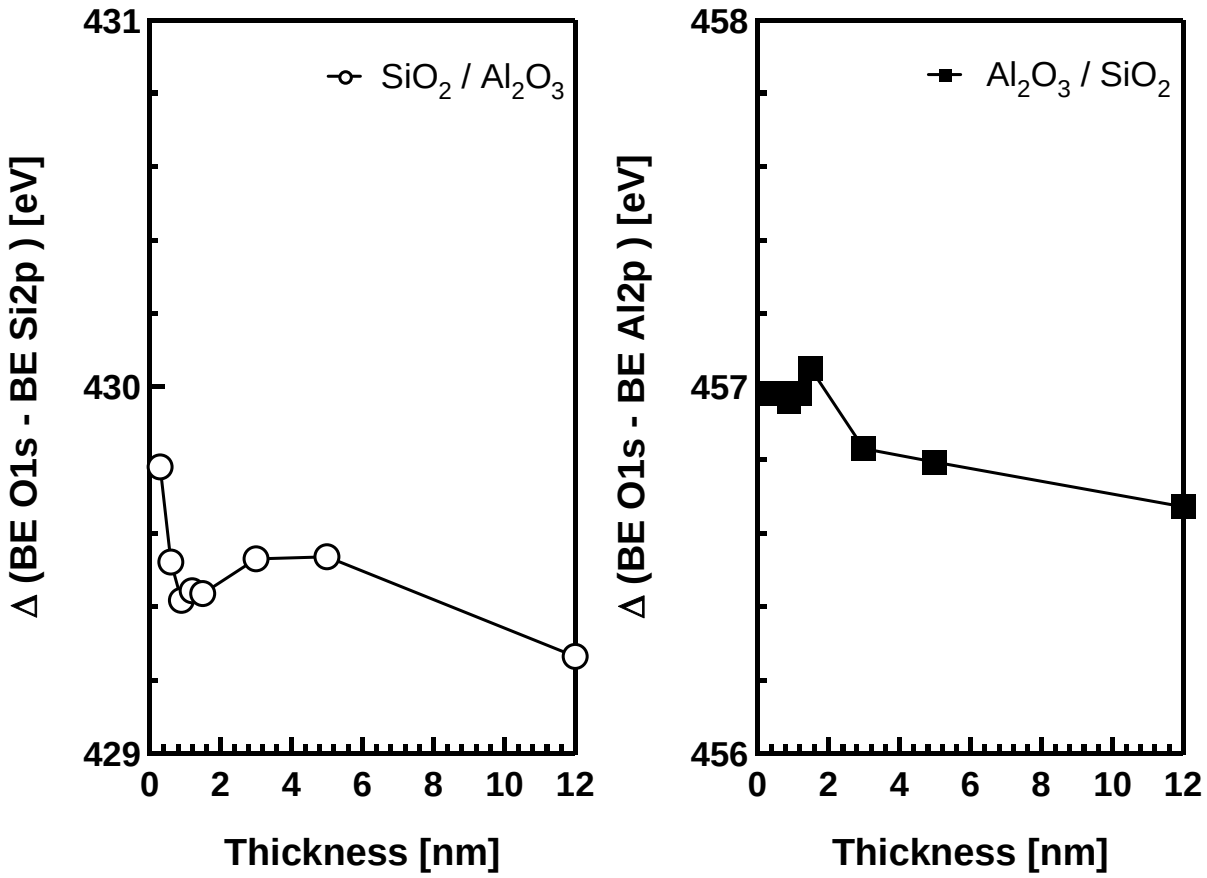

Figure 4: Distance Δ(BE O1s(SiO_2) – BE Si2p) between O1s related to SiO_2 and Si2p core levels for SiO_2 on Al_2O_3 interface (left graph). Distance Δ(BE O1s(Al_2O_3) – BE Al2p) between O1s related to Al_2O_3 and Al2p core levels for Al_2O_3 on SiO_2 interface (right graph)

On the left graph of Figure 4, the distance Δ(BE O1s(SiO_2) – BE Si2p) or $\Delta_{O,Si}$ between O1s related to SiO_2 and Si2p core levels decreases from 429.8 eV for the first 1.5 nm and becomes constant at 429.6 eV while depositing SiO_2 on Al_2O_3.

On the right graph of Figure 4, the distance Δ(BE O1s(Al_2O_3) – BE Al2p) or $\Delta_{O,\ Al}$ between the BE of the O1s related to Al_2O_3 and Al2p core levels shows a decrease from 457.0 eV to 456.8 eV for 2-nm thick of Al_2O_3 sputtered on SiO_2. The obtained value of the $\Delta_{O,Al}$ parameter is close to that found by Renault et al [3] for a 1-nm Al_2O_3

on SiO_2 and to that of the bulk alumino-silicates [7], which are 457.3 eV and 457.2 eV, respectively. An accurate estimation of the thickness of the formed reactive interface between Al_2O_3 and SiO_2 oxides is difficult. The interface width of SiO_2/Al_2O_3 and Al_2O_3/SiO_2 appears to be less than 1 nm.

Figure 5 shows the binding energy difference between Al2p and Si2p denoted Δ(BE Al2p – BE Si2p) or $\Delta_{Al,Si}$ coming from two different layers for both interfaces Al_2O_3/SiO_2 and SiO_2/Al_2O_3. It varies from 28.0 eV to 28.2 eV for both systems Al_2O_3/SiO_2 and SiO_2/Al_2O_3 after only some monolayers (0.5 nm) of deposited oxide. The variation is probably due to the presence of an interfacial reaction between the two oxides in this region, as found by Renault et al [3] and Ch. Gründling et al [8]. They found that the $\Delta_{Al,Si}$ parameter ranged between 27.7-27.9 eV for the bulk alumino-silicates, which is close to 28.0-28.2 eV calculated in our work at the Al_2O_3 and SiO_2 interfaces. Thus, at the interfacial region mixed aluminium and silicon oxides are present.

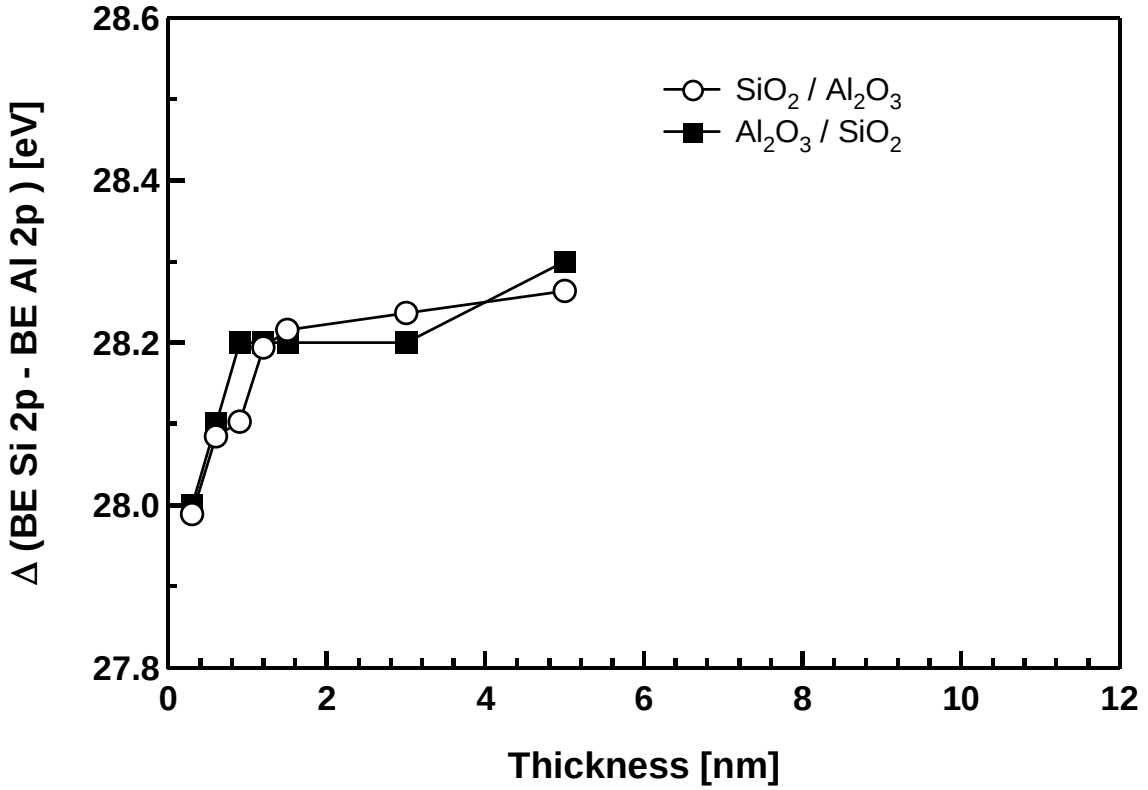

Figure 5: Distance Δ(BE Si2p – BE Al2p) between Si2p in SiO_2 and Al2p in Al_2O_3 core levels for both SiO_2 on Al_2O_3 and SiO_2 on Al_2O_3 interfaces

For Al_2O_3 or SiO_2 thicker than 1 nm, the $\Delta_{Al,Si}$ parameter stays constant at 28.2 eV. These observations could be explained by the similar static dielectric constants of Al_2O_3 and SiO_2, which are 2.89 and 2.25, respectively.

1.5 Conclusion

We studied the deposition of SiO_2 on Al_2O_3 and Al_2O_3 on SiO_2 using photoelectron spectroscopy by measuring Al2p, O1s and Si2p core levels. To exclude a charging effect on the surface of the studied oxides, we calculated a distance between the binding energies of the elements in the same overlayer. We also determined $\Delta_{Al,Si}$, which is defined as a binding energy difference between Al2p and Si2p core levels rising from the two oxide layers.

It seems that an interfacial reaction took place between the two oxides on contact. The formed interface is due to the presence of alumina-silicates compound between oxides layers. Our experimental results gave a rough estimation of the formed interfacial zone between Al_2O_3 and SiO_2 oxides, which is less than 1 nm for the system SiO_2 on Al_2O_3 but difficult to estimate for the system Al_2O_3 on SiO_2 (figure 5). Mixed aluminium and silicon oxides are present at the interfacial region less than 1 nm (figure 6).

2 Al_2O_3 – SiO_2 multilayers for coloured glazed solar collectors

2.1 Introduction

Transparent oxide films are widely employed as antireflection or high reflection coatings [9, 10], band-pass filters [11] and narrow-band-filters [12] in various optical and electronic devices. The performances of these devices are based on interference effects obtained by alternating layers of high and low refractive indices.

Nowadays different deposition methods exist to produce dielectric oxide films. Thin film evaporation underwent rapid development and became a standard method for optical coatings [13]. Afterwards, alternative methods such as chemical vapor deposition [14], dip coating [15], sol gel method [16] and reactive sputtering [17] have been extensively studied. The latter allows large area coatings and thicknesses uniformity combined with high growth rate deposition [18].

In this section, we report an experimental study for the preparation of optical coatings based on Al_2O_3 – SiO_2 multilayer dielectric films realised by reactive magnetron sputtering by depositing alternating layers of two materials. During the experimental realisation, some important requirements must be fulfilled. For example, the deposition technique must allow good control and reproducibility of the optical properties of any individual thin film combined with a high deposition rate. Moreover, the interface between two layers should be as smooth as possible. To meet the above conditions, SiO_2 and Al_2O_3 are considered suitable materials to cover solar thermal collectors [19].

2.2 Experimental details

Silicon oxide and aluminium oxide thin films were prepared by reactive magnetron sputtering in a high vacuum deposition chamber using an Ar/O_2 gas mixture. The mass flow ratio was set to 35:5 for silicon oxide and to 37:3 for aluminium oxide. The magnetrons were driven by bipolar-pulsed power for the Al target (50 kHz at 150 W) and by medium frequency RF power (13.5 kHz at 100 W) for the Si target. During the thin film deposition carried out at room temperature, the grounded substrates faced the target at a distance between 5 and 8 centimetres. A working pressure of around 3 x 10^{-3} mbar was adjusted by throttling the pumping system. SiO_2 and Al_2O_3 films were deposited on glass AF45 and monocrystalline silicon (40x40 mm^2 with its native oxide) substrates for the optical characterisation.

For the in-situ photoelectron spectroscopy characterisation, the Si 2p, Al 2p and O1s core levels were recorded in the case of SiO_2 and Al_2O_3 to determine the atomic concentration ratios and consequently the chemical composition for each layer. In our deposition conditions, the XPS measurements showed a reproducible stoichiometry for the SiO_2 and Al_2O_3 films.

Silicon wafers were used as substrates for in-situ real-time laser reflectometry and ex-situ ellipsometry, while glass substrates were used for ex-situ spectrophotometry. The optical reflectivity of a laser beam is measured continuously during the film deposition to determine the deposition rate and the optical constants n and k at one wavelength. The optical constants n and k and the thicknesses of any individual thin films inside a multilayer coating were determined by ellipsometry. The ellipsometer

(SENTECH SE 850) was performed in the range 300-850 nm with variable angle of incidence ranging between 40° and 70° by steps of 10°. The total hemispherical reflectivity and transmission curves in the UV, VIS and NIR were performed on a Varian Cary 5 spectrophotometer.

2.3 Optical characterisation

2.3.1 Laser Reflectometry

The reflectivity data at 532 nm were monitored as a function of time during the deposition of SiO_2 and Al_2O_3 films on silicon substrates using the laser light polarization parallel to the incidence plane.

The experimental obtained curves, shown in Figure 6, show oscillations with constant amplitude, which is an indicator of the film's transparency. We consider that the extinction coefficient k at 532 nm is zero. The numerical fitting of the experimental data using the reflectivity formula of a one layer on substrate model allow the determination of the optical constant of the deposited film. Thus, the laser reflectometry provides important information about the growth rate (24.7 nm/min for Al_2O_3 and 7.6 nm/min for SiO_2) and the refractive index n (1.59 for Al_2O_3 and 1.47 for SiO_2) at only one wavelength, 532 nm.

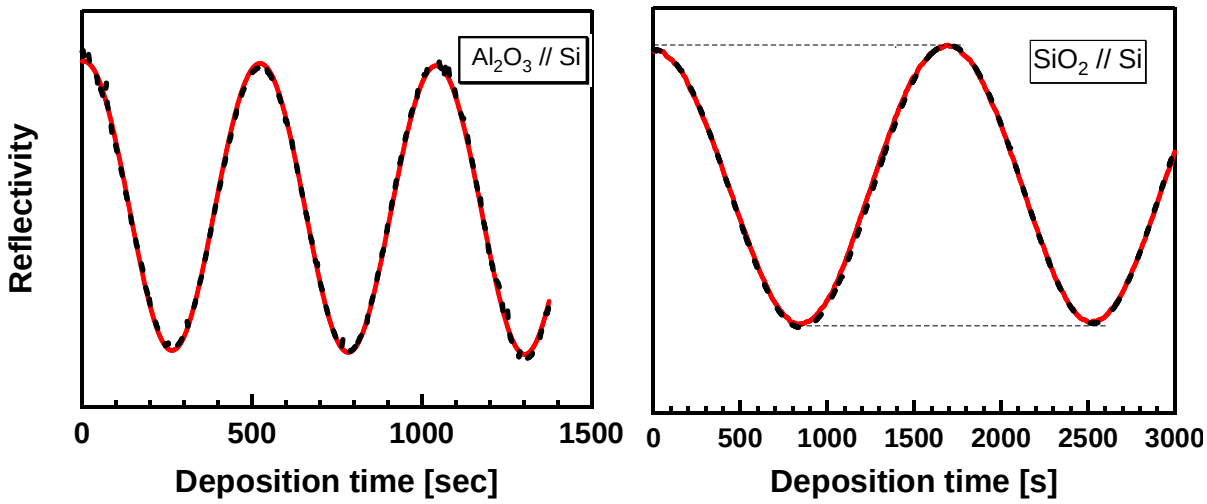

Figure 6: Real-time laser reflectometry of sputtered Al_2O_3 and SiO_2 on Si. The solid curves correspond to the experimental data, the dashed ones to the fit curves

2.3.2 Ellipsometry

2.3.2.1 Single layers on silicon substrate: Al_2O_3 on Si and SiO_2 on Si

The ellipsometric data were monitored in the range 300-850 nm for different incident angles between 40° and 70°. A systematic study of the optical properties of individual dielectric layer for SiO_2 and Al_2O_3 by ellipsometer was done. To extract the optical parameters, the films were modelled as single uniform homogeneous dielectric layers on a semi-infinite silicon substrate. A native silicon dioxide interlayer was included in the model. Surface roughness was neglected. The ψ and Δ spectra were fitted with a widely used Cauchy dispersion formula for SiO_2 and Al_2O_3 layers.

Figures 7 and 8 show the measured ellipsometric data ψ and Δ for a deposited single layer of Al_2O_3 and SiO_2 on silicon substrates and the best theoretical fits using the Cauchy dispersion model. The measurements and fits were plotted by solid and dashed lines.

A good agreement between the fit and the experimental data was obtained for SiO_2 and Al_2O_3.The best Cauchy parameters for the fit in the wavelength range 300-850 nm are (n_0 = 1.57, n_1 = 77.3 nm^2, n_2 = -22.9 nm^4, k_0= k_1= k_2=*0*) for the Al_2O_3 individual layer and (n_0 = 1.46, n_1 = 25.3 nm^2, n_2 = 17.5 nm^4, k_0= k_1= k_2=*0*) for the SiO_2 individual layer. The fit results confirm that no absorption occurs in the films. The sputtering rates were 25 nm/min for Al_2O_3 and 7.6 nm/min for SiO_2.

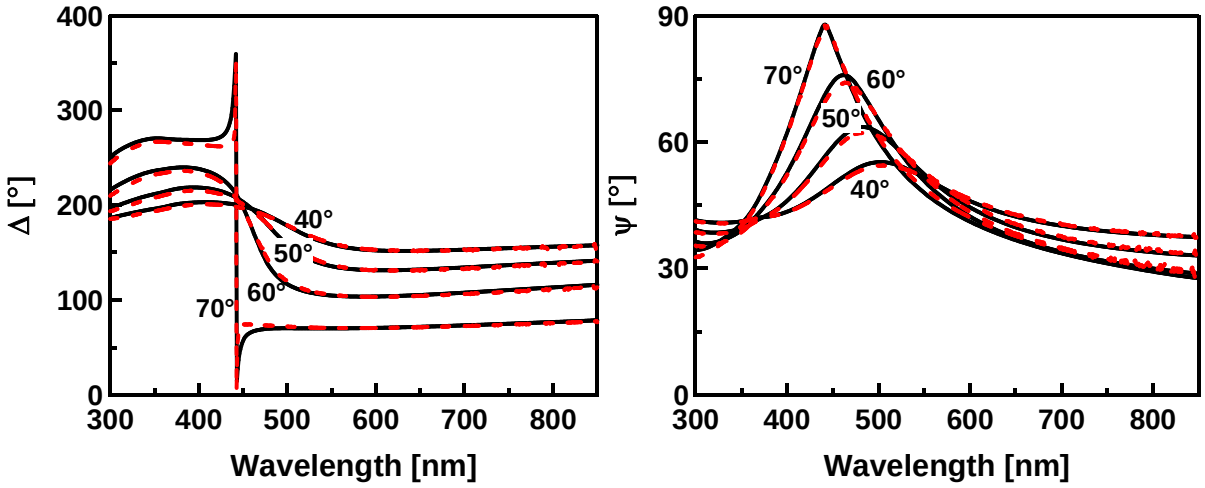

Figure 7: Ellipsometric spectrum of sputtered Al_2O_3 on silicon substrate

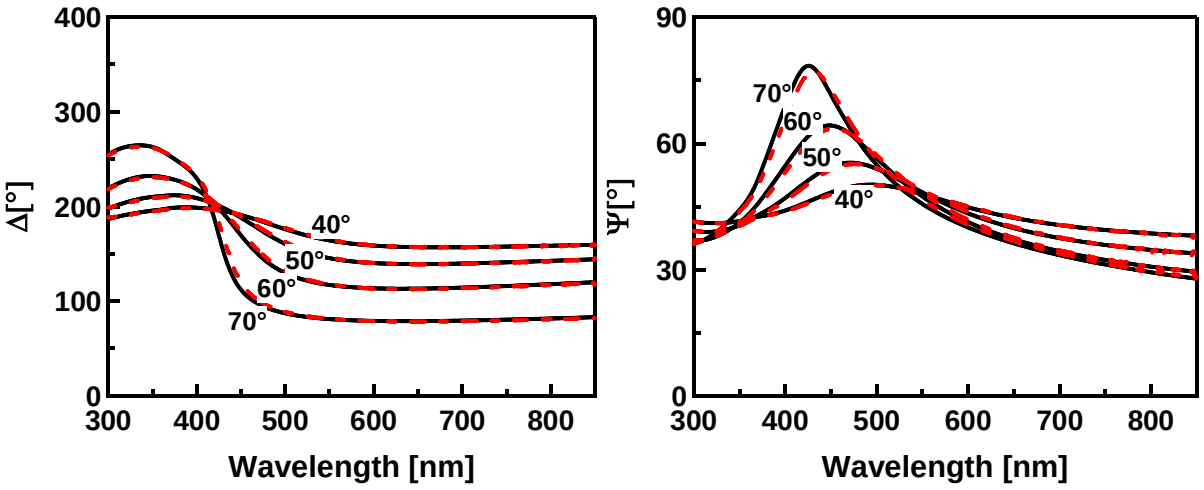

Figure 8: Ellipsometric spectrum of sputtered SiO_2on silicon substrate

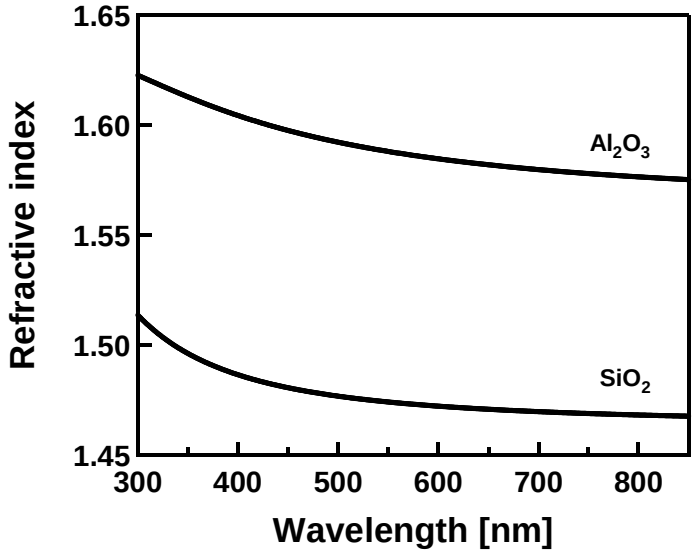

Figure 9: Refractive index dispersion for the sputtered Al_2O_3 and SiO_2 films

Figure 9 shows the refractive index *n* curve in the wavelength range 300-850 nm for SiO_2 and Al_2O_3. It should be noted here, by comparing the sputtering rate deduced by laser reflectometry and ellipsometry that the thicknesses of the SiO_2 dielectric layers determined by the ellipsometry are in a good agreement within 5% of the determined one by the laser reflectometry. However, the thickness discrepancy for the Al_2O_3 film is 10%.

2.4 Multilayered films

2.4.1 Multilayers on silicon substrate

After studying the optical properties of individual dielectric layers of Al_2O_3 and SiO_2, we are interested now in the more complex system of two, three, four and five layers. For individual layers Al_2O_3 and SiO_2, the experimental ellipsometric data was fitted with a widely used Cauchy model.

For the multilayered sample, the optical properties were taken from that of individual layers. Thickness was the only parameter that was allowed to fluctuate during the fit procedure. Figures 10–14 show the measured ellipsometric functions ψ and Δ□□ and □the corresponding fits□ for multilayered films with respectively 2, 3, 4 or 5 alternating layers.

We observed a good agreement between the experimental (dashed line) and the fitted (solid line) data. Table 1 summaries the expected layer thicknesses calculated from the sputtering velocities deduced by laser reflectometry and ellipsometry for individual layers and the thickness for the best fit of the multilayered samples with 2, 3, 4 and 5 layers.

The good agreement between the data indicates reproducible sputter deposition and optical properties of the dielectric materials as well as the validity of our model with abrupt interfaces between the SiO_2 and Al_2O_3 layers.

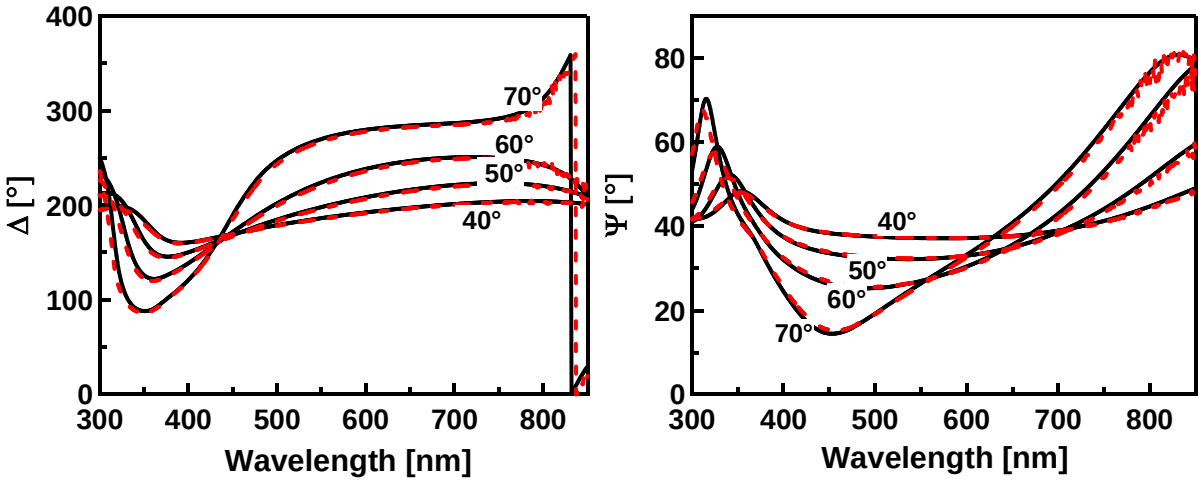

Figure 10: Ellipsometric spectrum of sputtered 2-layered sample SiO_2/Al_2O_3 //Si

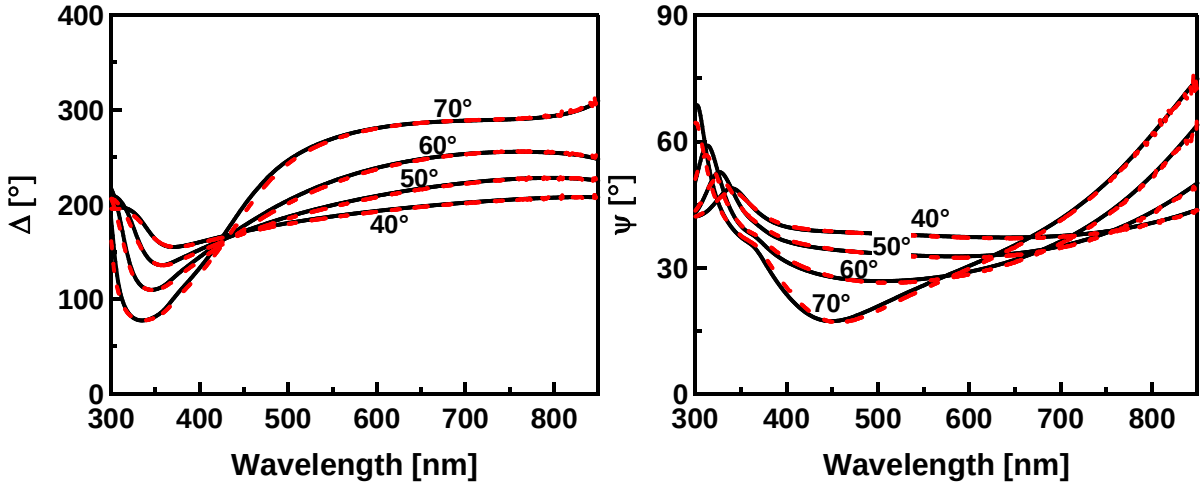

Figure 11: Ellipsometric spectrum of sputtered 2-layered sample Al_2O_3/SiO_2//Si

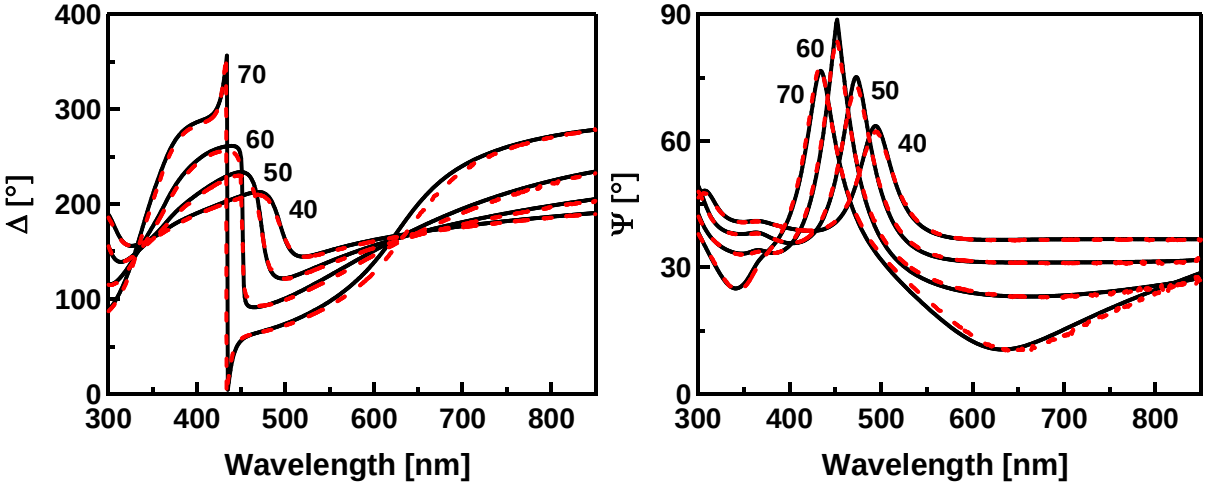

Figure 12: Ellipsometric spectrum of sputtered of 3-layered sample $Al_2O_3/SiO_2/Al_2O_3$//Si

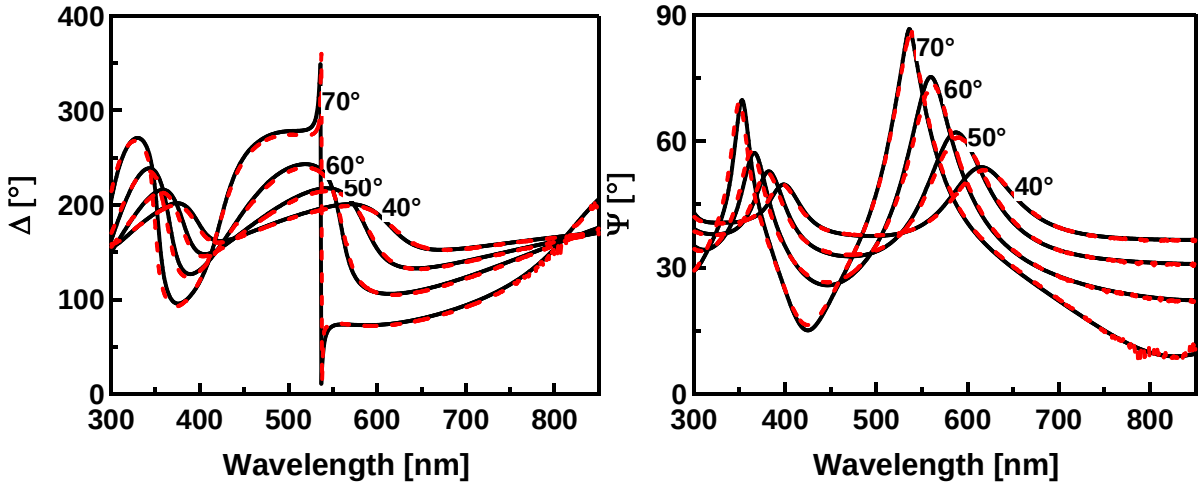

Figure 13: Ellipsometric spectrum of sputtered of 4-layered sample $SiO_2/Al_2O_3/SiO_2/Al_2O_3$//Si

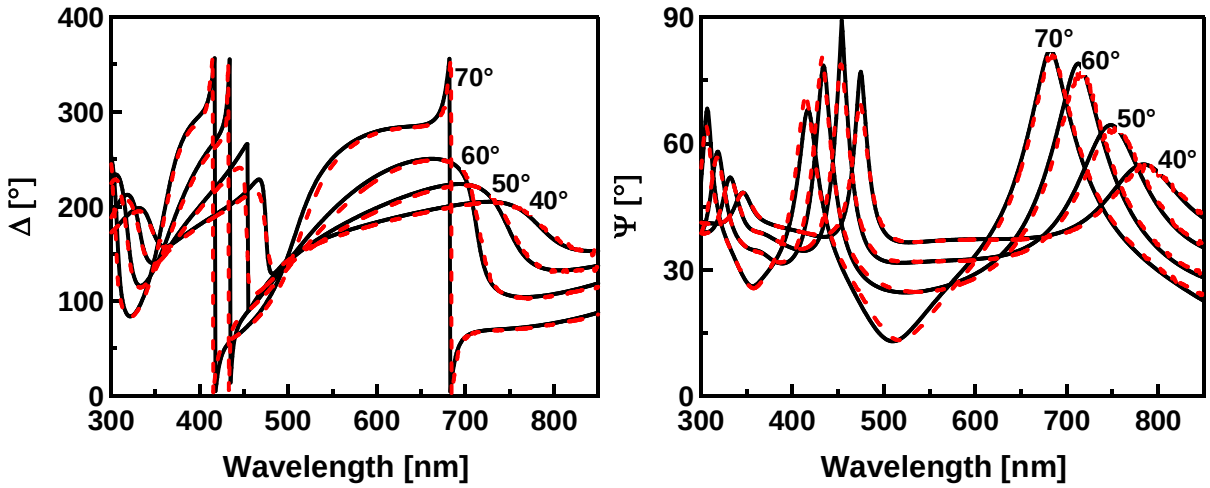

Figure 14: Ellipsometric spectrum of sputtered of 5-layered sample $Al_2O_3/SiO_2/Al_2O_3/SiO_2/Al_2O_3$//Si

		Thickness by Laser Reflectometry [nm]	Thickness by Ellipsometry [nm]	Thickness by the best fit [nm]
1L	**Al_2O_3//Si**	91	83	83
1L	**SiO_2//Si**	90	91	91
2L	**Al_2O_3/SiO_2//Si**	-	-	83/91
	SiO_2/Al_2O_3//Si	-	-	94/83
3L	**$Al_2O_3/SiO_2/Al_2O_3$//Si**	-	-	83/94/83
4L	**$SiO_2/Al_2O_3/SiO_2/Al_2O_3$ //Si**	-	-	81/91/81/92
5L	**$Al_2O_3/SiO_2/Al_2O_3/SiO_2$ /Al_2O_3//Si**	-	-	81/87/81/89/81

Table 1: Deduced thickness by ellipsometry and laser reflectometry (LR) for individual layer and the multilayered samples (shown on figures 10-14)

2.4.2 Simulation of the solar transmission and visible reflectance

Numerical simulations allow optimizing the optical properties of multilayers as a function of the thickness and the number of alternated layers.

The effects of the number of layers and the thicknesses on the optical properties of the Al_2O_3 – SiO_2 multilayered systems were simulated by the software *Advanced Fit*. The obtained refractive index curves, in the rage 300-850 nm, for individual layers Al_2O_3 and SiO_2 by ellipsometry spectroscopy were used (see paragraph 1.3.2.1) to realise the simulation.

The solar transmission T_{sol} as well as the visible reflectance R_{vis} are represented in cartographic form on Figures 15-17 for 5-, 9- and 11-layered samples on glass.

These two parameters are considered to be the most important parameters for the Al_2O_3/SiO_2 multilayers for the coloured glazed collector application. The thicknesses of Al_2O_3 and SiO_2 layers was varied from 50 to 100 nm and from 10 to 150 nm, respectively. It is of great interest to know the thickness and the number of layers which are needed to achieve, at the same time, a higher solar transmission (higher than 88%) and a higher visible reflectance (greater than 12%).

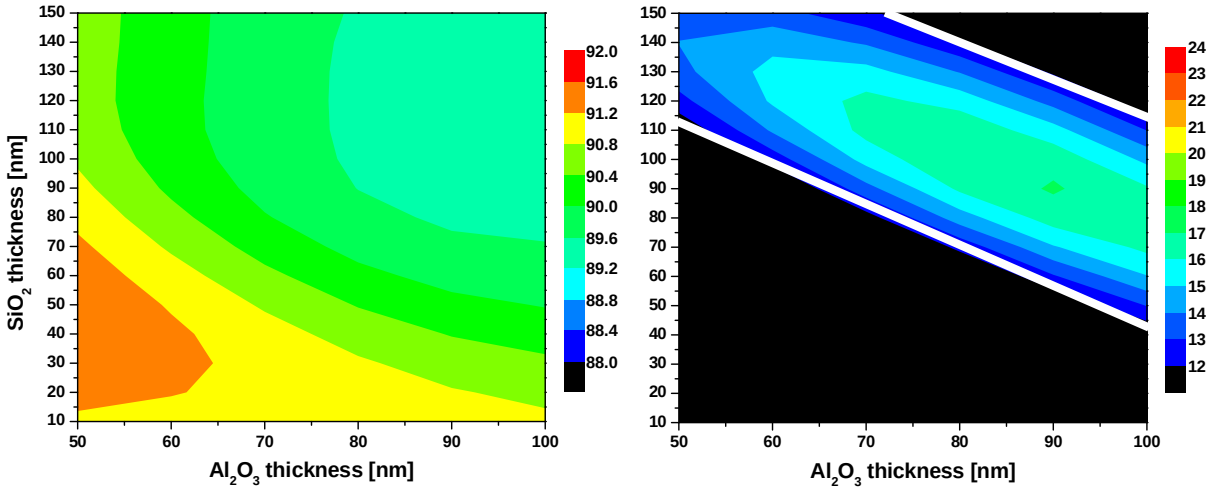

Figure 15: Solar transmission (left) and visible reflectance (right) cartographies for 5-layered system depending on the thicknesses of Al_2O_3 and SiO_2

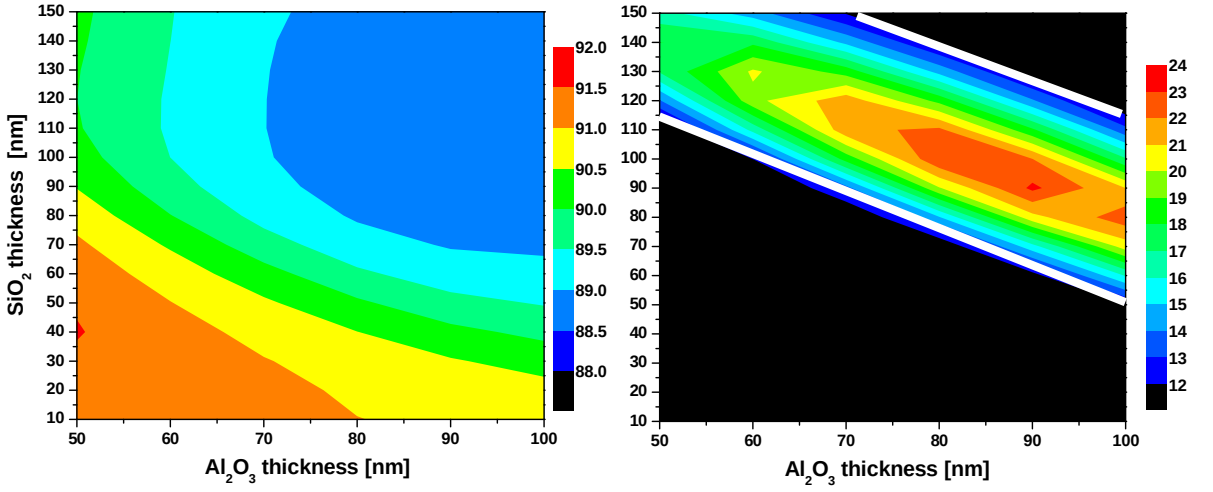

Figure 16: Solar transmission (left) and visible reflectance (right) cartographies for 9-layered system depending on the thicknesses of Al_2O_3 and SiO_2

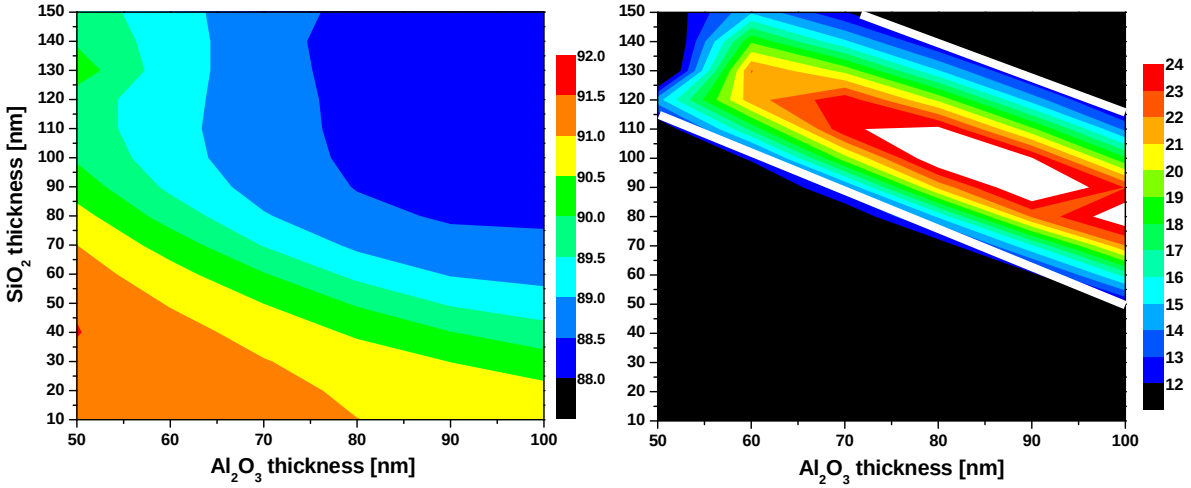

Figure 17: Solar transmission (left) and visible reflectance (right) cartographies for 11-layered system depending on the thicknesses of Al_2O_3 and SiO_2

The area with the best compromise: a higher solar transmission (more than 88%) and the sufficiently higher visible reflectance (more than 12%) is limited by white lines on the cartographies. Adding the number of layers has a positive effect on the visible reflectance value, which is increased, but the solar transmission is decreased. These results show the possibility of achieving our purpose for 5-, 9- and 11-layered samples. For example, the SiO_2 thickness should be in the range 90-150 or 70-130 nm, when the Al_2O_3 thickness is fixed at 70 or 100 nm, respectively

2.4.3 Experimental realisation on glass

We have realised a couple of multilayered Al_2O_3 – SiO_2 samples on glass based on the simulation results. Figure 18 shows the theoretical and measured reflectivity curves of four different samples. The thicknesses of Al_2O_3 and SiO_2 layers alternatively deposited on glass were 83 nm and 95 nm, respectively.

The theoretical curves were calculated using the experimental optical constants determined by spectroscopic ellipsometry on single-layer samples. In our model, we suppose homogenous layers and sharp interfaces.

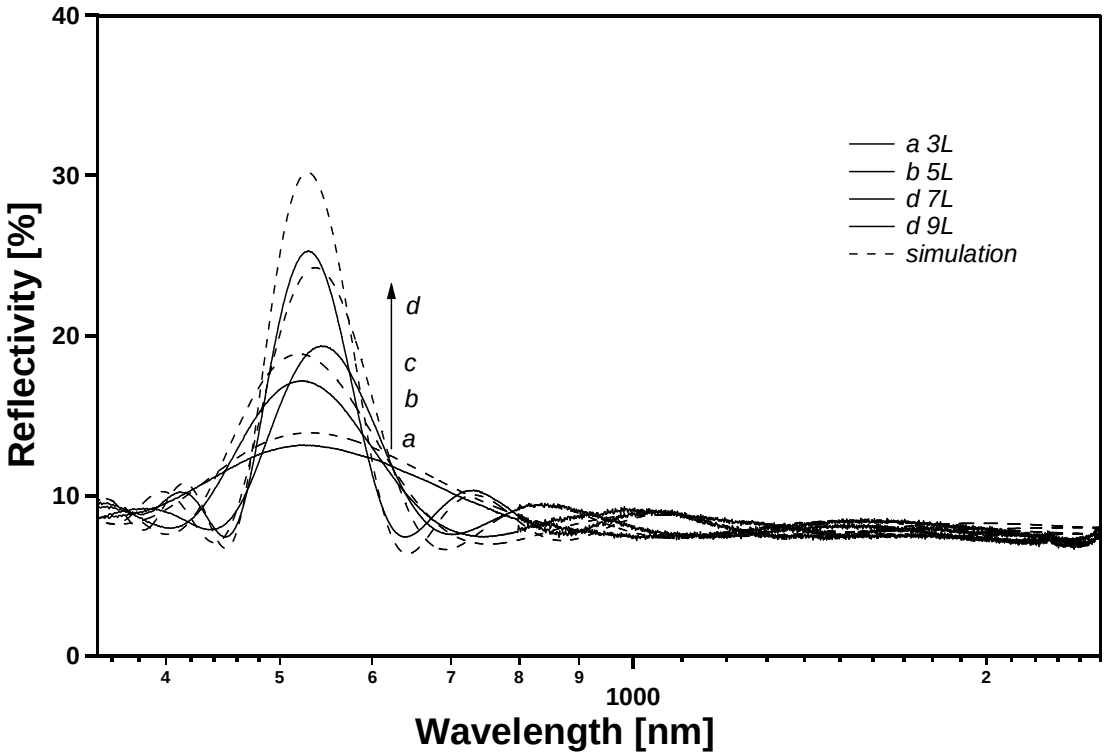

Figure 18: Measured total reflectivity of Al_2O_3 – SiO_2 multilayers (solid lines) combined with the theoretical one (dotted lines), the parameters are summarised in Table 2

		T_{sol} [%]		R_{sol} [%]		R_{vis} [%]	
		exp	Theo	exp	theo	exp	theo
3L	*a*	90.5	90	9.8	10	12.7	13.5
5L	*b*	89.9	89.6	10.2	10.4	15.2	16.4
7L	*c*	89.7	89.1	10.3	10.9	16.7	20
9L	*d*	89.4	88.8	10.7	11.2	18.7	21.7

Table 2: Measured parameters (thicknesses, solar transmission and reflectivity, visible reflectance and merit factor) of Al_2O_3 – SiO_2 multilayers combined with the same theoretical parameters

The reflectivity peak position is situated in the visible range. The height increases when the number of layers is increased. This evolution shows that the reflectivity peak position, its maximum value and its FWHM depend on the number of layers. The position of the reflectivity peak is relatively constant and its maximum value increases by increasing the number of alternating layers. The disagreement between the experimental and calculated values for the 7- and 9-layered samples can probably be explained by an eventual change of the deposition conditions during the long deposition time, resulting in a deviation between the expected and the real thicknesses of the different layers. An arc generation was visually observed on the

target surface and in plasma discharge during a long time sputtering of Al_2O_3. We believe this violent phenomena has a direct influence on the layer thickness and generates defects on the surface of the film [20].

Table 2 shows the solar transmission, the solar reflectivity and the visible reflectance in the case of the Al_2O_3 – SiO_2 multilayers. The solar transmission is slightly decreasing by increasing layer number, but stays at a high level superior to 89%, which is slightly lower than the solar transmission of uncoated glass (92%). As mentioned above, this is due to the small refractive index difference between SiO_2 and Al_2O_3. The visible reflectance increases.

The solar transmission of the four samples is higher than 88%, combined with a pronounced visible reflectance (higher than 12%). Different colours of the reflected light from glazed samples can be obtained by changing the reflectivity peak position— in other words, the Al_2O_3 and SiO_2 thicknesses.

2.5 Ageing test

The thermal stability of 5-layered samples $Al_2O_3/SiO_2/Al_2O_3/SiO_2/Al_2O_3$ on glass was studied by annealing at high temperature in a joule effect oven. Three identical samples underwent heating at three different temperatures—350, 450 and 550°C—and for different annealing time—from 1 h to 116 h. Figure 19 shows the reflectivity and transmission of the samples before and after ageing. All the samples present a change of the spectral reflectivity and transmission due to annealing at high temperature. The peak height situated at 560 nm decreases for an annealed sample. The optical properties of the samples are summarized in Table 3. An important degradation of the visible reflectance is observed whatever the annealing temperature. However, the solar transmission is slightly improved. An annealing at 350°C for only 1 hour is able to decrease the visible reflectance by 10% and to increase the solar transmission by 0.7%. The decay magnitude of the visible reflectance and the gain in solar transmission depend on the annealing temperature as well the annealing time at a chosen temperature. They reach 26.4% and 1.9% for an annealing of 116h at 550°C. It is clear from the ageing test that optical properties changes seem to take place for the 5-layered Al_2O_3/SiO_2 samples at elevated

temperature in atmospheric air, which have a dramatic effect on the visible reflectance and a marginal benefic effect on the solar transmission.

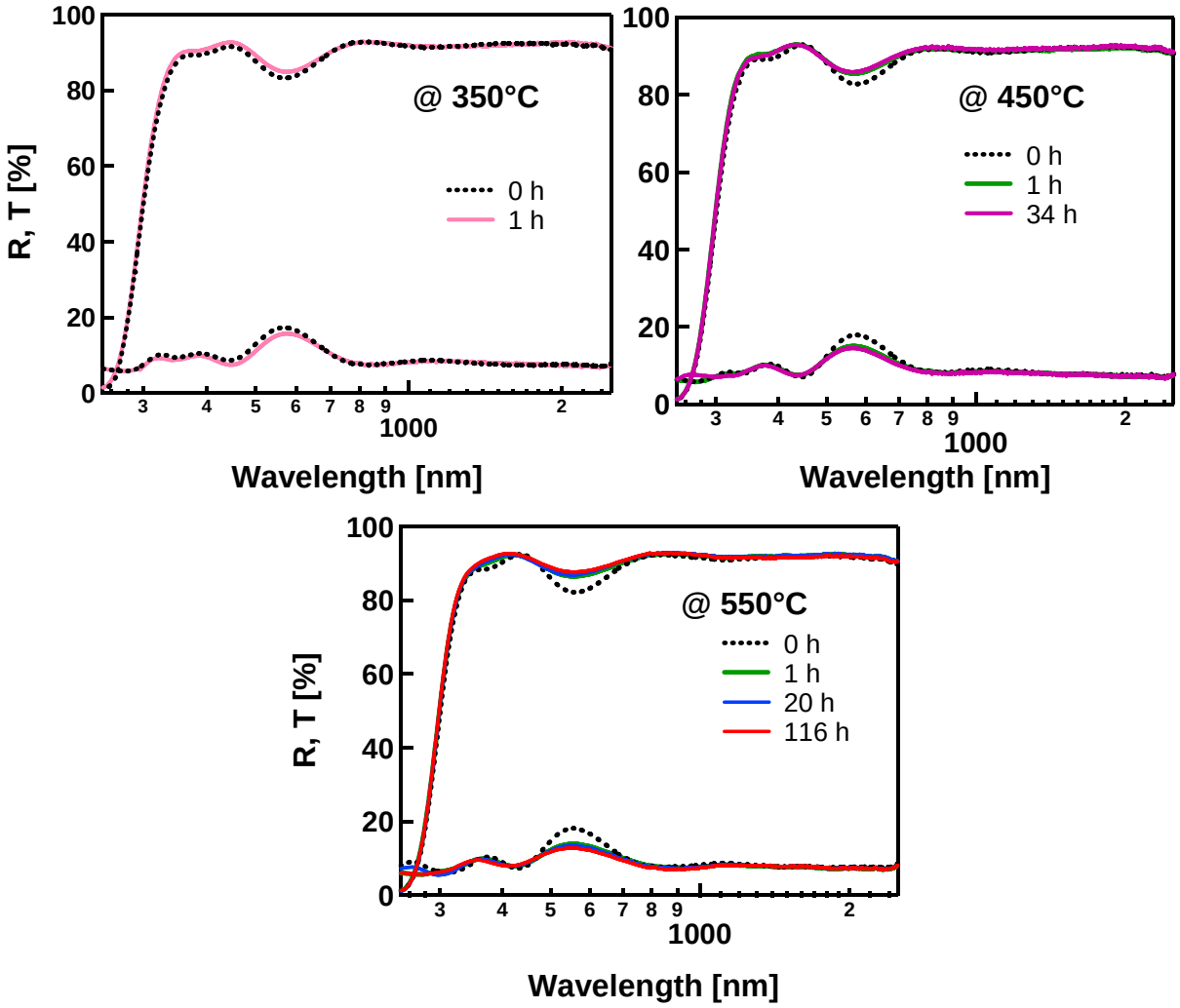

Figure 19: Total hemispherical reflectivity and transmission after an ageing test of Al_2O_3 – SiO_2 multilayers on glass in air at 35°C for 1 h (a) and at 450°C (b) for 1 h and 34 h and at 550°C for 1, 20 and 116 h

samples	Temp/duration	T_{sol} [%]	R_{vis} [%]	Decrease in R_{vis} [%]	Increase in T_{sol} [%]
Sample 1	as deposited	89.7	15.8	0	0
	350°C/1h	90.3	14.2	10	0.7
Sample 2	as deposited	89.4	16.1	0	0
	450°C/1h	90.1	13.9	13.5	0.8
	450°C/34h	90.4	13.5	16.1	1.1
Sample 3	as deposited	89.2	16.7	0	0
	550°C/1h	90.5	13.3	20.8	1.5
	550°C/20h	90.7	12.9	22.9	1.7
	550°C/116h	90.9	12.3	26.4	1.9

Table 3: Solar transmission and visible reflectance of three identical samples after the ageing test at different temperatures and annealing time

2.6 Conclusion

Coloured glass to cover solar collectors has been obtained by alternative deposition of dielectric layers with high and low refractive indices. The deposition rate has been controlled by in-situ laser reflectometry and confirmed by ex-situ ellipsometry for complex systems with several layers. The optical properties of individual oxides of silicon and aluminium have been determined. A Cauchy dispersion model is adequate for extracting the refractive and extinction index in the case of reactive magnetron sputtering deposition.

The reflectivity and the solar transmission of multilayered samples on glass depend on the thicknesses and the number of the alternated dielectric layers. The fabricated multilayers fulfilled the fixed requirements: nearly zero absorption, reflectivity peak in the visible, solar transmission above 88% combined with an acceptable visible reflectance, whereby the solar transmission of uncoated glass is 92%.

The ageing test on 5-layered Al_2O_3 – SiO_2 samples showed a strong degradation in their visible reflectance, which is increased by increasing the annealing temperature and time. However, the solar transmission is increased by 2%. This increase in the solar transmission can be considered a positive effect of the ageing test for our application for architectural integration in buildings; nevertheless, one has to make sure of conserving an acceptable visible reflectance.

REFERENCES

[1] G. D. Wilk G.D. Wilk, R. M. Wallace, J. M. Anthony, J. Appl. Phys. 89 (2001) 5243
[2] K. Kimoto, Y. Matsui, T. Nabatame, T. Yasuda, T. Mizoguchi, I. Tanaka, A. Torium, Appl. Phys. Lett. 83 (2003) 4306
[3] O. Renault, L.G. Gosset, D. Rouchon, A. Ermolieff, J. Vac. Sci. Technol. A. 20 (2002) 1867
[4] R. Reiche, F. Yubero, J.P. Espinos, A.R. Gonzalze-Elipe, Surf. Sci. 457 (2000) 199
[5] A. Barranco, F. Yubero, J.A. Mejias, J.P. Espinos, A.R. Gonzalez-Elipe, Surf. Science 482-485 (2001) 680
[6] See chapter 2
[7] A.R. Gonzalez-Elipe, J.P. Espinos, G. Munuera, J. Sanz, J.M. serratosa, J. Phys. Chem. Solids, 36 (1988) 3471
[8] Ch. Gründling, J.A. Lercher, D.W. Goodman, Surf. Sci. 318 (1994) 97
[9] D. Bhattacharyya, N.K. Sahoo, S. Thakur, N.C. Das, Vacuum 60 (2001) 419
[10] H. Selhofer and R. Müller, Thin Solid Films 351 (1999) 180
[11] C. Garapon, J. Mugnier, G. Panczer, B. Jacquier, C. Champeaux, P. Marchet and A. Catherinot, Appl. Surf. Science 96-98 (1996) 836
[12] M.F. Ouellette, R.V. Lang, K.L. Yan, R.W. Bertram, R.S. Owies and D. Vincent, J. Vac. Sci. Technol. A. 9 (1991) 1188
[13] Z.D.X. Guangzhong and L. Wi, Vacuum 42 (1991) 1087

[14] C. Martinet, V. Paillard, A. Gagnaire and J. Joseph, J. Non-Cryst. Solids 216 (1997) 77
[15] H. Köstlin, G. Frank, H. Auding and G. Hebbinghaus, J. Non-Cryst. Solids 218 (1997) 347
[16] W. Que, W. Sun, Y. Zhou, Y.L. Lam, Y.C. Chan and C.H. Kam, Thin Solid Films 359 (2000) 177
[17] R.J. Hill, J. Non-Cryst. Solids 218 (1997) 54
[18] M. Vergöhl, N. Malkomes, T. Staedler, T. Matthée and U. Richter, Thin Solid Films 351 (1999) 42
[19] J. Boudaden, R. S.-C. Ho, P. Oelhafen, A. Schüler, C. Roecker and J.-L. Scartezzini, Solar Energy Mater. Solar Cells (2004) 225
[20] K. Koski, J. Hölsä, P. Juliet, Surf. Coatings thechnology 115 (1999) 163

1 TiO_2 – SiO_2 composite films for coloured glazed solar collectors

1.1 Introduction

For decades, the optical properties of composite oxides have attracted a great deal of interest. The preparation of homogeneous composites allows for the development of promising materials with different optical properties for new applications.

Titanium and silicon dioxides are the most frequently used materials in various optical devices, such as antireflection, high-reflection coatings and band-pass filters [1]. They are transparent in a large spectral band, and have a high (at λ = 550 nm n = 2.3 for amorphous TiO_2) [2, 3] and low (at λ = 550 nm n = 1.46) [2] refractive index and a quasi-zero absorption in the visible. Therefore, TiO_2 and SiO_2 are the most adequate optical materials in both discrete and mixed composite coatings. TiO_2-SiO_2 mixed oxides have received a lot of attention, due to several advantages, such as a specific elevated melting temperature, immiscibility, film homogeneity and avoidance of intermediate compounds or phase formations [4]. Several groups investigated the structural and the electrical properties of partially oxygenated TiSiOx compounds [5] as well the completely oxygenated phase of a Ti-Si-O system [6]. Beyers described the thermodynamics in refractory metal-silicon-oxygen systems via ternary phase diagram. An interesting feature for Ti-Si-O system is that their ternary diagram phase has a tie line connecting the two binary compounds TiO_2 and SiO_2, which are in equilibrium phases [7]. Incorporating one into the other increases the free energy of the crystalline phase.

Chen et al [8] and Brunet-Bruneau et al [9] reported the optical and structural properties of electron-beam coevaporated mixed oxides investigated by RBS, AFM, transmission and ellipsometry spectroscopies. Sankur et al [10] studied the crystallisation and Ti diffusivity in layered and codeposited TiO_2-SiO_2 thin films. They found out that the minimum temperature for the formation of anatase phase increases with increasing the silicon oxide content in the co-deposited film.

Using sol–gel techniques, Jiwei et al [11] and Que et al [12] prepared TiO_2-SiO_2 composite thin films for optical waveguides. The optical wave-guiding properties

increase by raising titanium oxide content in the mixed film and depend on the annealing temperature, which induces segregation effects and a heterogeneous distribution of the film. Stakheev et al [13] used XPS and XAES to determine the concentration of the mixed TiO_2-SiO_2 formed by a homogenous precipitation procedure. The obtained data revealed that for low TiO_2 concentration, the TiO_2-SiO_2 system exists as a homogeneous solid solution of TiO_2 in SiO_2 but for a low SiO_2 concentration, silicon forms a monolayer titanium-silicate coating on the TiO_2 particles. Schüler et al. realised a multilayered $SiO_2/Ti_{1-x}Si_xO_2$ coating on glasses by sol-gel dip-coating. The obtained solar transmission and visible reflectance are acceptable for the application in coloured glazed thermal solar collectors [14].

Concerning the deposited composite TiO_2-SiO_2 films by sputtering methods, Gluck et al [4] investigated their structural properties. Demiryont [15] demonstrated a continuous change in their optical properties depending on the concentration of each oxide in the prepared film. Wang et al [16] determined the optical properties of helicon plasma sputtered TiO_2-SiO_2 films at one discrete wavelength 633 nm. Previous studies showed that the desired refractive index can be conveniently achieved by adjusting the composition of the composite film by controlling the applied power on each used target during the sputtering process. Ouellette et al [17] made a homogeneous mixed coating for fabricating a narrow band filter widely used for protecting the instruments from damage by intense narrow band radiation. The literature study shows that the optical properties of composite oxide depend on the preparation conditions and methods. The determination and control of the optical properties is therefore an essential step for further device development.

In this section, we investigate the possibility to obtain intermediate refractive indexes by mixing different amounts of SiO_2 and TiO_2 to obtain a selective reflectivity in the visible by using stacks of two transparent mediums, the first one with a lower refractive index (SiO_2) and the second one with a higher index (mixed TiO_2 – SiO_2).

1.2 Experimental details

Composite TiO_2-SiO_2 dielectric films obtained by reactive sputtering were manufactured using a new homemade co-centric double ring magnetron. The double ring magnetron sputtering source consists of an inner target and an outer target. The

power applied to any of the targets can be chosen independently. This offers new possibilities to deposit mixed-oxide multilayer films with a separate feed of energy and a high flexibility for the process control. The water-cooled double ring magnetron capped by an outer titanium and an inner silicon target was driven by bipolar-pulsed power (50 kHz at 100 W or 250 W) for the Ti target and by medium frequency RF power (13.5 kHz at 10 to 100 W) for the Si target.

The experiments were performed in a vacuum system that consists of two interconnected chambers: high vacuum deposition chamber and ultrahigh vacuum XPS analysis chamber. The high vacuum deposition chamber, pumped down to a background pressure of 10^{-6} mbar, was used for the sputtering of dielectric coating films. (100) oriented crystalline silicon wafers were used as substrates, from which the native oxide layer had been etched using a Kaufman ion gun source. The thin film deposition took place at room temperature, at a fixed distance of 6 cm from the sample and at a working pressure around 5 x 10^{-3} mbar. High purity argon and oxygen were used as process gases and their mass flow ratio was set to 7:1. The double magnetron sources were always run for some minutes before starting the deposition on the chosen substrate to clean the targets and to achieve stable plasma conditions.

The ultrahigh vacuum XPS analysis chamber connected to the high vacuum deposition chamber insured a transfer between the two chambers without breaking the vacuum. The relative concentrations of titanium, silicon and oxygen were determined by integrating the Ti2p doublet, Si2p and O1s core lines after subtracting a Shirley background [18]. From the photoionization cross-sections given by [19], the atomic concentration at the film's surface was then calculated using UNIFIT [20].

The optical reflectivity of a laser beam was continuously measured in-situ in a high vacuum deposition chamber while sputtering a thick oxide film of several hundreds of nm. The films measured in-situ by laser reflectometry were also subjected to an ex-situ ellipsometry measurement performed by an SENTECH SE 850 ellipsometer in the range 350 - 850 nm. The total hemispherical reflectivity (diffuse and specular) at 7° angle of incidence and transmission at 0° angle of incidence measurements in the UV, VIS and NIR are performed on a Varian Cary 5 spectrophotometer.

TiO_2-SiO_2 composites with different SiO_2 and TiO_2 contents were cosputtered by keeping the power supply applied to the Ti target constant (at 250 W for a first series

and at 100 W for a second series of samples) and that applied to the Si target was varied from 10 to 100 W to obtain mixed oxides with different compositions.

For the multilayered films on glass, mixed oxide TiO_2-SiO_2 and SiO_2 layers were alternately sputtered, the mixed oxide layer with the higher refractive index being deposited on top of the substrate. The TiO_2- SiO_2 layer was obtained by applying 35 W or 45 W to the Si target and 100 W to the Ti target. The silicon oxide layer was sputtered using a standard magnetron capped by a silicon target and driven by medium frequency RF power (100 W at 13.5 kHz). The silicon oxide was deposited in the presence of an argon-oxygen gas mixture at a pressure of 5×10^{-3} mbar; the argon-oxygen partial pressure ratio was fixed at 7:1. The distance silicon target-substrate was 5 cm.

1.3 Results and discussion

1.3.1 XPS

Figure 1 shows the fractions $f_x = I_x/(I_{Si2p} + I_{Ti2p} + I_{O1s})$ of the detected elements in the mixed oxides by XPS as a function of the applied power to the Si target, $I_x = I_{Si2p}$, I_{Ti2p} or I_{O1s} being the intensities of the core levels Si2p, Ti2p doublet and O1s peaks, respectively. By increasing the power applied to the silicon target, the content of silicon in mixed films increases and that of titanium decreases for both values of the applied power to the titanium target (100 W or 250 W). For each fixed applied power to the Si target from 25 to 50W, increasing the applied power to the Ti target from 100 W to 250 W induces a decrease of the silicon concentration and an increase of the titanium concentration. The relative content of oxygen, however, remains quite constant (between 60 and 65%) over the entire range of the applied power to the Si target, whatever the applied power to Ti target (100 W or 250 W) was. It is quite close to 66%, independently of the applied power to the Ti target, as it is the case for a composite film being a mixture of SiO_2 and TiO_2 phases. Moreover, the XPS spectra do not indicate other phases related to the titanium or to the silicon besides TiO_2 and SiO_2 oxides. If we suppose that the mixed oxide film is composed exclusively of TiO_2 and SiO_2, than the SiO_2 fraction is given by $F = I_{Si2p}/(I_{Si2p} + I_{Ti2p})$. The fraction F is plotted on Figure 2 as a function of the power applied to the silicon target.

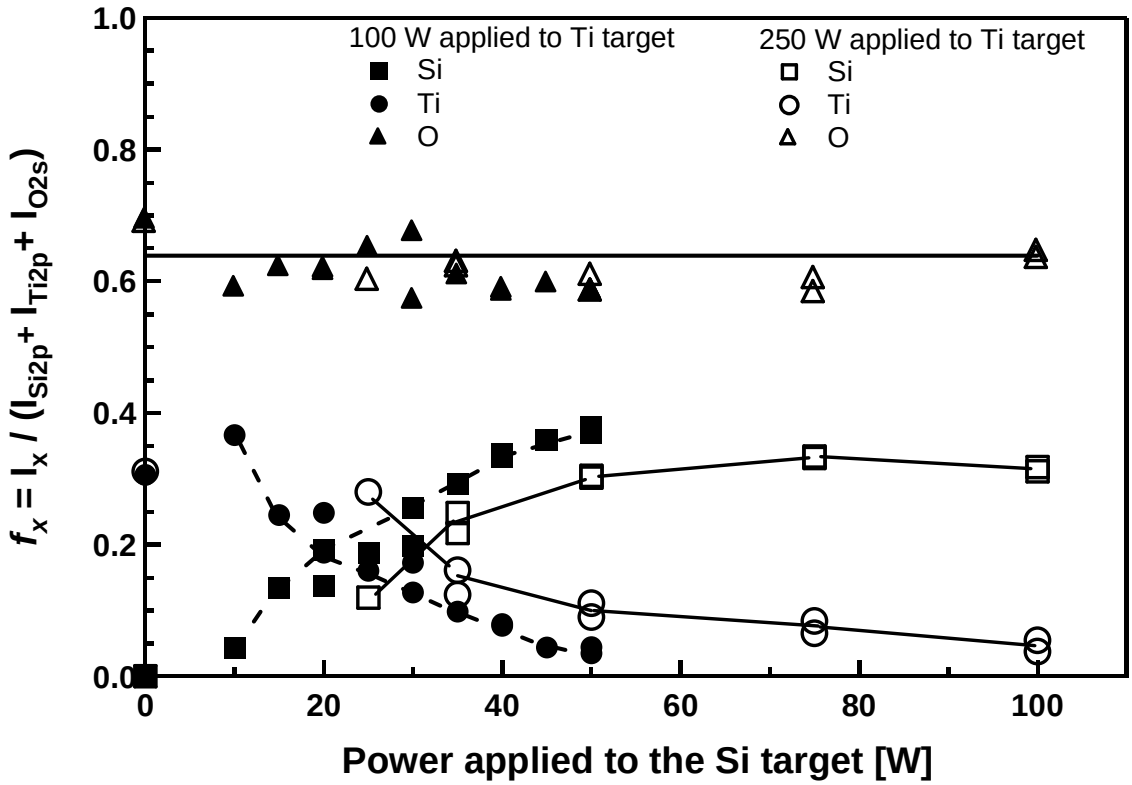

Figure 1: Silicon, titanium and oxygen fraction as a function of the applied power to the Si target. Two different powers were applied to the titanium target: 100 W and 250 W

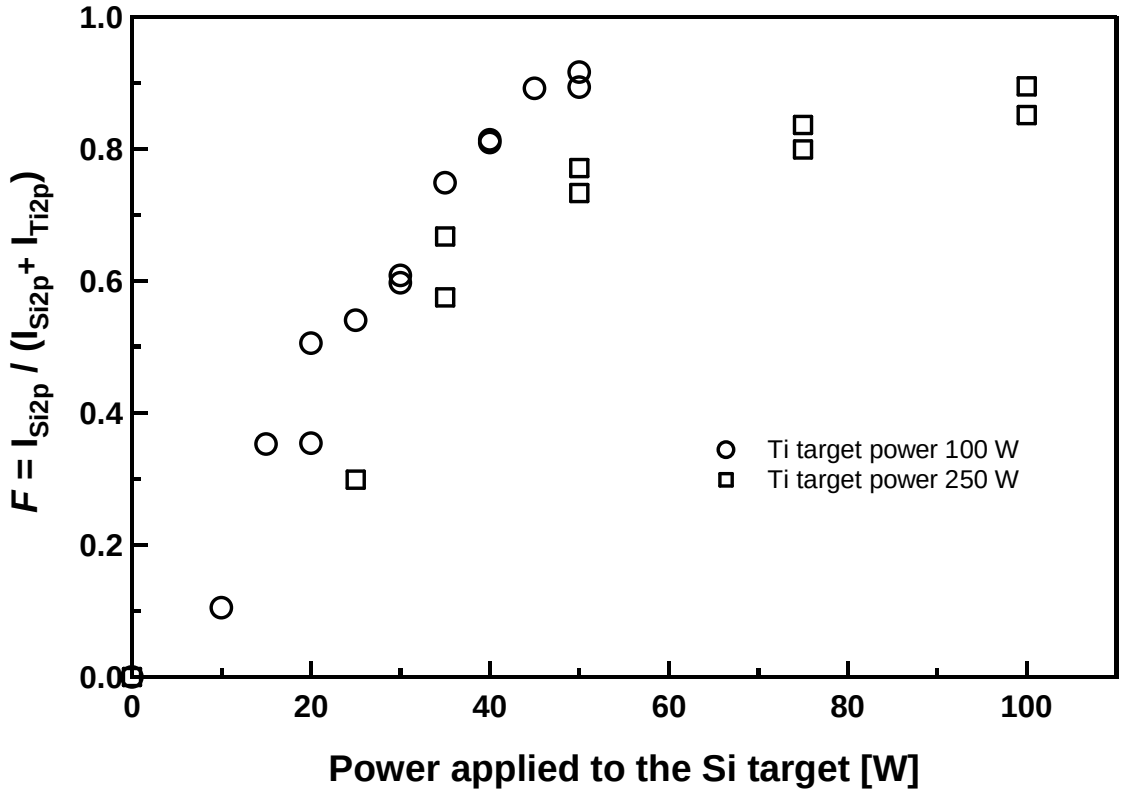

Figure 2: Correlation between the fraction *F* and the applied power to the silicon target for two different powers applied to the titanium target (100 W and 250 W)

Figure 2 represents the correlation between the fraction *F* and the applied power to the Si target. In general, the fraction *F* increases by raising the applied power to the Si target, whatever the applied power to the Ti target. When the applied power to the Ti target is fixed at 100 W, the fraction *F* increases linearly from 0.5 to 0.9 as the applied power to the Si target varies between 20 and 50 W. When the applied power to the Ti target is 250 W, the F fraction increases rapidly for a power between 25 and 50 W applied to the Si target. An applied power to the Si target greater than 25 W slowly increases the *F* fraction from 0.75 to 0.85.

The sample charging problem is commonly considered an experimental obstacle to an accurate determination of binding energies for researchers engaged in the application of photoelectron spectroscopy on poorly conducting surfaces, such as mixed TiO_2-SiO_2 oxide. In the oxides, the positive charge left by the outgoing photoelectron is not compensated by electrons. Instead, a positive surface charge is built up. The surface charge manifests itself in a shift of the whole spectrum to higher binding energies.

Sample charging is therefore expected to appear in the XPS spectra for the investigated dielectric mixed films by XPS due to low electrical conductivity of TiO_2 and SiO_2. As in the previous examples in this work, examining the binding energy difference of elements from the same layer will provide the most reliable bonding information independently of the surface charging. Figure 3 shows the binding energy difference between $Ti2p_{3/2}$ and Si2p of the sputtered mixed oxide Δ(BE $Ti2p_{3/2}$ – BE Si2p). The binding energy difference Δ(BE $Ti2p_{3/2}$ – BE Si2p) of the interacting SiO_2 and TiO_2 phases decreases slightly from 356.8 eV to 356.5 eV by increasing the SiO_2 contents in the composite film. The observed behaviour is independent of the type of the applied power on Ti target: a low 100 W or a high 250 W power. The values found in the NIST Scientific and Technical Databases for mixed TiO_2-SiO_2 oxides are in good agreement with our results. Brunet et al [9] measured a binding energy difference between Ti2p and Si2p varying slightly from 356.2 to 356.6 eV when the TiO_2 concentration increases from 4 to 65 mol.%. The binding energy difference would be between 355.0 eV and 355.6 eV for unmixed SiO_2 and TiO_2 phases obtained by depositing, for example, a thick TiO_2 film on an SiO_2 layer [21]. The obtained result confirms the presence of a mixture of interacting TiO_2 and SiO_2 oxide phases.

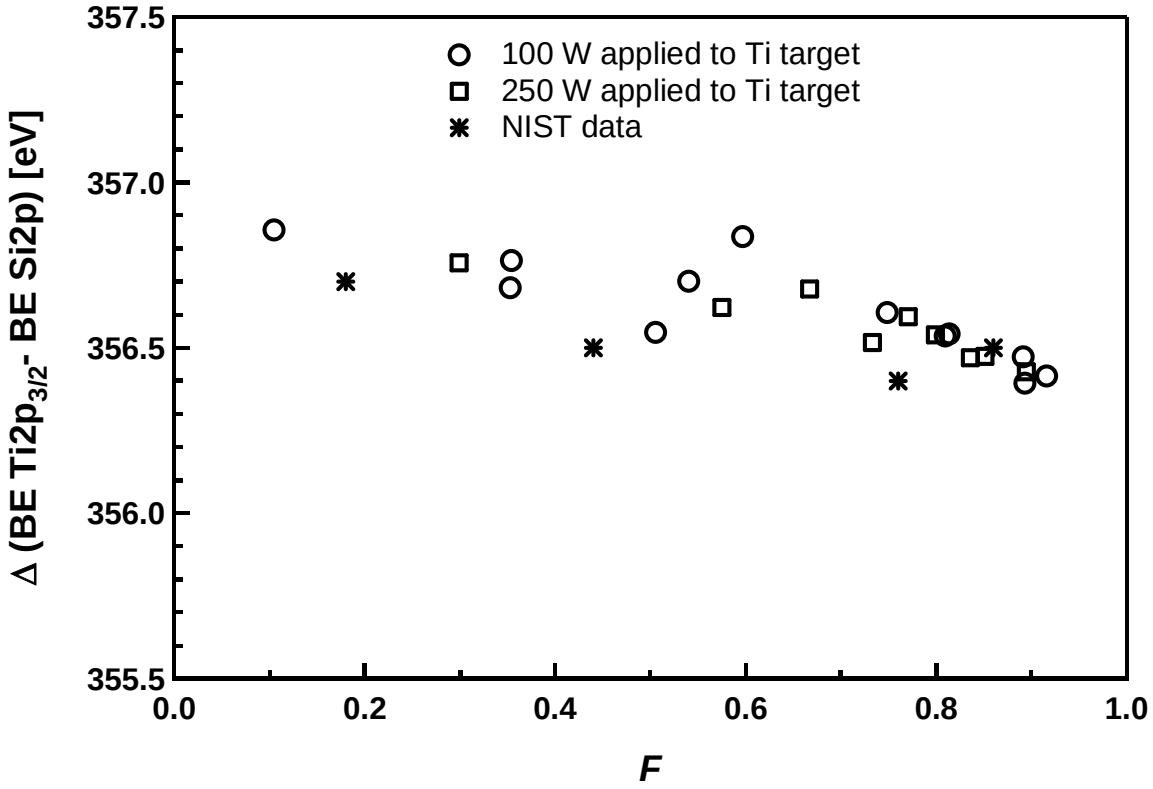

Figure 3: Binding energy difference Δ(BE $Ti_{2p3/2}$ – BE Si_{2p}) between $Ti2p_{3/2}$ related to TiO_2 and Si2p related to SiO_2 core levels depending on SiO_2 fraction in the mixed oxides TiO_2 - SiO_2

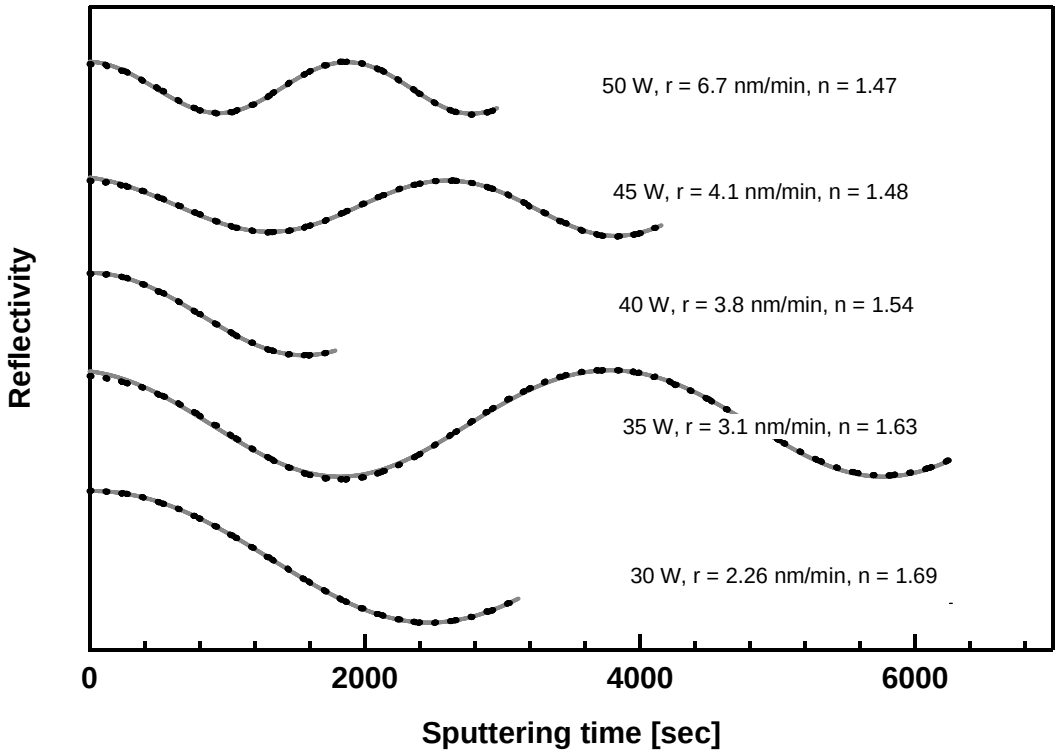

Figure 4: Real-time laser reflectometry during deposition of mixed TiO_2-SiO_2 layers on a silicon substrate as a function of sputtering time. The dashed lines correspond to the experimental data and the solid lines to the fit. The different curves represent different applied power to the silicon target. The applied power to titanium target was 100 W

1.3.2 Laser Reflectometry

Figures 4 and 5 show the real-time reflectivity of the laser beam during deposition of mixed TiO_2-SiO_2 layer on a silicon substrate (40x40 mm^2) as a function of the sputtering time. The dotted lines are the measured data and the solid lines correspond to the fits using a simple model of one single layer on silicon substrate from which the native oxide has been removed. For each mixed oxide film, the amplitudes of oscillating reflectivity curves are constant, which means that the deposited films are transparent to the laser wavelength of 532 nm. A qualitative determination of the refractive index *n* and the extinction index *k* at the wavelength 532 nm of the laser as well as of the deposition rate is made possible by fitting the measured reflectivity. The SiO_2 content in the mixed oxide TiO_2-SiO_2 films and two fit parameters, the deposition rate *r* and the refractive index at 532 nm, are indicated on Figures 4 and 5 for the corresponding reflectivity curves of different mixed TiO_2-SiO_2 oxides. The extinction coefficient is negligible, which confirms that the mixed oxides are transparent film.

The deposition rate is enhanced and the refractive index tends towards the value of pure silicon dioxide (n = 1.47 at 532 nm) by increasing the power applied to the Si target and consequently the SiO_2 content in the mixed oxide.

Figure 6 shows the sputtering rate deduced from laser reflectometry and spectroscopic ellipsometrry versus the applied power to the Si target. The graph summarises the results of the two series, which correspond to two different powers applied to the titanium target (100 and 250W). The deposition rate increases linearly for each series (from 1.3 to 6.7 nm/min and from 5.2 to 25.2 nm/min) by increasing the power applied to the silicon target. In the case of a fixed power applied to the Si target, the sputtering rate is about three times higher for an applied power to Ti target of 250 W than 100 W.

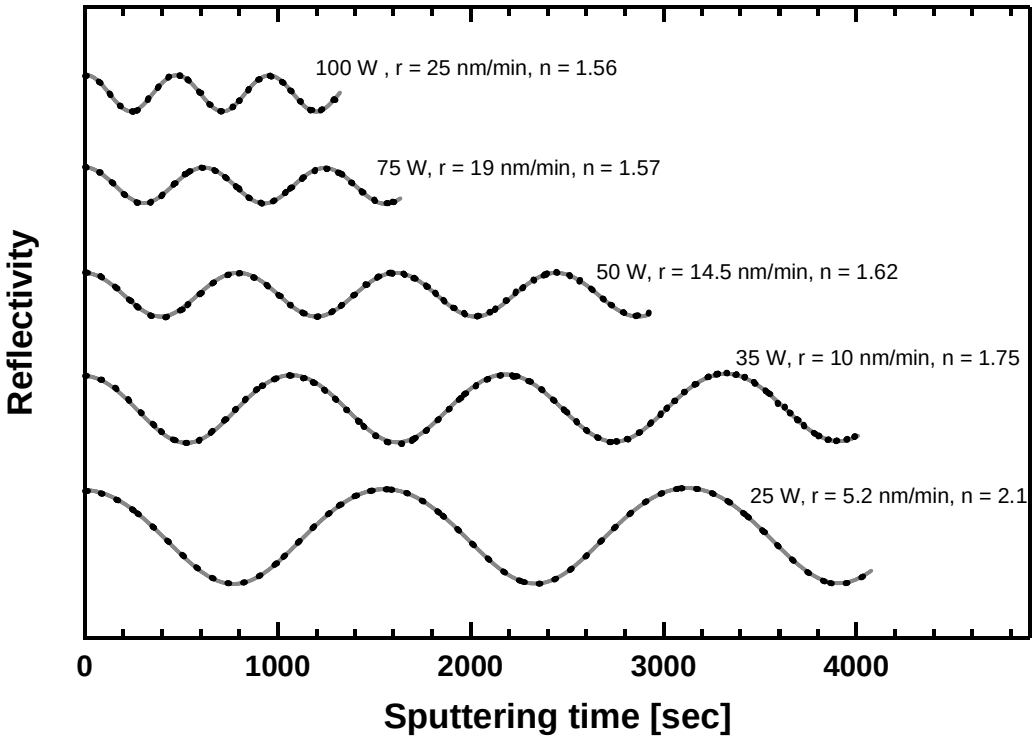

Figure 5: Real-time laser reflectometry during deposition of mixed TiO_2-SiO_2 layers on a silicon substrate as a function of sputtering time. The dashed lines correspond to the experimental data and the solid lines to the fit. The different curves represent different applied power to the silicon target. The applied power to titanium target was 250 W

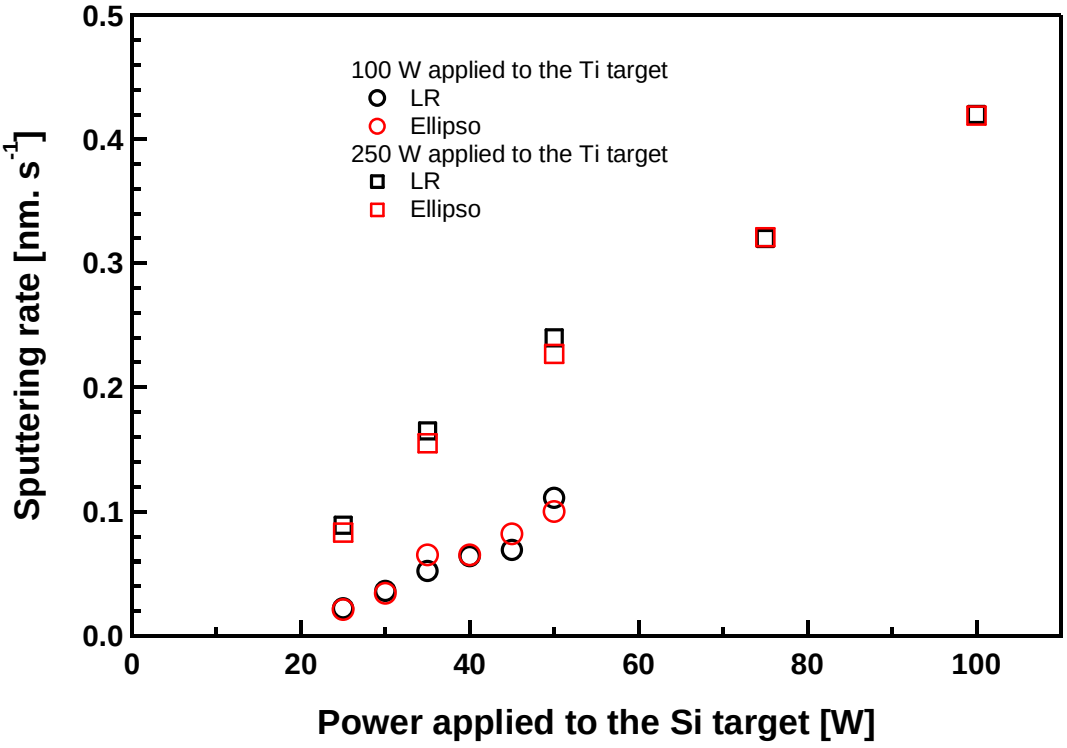

Figure 6: Sputtering rate deduced from real-time laser reflectometry and ellipsometry methods depending on the applied power to the Si target. Two different powers were applied to the titanium target: 100 W and 250 W

1.3.3 Ellipsometry

Ex-situ spectroscopic ellipsometry was performed on the TiO_2-SiO_2 mixed oxides on silicon substrates after deposition and in-situ characterisation by laser reflectometry. A Cauchy formula was used to fit the ellipsometric functions of a uniform layer on substrate to deduce the refractive index dispersion curves. The ellipsometry data confirm that the films are transparent in the visible region.

Two thick films with different content of the mixed TiO_2-SiO_2 oxides were deposited by applying 35 W and 45 W, respectively, to the silicon target. The applied power to the outer titanium target was 100 W. Figures 7 and 8 give the measured and the fitted ellipsometric data for the two samples as an example. The films were fitted with the Cauchy model, which gave a good fit to the measured data in the wavelength range 350-850 nm.

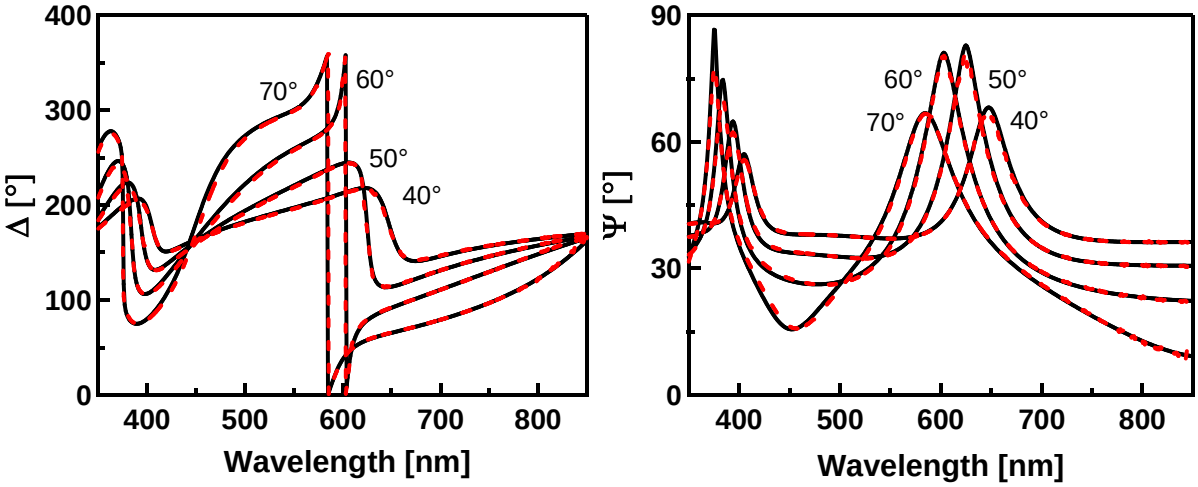

Figure 7: Fitted ellipsometric data for mixed TiO_2-SiO_2 oxides. The applied power to the Si and Ti targets were 35 W and 100 W, respectively. The refractive index was 1.71

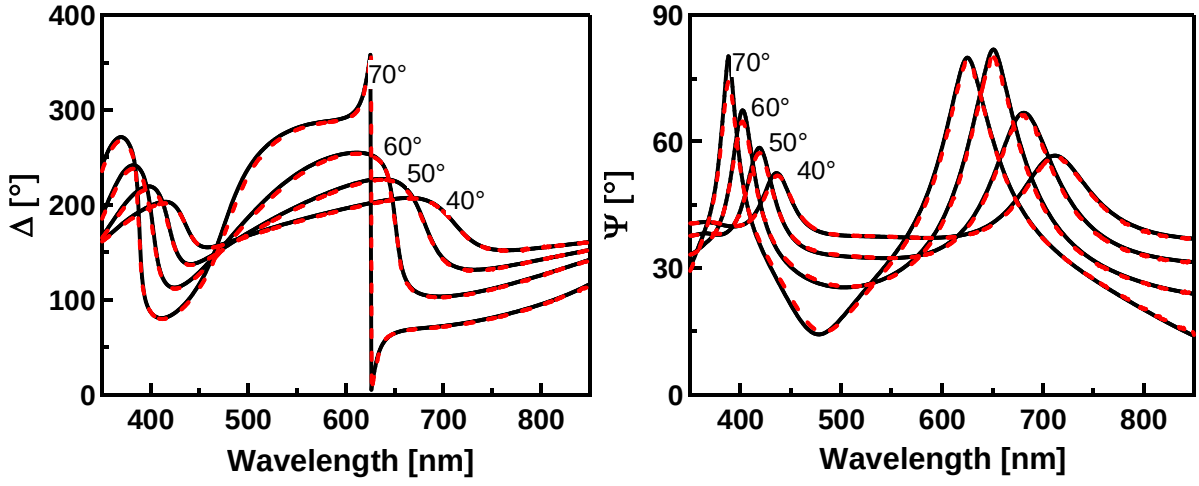

Figure 8: Fitted ellipsometric data for mixed TiO_2-SiO_2 oxides. The applied power to the Si and Ti targets were 45 W and 100 W, respectively. The refractive index was 1.57

Figures 9 and 10 present the refractive index variation for mixed TiO_2-SiO_2 oxide films versus wavelength for a different power applied to the Si target. The applied power on the titanium target is fixed at 100 or 250 W for the represented curves. The dispersion behaviour is more pronounced in titanium oxide rich composite. Different refractive indexes were obtained depending on the silicon content in the mixed oxide. They vary from that of pure titanium oxide to that of pure silicon oxide, by increasing the applied power on the Si target. Consequently, a control of the applied power on Si target allows for the deposit of a mixed oxide, showing the desired refractive index. Figure 11 represents the refractive index of the mixed film as a function of the SiO_2 volume fraction at one given wavelength (532 nm). It regroups the measured data by both methods ex-situ spectroscopic ellipsometry and in-situ laser reflectometry. We compare the determined refractive index of the mixed films with the calculated one from the individual constituents by the effective medium approximation model of Bruggeman [22]. The Bruggeman model assumes spherical unit cells for all constituents in the mixture. For a mixed material consisting of SiO_2 and TiO_2, with respective volume fractions F_{SiO_2} and $F_{TiO_2} = 1 - F_{SiO_2}$ and dielectric functions ε_{TiO_2} and ε_{SiO_2}, the effective dielectric function ε_{eff} is then given by the following equation:

$$F_{SiO_2}\frac{\varepsilon_{SiO_2}-\varepsilon_{eff}}{\varepsilon_{SiO_2}+2\varepsilon_{eff}}+\left(1-F_{SiO_2}\right)\frac{\varepsilon_{TiO_2}-\varepsilon_{eff}}{\varepsilon_{TiO_2}+2\varepsilon_{eff}}=0$$

The Si, Ti and O fractions determined by XPS are used to calculate refractive index by Bruggeman theory. We have supposed that the surface fractions measured by XPS are identical to the bulk fractions. The volume fractions are then derived by using the bulk densities of TiO_2 and SiO_2 films (4.23 g cm^{-3} for TiO_2 and 2.533 g cm^{-3} for SiO_2). At first glance, it appears that the refractive index values deduced from laser reflectometry and ellipsometry methods are equivalent. The assumption of the presence of two phases, silicon oxide and titanium oxide, is sufficient to explain the ellipsometric data in the visible range 350-850 nm. Moreover, a good agreement between the experimental data and the Bruggeman model is observed, which confirms a mixed oxide film and the absence of porosity in the layer.

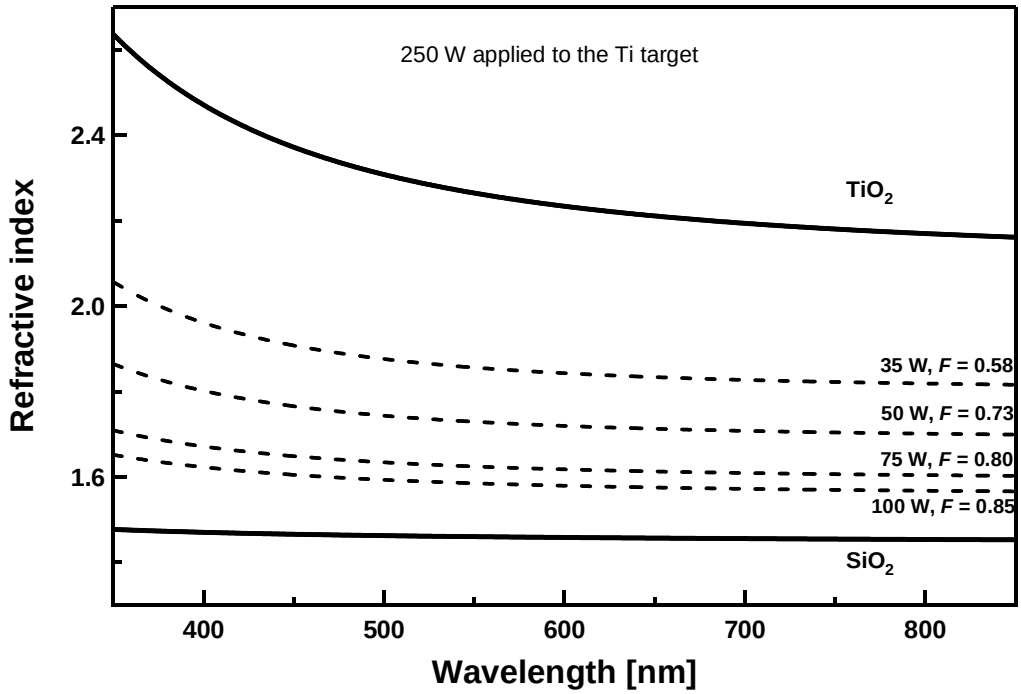

Figure 9: Refractive index dispersion in the visible region determined by ex-situ ellipsometry for different power applied to the Si target. The applied power to the titanium target was fixed at 250 W

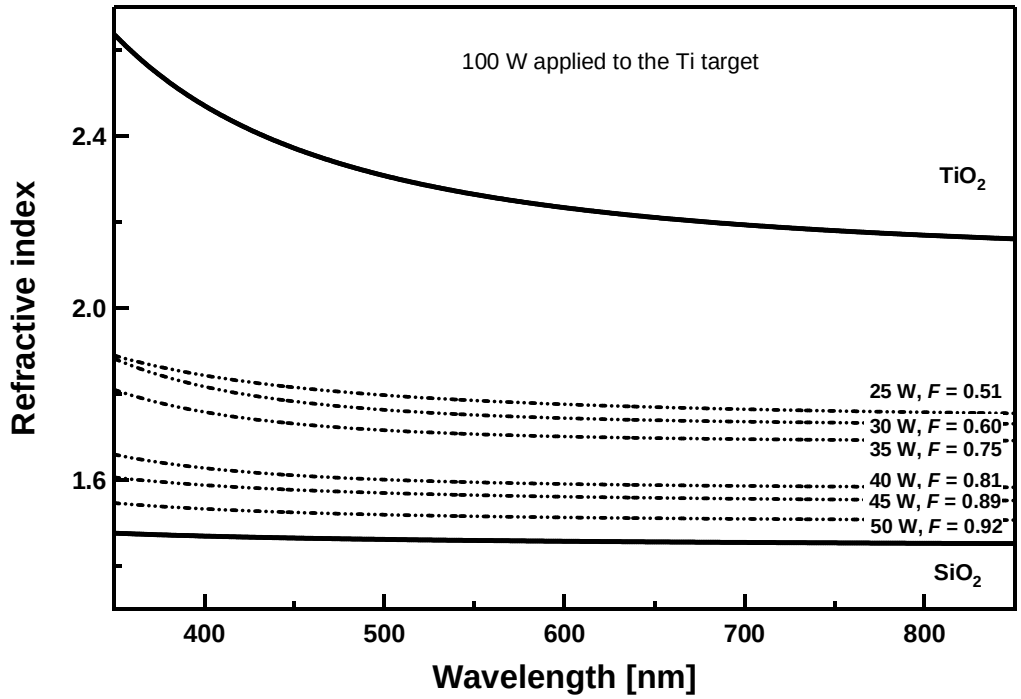

Figure 10: Refractive index dispersion in the visible region determined by ex-situ ellipsometry for different power applied to the Si target. The applied power to the titanium target was fixed at 100 W

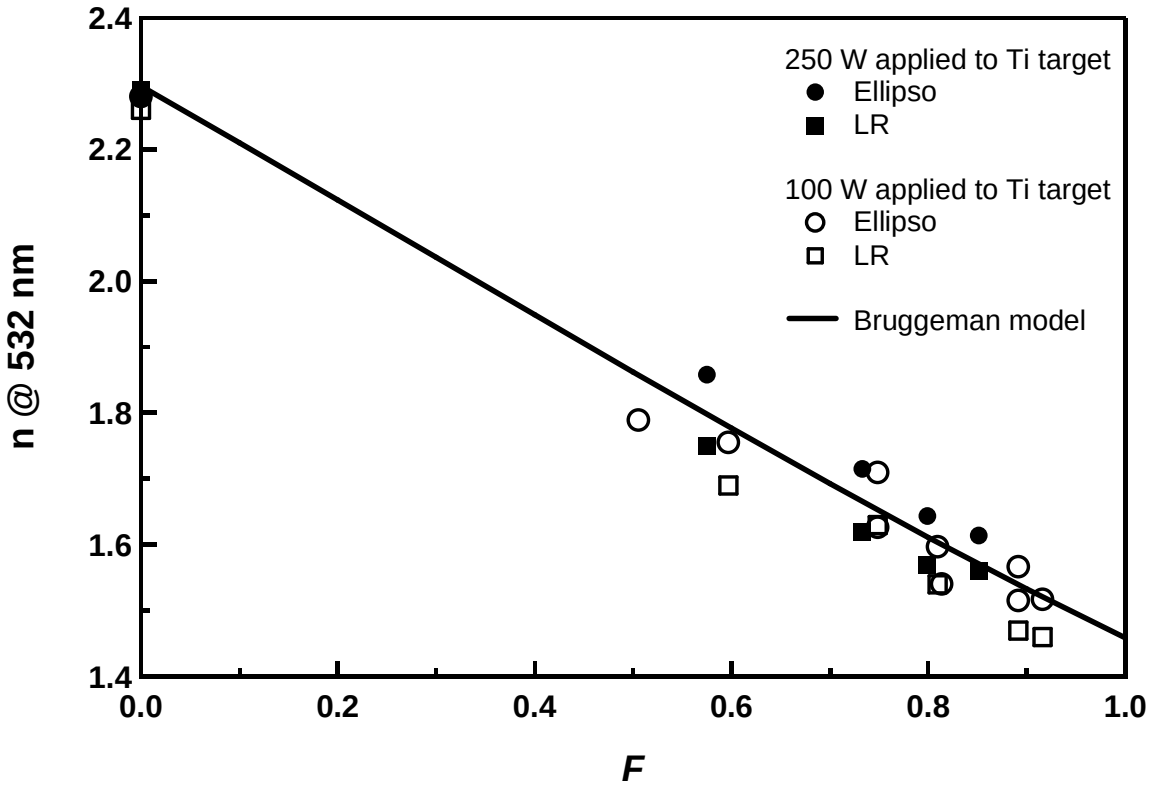

Figure 11: Refractive index at 532 nm determined experimentally by in-situ real-time laser reflectometry and ex-situ ellipsometry. The solid line refers to the calculated refractive index using the Bruggeman model

1.4 Experimental realization of multilayered films

After having analysed the optical properties and the growth velocities for different deposition conditions, we realised several multilayer samples suitable for glazed soar collectors.

1.4.1 Optical properties

An ex-situ optical characterisation was performed on multilayered samples, obtained by alternating TiO_2-SiO_2 mixed oxide and SiO_2 layers on glass substrate. The layers were deposited by sputtering on a 40x40 mm^2 glass the desired thickness of the mixed oxides TiO_2-SiO_2 film followed by the desired thickness of SiO_2 film and the two films were alternated until the desired number of layers was reached.

Figures 12 and 13 represent the total hemispherical reflectivity $R(\lambda)$ and transmission $T(\lambda)$ of two samples with several alternated layers. Thin films of TiO_2-SiO_2, having

two different refractive indexes (1.57 and 1.71), are prepared to realise two series of multilayers.

The first series of multilayered samples was made by choosing an intermediate refractive index 1.71 at 532 nm for mixed TiO_2-SiO_2 oxide. Several samples consisting of 7, 11 or 15 layers were prepared. The thickness of the mixed oxide layer was fixed at 85 nm and that of SiO_2 at 94 nm.

The second series was made from a mixed TiO_2-SiO_2 oxide having a low refractive index of 1.57 at 532 nm, which is closer to that of pure SiO_2. Samples with 11, 15 and 19 layers were deposited. The thickness of a mixed oxide layer was fixed at 95 nm and that of SiO_2 at 94 nm.

For all multilayered samples, the reflectivity peak position is situated in the visible range; see Figures 12 and 13. The observed colour of the light reflected by the samples depends on the wavelength at which the peak maximum is positioned. In our case it is situated close to 560 nm, which corresponds to the green colour.

For the first series, the peak position is situated at approximately 560 nm. The FWHM (Full Width at Half Maximum) of the reflectivity peak decreases from 122 nm to 63 nm by increasing the layers number from 7 to 15 layers. The FWHM is getting narrower from 78 nm to 47 nm by increasing the layers number from 11 and 19 layers.

The reflectivity peak position, its maximum value and its FWHM depend on the layer thicknesses and on the number of layers. In general, for a fixed thickness of the deposited layers, the reflectivity peak maximum at a chosen wavelength increases with an increasing number of layers.

The insert graph in Figure 13 shows the theoretical (dotted lines) and the measured reflectivity curve (solid lines) of a 19-layered sample of alternating mixed oxides TiO_2-SiO_2 and SiO_2. The simulation is performed by taking into account the experimentally measured refractive index of the mixed layer and by supposing sharp interfaces between the two types of materials. This graph illustrates a good agreement between the experimental and the theoretical total reflectivity curve for a 19-layered sample.

The solar transmission, the visible reflectance of the samples, the Lab colour coordinates of the multilayers as well as the peak position of the reflectivity curve and its FWHM are summarised in table 1.

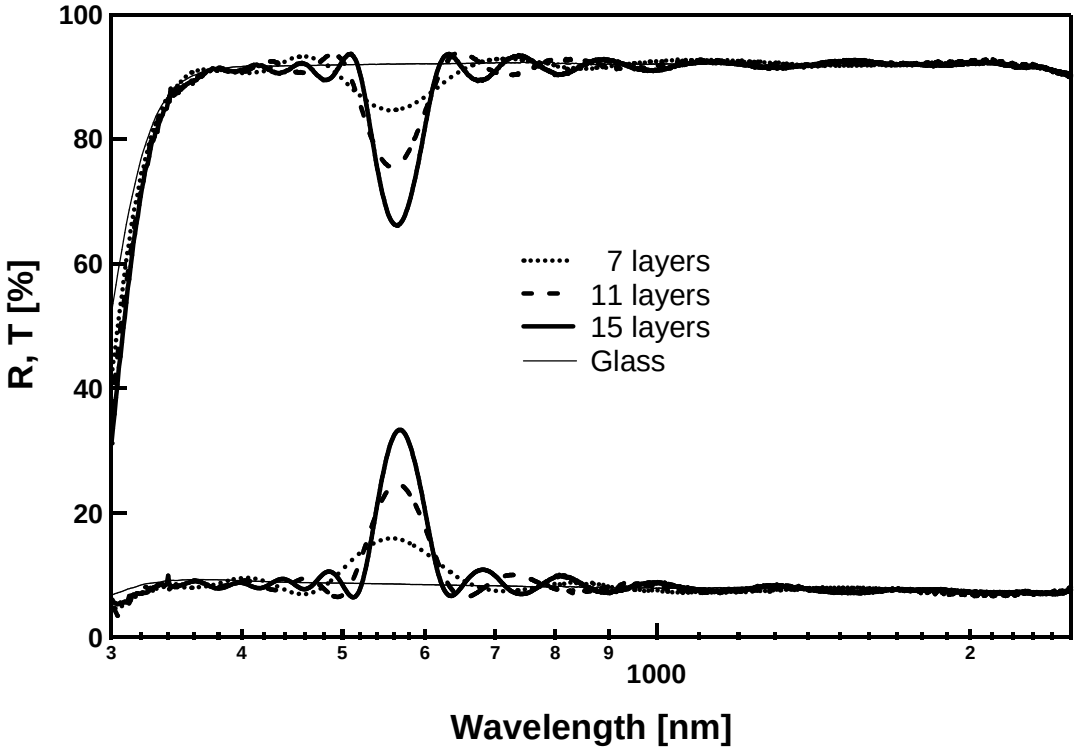

Figure 12: Total hemispherical reflectivity and transmission of the used glass and of multilayered samples deposited on glass consisting of 7, 11 and 15 layers. The TiO_2-SiO_2 mixed oxides have a refractive index of 1.57 at 532 nm

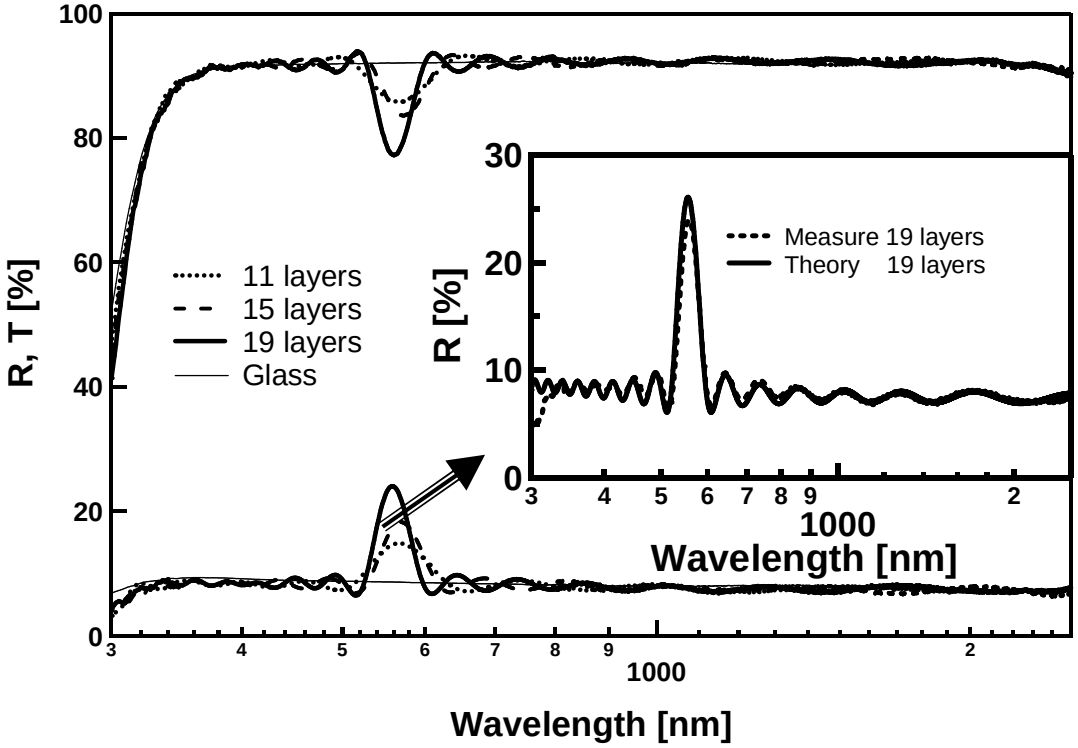

Figure 13: Total hemispherical reflectivity and transmission of the used glass and of multilayered samples deposited on glass consisting of 11, 15 and 19 layers. The TiO_2-SiO_2 mixed oxides have a refractive index of 1.71 at 532 nm. In the insert: measured (the dotted line) and predicted (solid line) total hemispherical reflectivity of a 19-layered sample

***n* (TiO_2+SiO_2)= 1.71 at 532 nm**							
Layers number	T_{sol} (%)	R_{vis} (%)	**Peak position**	**FWHM (nm)**	***L***	***a***	***B***
7 L	90.8	13.9	559	122	44.12	-9.48	17.43
11 L	90.0	17.5	563	78	48.95	-10.40	23.73
15 L	89.2	20.2	567	63	52.09	-9.57	28.25
***n* (TiO_2+SiO_2)= 1.57 at 532 nm**							
Layers number	T_{sol} (%)	R_{vis} (%)	**Peak position**	FWHM **(nm)**	***L***	***a***	***B***
11 L	91.4	11.8	567	78	40.91	-4.27	10.95
15 L	91.4	12.4	568	60	41.79	-4.02	12.30
19 L	91.0	14.2	558	47	44.47	-13.66	16.28
Glass	91.9	1.0	---	---	221.87	-0.89	-3.87

Table 1: Solar transmission, the visible reflectance as well as the Lab colour coordinates of multilayered samples by alternating mixed oxide TiO_2-SiO_2 and SiO_2. The FWHM and the peak position are also reported for the reflectivity peak in the visible region. Two different refractive indexes of TiO_2-SiO_2 mixed oxide are chosen for realising multilayer samples 1.71 and 1.57

A solar transmission higher than 89% was obtained which is close to that of uncoated glass (91.9%). The visible reflectance is proportional to the luminosity and higher than 11.8%. More than 12% relative visible reflectance is considered to be a good value for a coated, coloured glass. The alternative mixed TiO_2-SiO_2 and SiO_2 multilayer with a low refractive index 1.57 at 532 nm, closer to that of pure SiO_2, provides a higher solar transmission 90.9% and an acceptable visible reflectance higher than 11.8% for a layered sample with more than 7 layers. Increasing the sample layers number from 11 to 19 increases the relative luminosity to 14.2% but decreases the solar transmission by 1.5% (90.9%). However, for a mixed TiO_2-SiO_2 and SiO_2 multilayer sample with an intermediate refractive index 1.7 at 532 nm, between that of pure TiO_2 and SiO_2, at least 7 layers are needed to achieve an acceptable relative luminosity of 13.9%. These results show that films with a higher solar transmission and a higher visible reflectance can be obtained.

1.4.2 Accelerated ageing test

An accelerated ageing test is necessary to estimate the lifetime of multilayers on a glass sample. Figure 14 shows the results of an accelerating ageing test conducted under high temperature in atmospheric air. Three identical samples, sized 40 mm x 40 mm, were prepared in a similar way and consist of 7 layers by alternating mixed oxide TiO_2-SiO_2 and silicon oxide SiO_2 on a glass substrate. The refractive index of mixed TiO_2-SiO_2 is 1.75 at 532 nm. The deposited thicknesses are 75 nm for mixed oxide and 94 nm for SiO_2. Each of the three identical samples underwent an annealing at three different temperatures (275°C, 350°C and 450°C) and for a different duration (from 2 h to 128 h). The total hemispherical reflectivity and transmission of each sample was measured after each annealing cycle to follow the influence of both the temperature and the heating time on the optical properties of the deposited multilayer. The experiments show that practically no degradation is observed on the optical properties of 7 layered films, whatever the heating time and annealing temperatures up to 450°C were.

The optical properties after the annealing cycles are conserved and are equivalent to the as-deposited film. The mixed TiO_2-SiO_2 films withstood heating temperatures up to 450°C for a duration of 128 hours under atmospheric pressure. This observation confirms that the mixed silicon and titanium phases are not affected, as has been published by Sankur et al. [10]. Their study has shown that the crystallisation of TiO_2 phase is retarded by the presence of SiO_2 phase. Normally, the pure amorphous titanium oxide phase began to crystallize in the anatase phase at temperature of 350°C. In our case, if we suppose that the as-deposited mixed oxides at room temperature are totally amorphous or a mixture of TiO_2 nanocrystals immersed in amorphous SiO_2, the optical properties are conserved after thermal annealing up to 450°C. It is known that the presence of silicon oxide retards the appearance of the crystallized phase of titanium oxide. This probably means that the presence of silicon oxide in the mixed titania-silica material shifts to a higher temperature; the crystallization point of titanium oxide, as has been confirmed by many works [23].

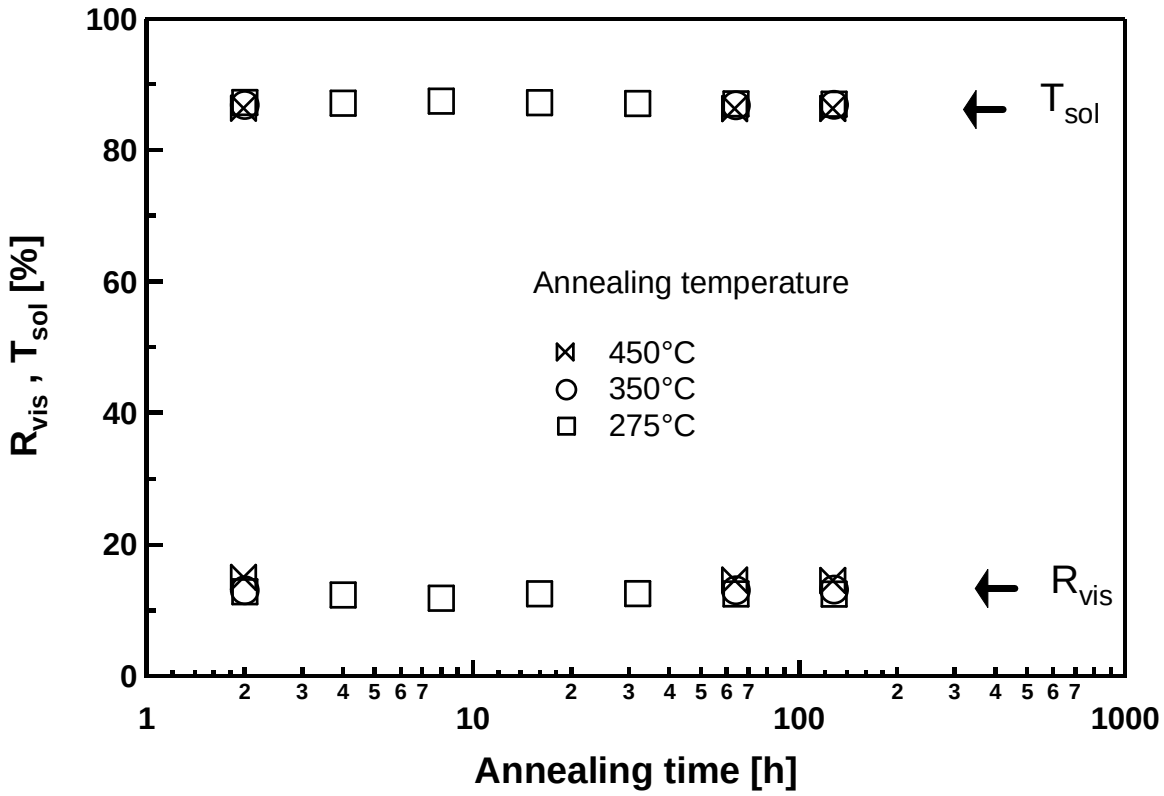

Figure 14: Visible reflectance and solar transmission of three identical multilayered samples after undergoing an ageing test. The annealing took place at atmospheric air for different temperature 275, 350 and 450°C for a heating time up to 128 h

1.5 Conclusion

Alternating layers based on mixed titanium and silicon oxides film and silicon dioxide film were obtained by sputtering process using a double ring magnetron and a simple magnetron, respectively. The applied power to the double ring magnetron capped with titanium and silicon targets allowed obtaining a mixed oxide with different refractive indexes ranging from that of pure titanium dioxide to that of silicon dioxide and described by the Bruggeman effective medium approximation.

By regulating the applied power on the titanium and silicon targets, it is possible to adjust the optical properties of the mixed oxide films to obtain the desired refractive index. The deposited multilayers on glass show a reflectivity peak zone situated in the visible range at approximately 560 nm. The peak intensity can be controlled by varying the fraction of titanium and silicon in the mixed film, the thickness of the films and the number of the alternating layers.

XPS allowed the determination of the chemical composition of co-deposited TiO_2-SiO_2 and confirmed the absence of other contaminants, such as carbon. The laser reflectometry method is a powerful tool for in-situ measurements of the refractive index at one wavelength 532 nm and the deposition rate of the mixed oxide. A complementary ex-situ ellipsometric spectroscopy allowed the determination of the refractive index in the visible range, 350-850 nm.

The sputtered mixed titanium and silicon oxides films are therefore promising candidates for the glazed coloured collectors. The above described optical properties confirm the applicability of alternating mixed titanium and silicon oxides layers with silicon oxide layers as coatings on glass providing a selective reflectivity. Ageing tests showed their stability and their resistance to heat treatments under air up to 450°C.

2 TiO_2 – Al_2O_3 composite films for coloured glazed solar collectors

2.1 Introduction

Significant interest has been generated during the past decade in the field of fabrication of composite oxides. There are a lot of reports on sputtering derived composite films based on the binary oxides, such as TiO_2-Al_2O_3 [24], ZrO_2-SiO_2 [24] TiO_2-SiO_2 [14], ZrO_2-SiO_2 [25]. The preparation of homogeneous composites allows the development of promising materials with different optical properties for various applications.

Titanium dioxide is a widely used material in various optical and electronic devices, such as antireflection, optical coatings, gas sensors, pigments (in paints and cosmetic products), DRAM capacitors, photocatalysis and solar cells [26]. TiO_2 has a high (at λ = 550 nm n = 2.3 for amorphous TiO_2) [2] refractive index and a quasi-zero absorption in the visible. Al_2O_3 finds use in a wide range of technological applications: catalysis, mirror coatings and microelectronics, due to many promising

properties such as high dielectrical constant, high thermal conductivity and transparency over a wide range of wavelengths. The refractive indexes of Al_2O_3 prepared by vacuum deposition lie between 1.6-1.7 [27, 28].

Thin films of TiO_2 and Al_2O_3 are used as high and low refractive index layers for traditional application, such as an optical filter [27]. The optical properties of such filters depend strongly on the optical properties of each material, the thickness of each layer and the number of layers. For future Complementary Metal Oxide Semiconductor (CMOS) devices, mixed TiO_2-Al_2O_3 oxides are considered as an alternative gate oxide to SiO_2 to satisfy the requirements of the next generation integrated circuits due to its high dielectric constant and low tunnelling current [29, 24]. It was found that Ti and Al oxides have lower oxide formation energies than Si, and that amorphous $TiAlO_x$ exhibits an excellent diffusion resistance to oxygen. Consequently, the presence of Ti and Al at the interface with Si is expected to reduce significantly the formation of an interfacial SiO_x layer. It was also established that the mixed TiO_2-Al_2O_3 oxide seems to be the most interesting candidate for electron emitters [30].

TiO_2-Al_2O_3 composite can be used as a dielectric resonator, which displays excellent frequency stability with temperature, very low loss and high thermal conductivity [31]. TiO_2-Al_2O_3 has been attempted in a number of industrially important catalytic reactions. Reddy et al have [32] showed that mixed TiO_2-Al_2O_3 supports can be used as highly promising materials for the dispersion of MoO and hydroprocessing reaction in industry.

In this section, we investigate the possibility to obtain intermediate refractive indexes by mixing different amounts of Al_2O_3 and TiO_2. Co-sputtering using double ring magnetron is employed to fabricate transparent TiO_2-Al_2O_3 composite films from stabilized TiO_2 and Al_2O_3. Chemical composition with various Al_2O_3 content in the mixed oxide film were studied using XPS. Optical properties were determined by combining in-situ laser reflectometry and ex-situ spectroscopic ellipsometry. The realization of periodic TiO_2-Al_2O_3/SiO_2 multilayers with the required selective reflectivity in the visible range and a high solar transmission, [2, 3, 28, 33], was the focus of this work.

2.2 Experimental details

Composite TiO_2-Al_2O_3 dielectric films using reactive sputtering were deposited at room temperature using a double ring magnetron. The water-cooled double ring magnetron sputtering source consists of an inner target capped by Al target and an outer target capped by Ti target.

The experiments are performed in a vacuum system that consists of two interconnected chambers: a sputtering chamber and a photoelectron spectroscopy chamber. The high vacuum sputtering chamber, pumped down to a background pressure of 10^{-6} mbar, was used for the dielectric coatings deposition. The Ti and Al targets were driven by bipolar-pulsed power (50 kHz at 100 W) and by medium frequency RF power (13.5 kHz at 35 to 95 W), respectively. Monocrystalline silicon wafers (100) oriented were used as substrates for XPS analysis and in-situ laser reflectometry. Their native silicon oxides layers were etched using a Kaufman ion gun source. The thin film deposition took place at room temperature, at a fixed distance of 6 cm from the sample and at a working pressure of around 5 x 10^{-3} mbar. High purity argon and oxygen were used as process gases and their mass flow ratio was set to 7:1. Deposition conditions were always run for some minutes before starting a coating on the chosen substrate to achieve stable plasma conditions.

The optical reflectivity of a laser beam was continuously measured in-situ during the sputtering a thick oxide film of several hundreds of nm. The fit of the experimental data was performed using the reflectivity formula of a single layer on the substrate for the numerical fitting [34] to determine the deposition velocity *r* and the optical constants *n* and *k* at a single wavelength, namely 532 nm.

Different TiO_2-Al_2O_3 composites were prepared by keeping the power supply applied to the Ti target constant at 100 W and varying the power supply of the Al target from 35 W to 85 W. Aluminium oxide Al_2O_3 was produced by applying a power of 95 W to the Al target.

An ultrahigh vacuum (UHV) electron spectrometer is connected to the high vacuum deposition chamber. The transfer between the two chambers is done without breaking the vacuum.

The single layers deposited on silicon substrate (40x40 mm^2) measured by in-situ laser reflectometry are subjected to ex-situ ellipsometry measurements, performed by

an SENTECH SE 850 ellipsometer in the range 350-850 nm with a variable angle of incidence ranging between 40° and 70° by steps of 10° to determine the ellipsometric functions Δ and Ψ. The total hemispherical reflectivity at 7° angle of incidence and transmission at 0° angle of incidence measurements in the UV, VIS and NIR are performed on a Varian Cary 5 spectrophotometer for the multilayered samples.

For the multilayered films on silicon or glass, mixed oxide TiO_2-Al_2O_3 and SiO_2 layers were alternately sputtered, the mixed oxide layer with the higher refractive index being deposited on top of the substrate. The TiO_2-Al_2O_3 layer was obtained by applying 65 W or 75 W to the Al target and 100 W to the Ti target. The silicon oxide layer was sputtered using a standard magnetron capped by a silicon target and driven by medium frequency RF power (100 W at 13.5 kHz). The silicon oxide was deposited in the presence of an argon-oxygen gas mixture at a pressure of 5×10^{-3} mbar; the argon-oxygen partial pressure ratio was fixed at 7:1. The distance silicon target-substrate was 5 cm.

2.3 Results and discussion

2.3.1 XPS

The chemical composition of the sputtered films was investigated by integrating Ti 2p, Al 2p and O 1s core lines after subtracting a Shirley background [18]. From the photoionization cross-sections given by Yeh et al. [19], the atomic concentration at the film's surface was calculated using UNIFIT [20]. The O1s line was deconvoluted into two contributions, one at lower binding energy corresponding to Ti-O bounds and the other at higher binding energy related to Al-O bounds. The Ti_{2p} peak was fitted using a doublet and the Al_{2p} peak using a single peak component.

Figure 15 shows the fraction $f_x = I_x/(I_{Al2p} + I_{Ti2p} + I_{O1s})$ of the detected elements by XPS as a function of the power applied to the Al target, $I_x = I_{Al2p,}$ I_{Ti2p} or I_{O1s} being the intensities of the Al2p, Ti2p and O1s peaks, respectively. A decrease of the titanium concentration and an increase of the aluminium concentration in the mixed film are observed by increasing the power applied to the Al target from 35 W to 85 W. The relative content of oxygen slightly decreases over the entire range of applied power to Al target, as is the case for a composite film being a mixture of Al_2O_3 and TiO_2.

Indeed, the oxygen content in TiO_2 is 66%, and in Al_2O_3 60%.The XPS spectra do not indicate phases other than TiO_2 and Al_2O_3. We suppose that the mixed films are a mixture of TiO_2 and Al_2O_3. In that case, the Al_2O_3 fraction is given by $F = I_{Al_{2p}} / \left(I_{Al_{2p}} + 2I_{Ti_{2p}} \right)$.

Figure 16 shows a linear dependence of the *F* fraction on the applied power to the aluminium target. The aluminium oxide fraction in the mixed oxide increases rapidly from 0.30 to 0.95 by increasing the applied power to the Al target from 35 to 85 W. The desired *F* fraction in the mixed oxide is obtained by regulating the applied power to the Al target. This control of the *F* fraction is an appropriate way to handle the optical properties needed for industrial applications.

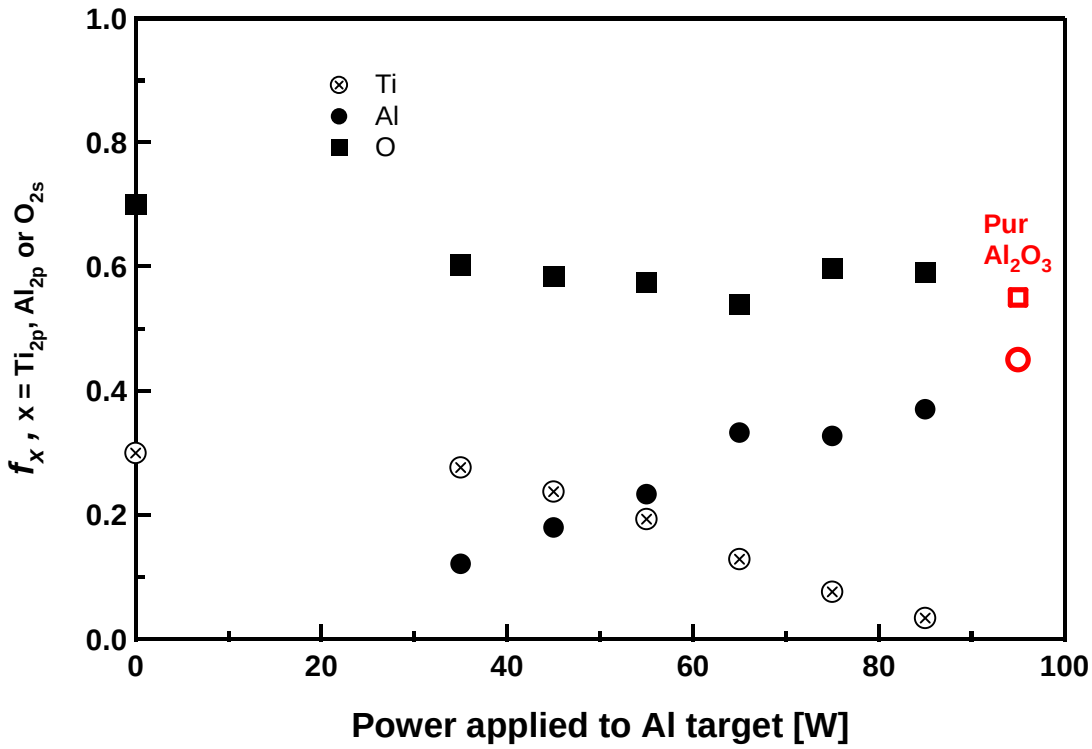

Figure 15: Titanium, aluminium and oxygen fraction f_x as a function of the applied power to the Al target. The applied power to titanium target was fixed at 100 W

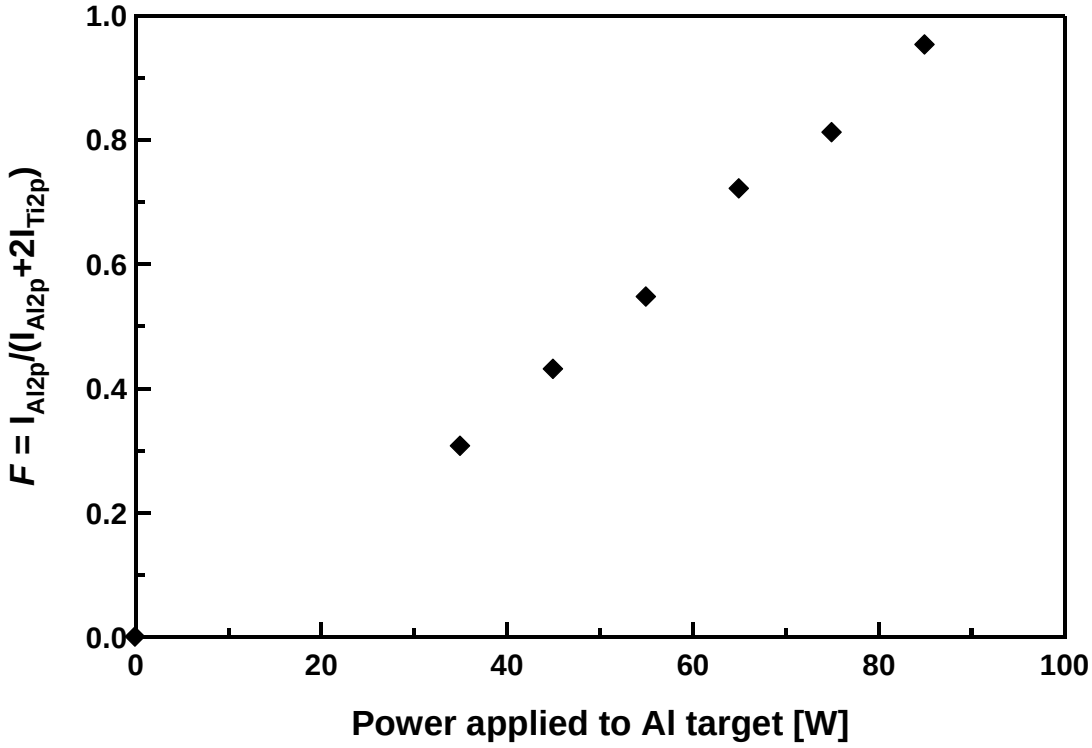

Figure 16: Correlation between the fraction *F* and the applied power to the aluminium target. The applied power to the titanium target was 100 W

In our study, a charging effect is expected to appear for the investigated samples due to low electrical conductivity of TiO_2 and Al_2O_3. Consequently, looking at the difference of the binding energy of elements from the same layer should provide the most reliable bonding information independently of the surface charging effect. Figure 17 shows the binding energy difference Δ(BE Ti2p – BE Al2p) resulting from elements of the composite film versus the applied power to the Al target. The obtained binding energy difference Δ(BE Ti2p – BE Al2p) lies between 384.6 eV and 384.7 eV by increasing the Al_2O_3 contents in the composite film deposited at room temperature. The same binding energy difference value was reported in the literature for a Ti-Al-O coatings deposited by sputtering method at substrate temperature of 300°C and 600°C [35]. Vitanov et al [36] obtained a binding energy difference of 384.4eV for a mixed $(Al_2O_3)_x(TiO_2)_{1-x}$ deposited by spin coating technique.

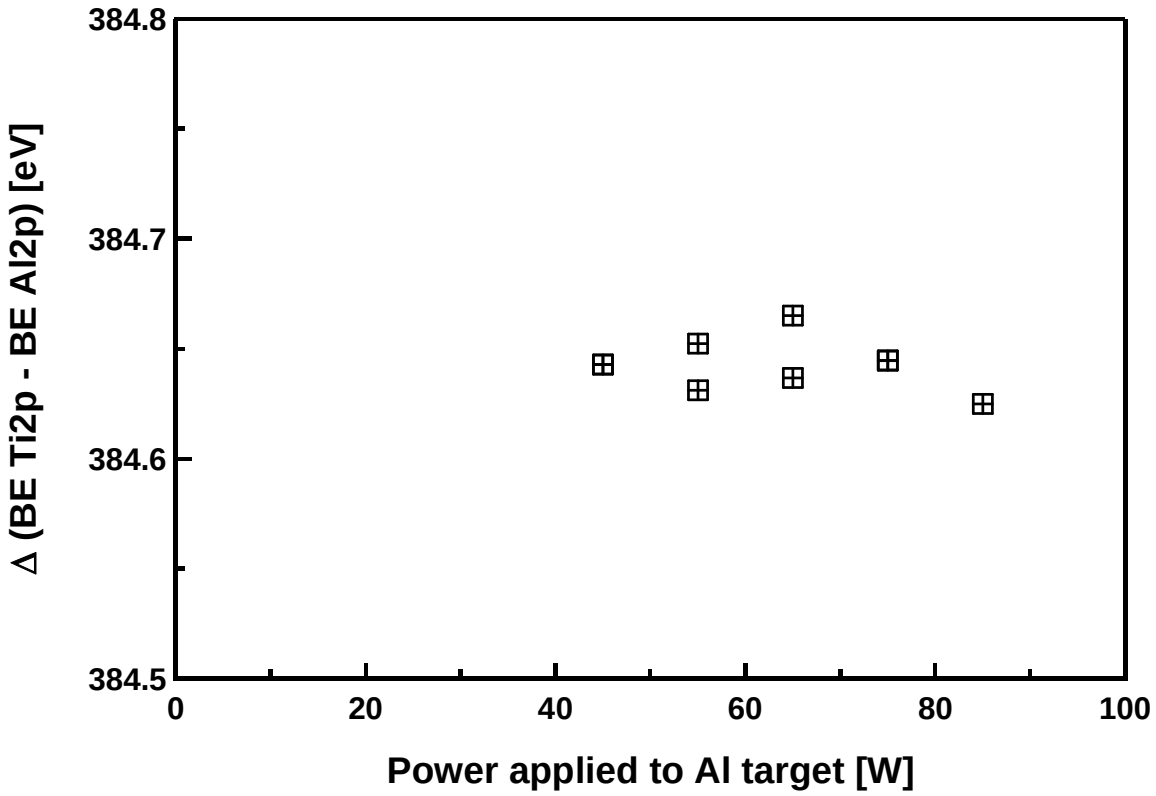

Figure 17: Distance Δ(BE Ti_{2p} – BE Al_{2p}) between binding energy of Ti2p and Al2p core levels depending on the applied power to the Al target

2.3.2 Laser reflectometry

Figure 18 shows the real-time reflectivity of the laser beam used to monitor the growth of mixed TiO_2-Al_2O_3 films on a silicon substrate (40x40 mm^2) as a function of the sputtering time. The applied power to the Ti target being fixed at 100 W and that applied to the Al target was varied from 45 to 85 W.

A close fit (solid line) to the experimental data (dotted line) was represented in Figure 18 using a simple model of one single layer on silicon substrate without its native oxide (removed by sputtering before the mixed oxides deposition). The extracted fit parameters, the deposition rate and the refractive index at 532 nm are indicated for the corresponding reflectivity curves of five different mixed oxides TiO_2-Al_2O_3. The extinction coefficient is negligible. The deposition rate is enhanced and the reflective index tends towards the value of pure Aluminium oxide (n = 1.63 at 532 nm) by increasing the power applied to the Al target.

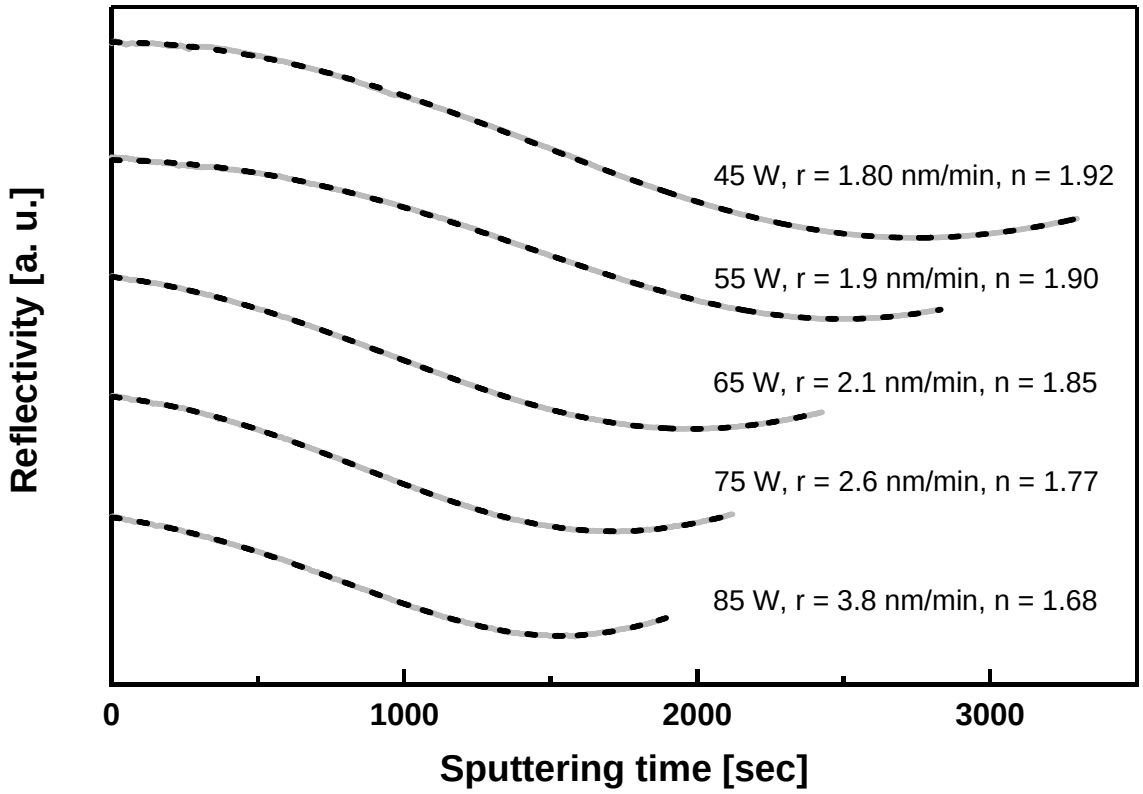

Figure 18: Real-time laser reflectometry during deposition of mixed TiO_2-Al_3O_2 layers on a silicon substrate as a function of sputtering time. The solid lines correspond to the experimental data and the dashed lines to the fit. The different curves represent different applied power to the aluminium target. The applied power to titanium target was 100 W

Figure 19 reports the growth rate of mixed oxide deduced by laser reflectometry. The sputtering rate depends essentially on the applied power to the aluminium target as the power applied to the titanium target was fixed. The deposition rate varies from 1.2 nm/min for pure TiO_2 film to 3.6 nm/min for mixed oxide film with the highest content of Al_2O_3. The growth rate of pure Al_2O_3 is 4.1 nm/min.

2.3.3 Spectroscopic ellipsometry

A Cauchy model was used to fit the measured ellipsometric functions Ψ and Δ of a uniform mixed TiO_2-Al_2O_3 oxide layer—see on Figure 20, as an example, in which case the power applied to the aluminium target was 75 W.

The refractive index, the absorption coefficient and the film thickness were determined by minimising the difference between the measured and the calculated Ψ and Δ parameters of a sample with one layer of mixed oxide in the wavelength range 350 - 850 nm and for different angles of incidence 40-50-60-70°.

The same fitting operation was done for the mixed oxide overlayer films. Figure 21 shows the refractive index dispersion curve of mixed TiO_2-Al_2O_3 oxides films in the wavelength range 350-850 nm for a different power applied to the Al target. The applied power on the titanium target is fixed at 100W for the represented curves. The refractive indexes vary from that of pure TiO_2 to that of pure Al_2O_3, by increasing the applied power on the Al target. A higher content *F* of Al_2O_3 in the mixed oxide implies a lower refractive index approaching that of aluminium oxide.

Consequently, a mixed oxide with the desired refractive index is manufactured by controlling the power applied to the Al target and the Al_2O_3. The corresponding growth rates measured by spectroscopic ellipsometry are shown in Figure 19. A good agreement between the experimental data is obtained.

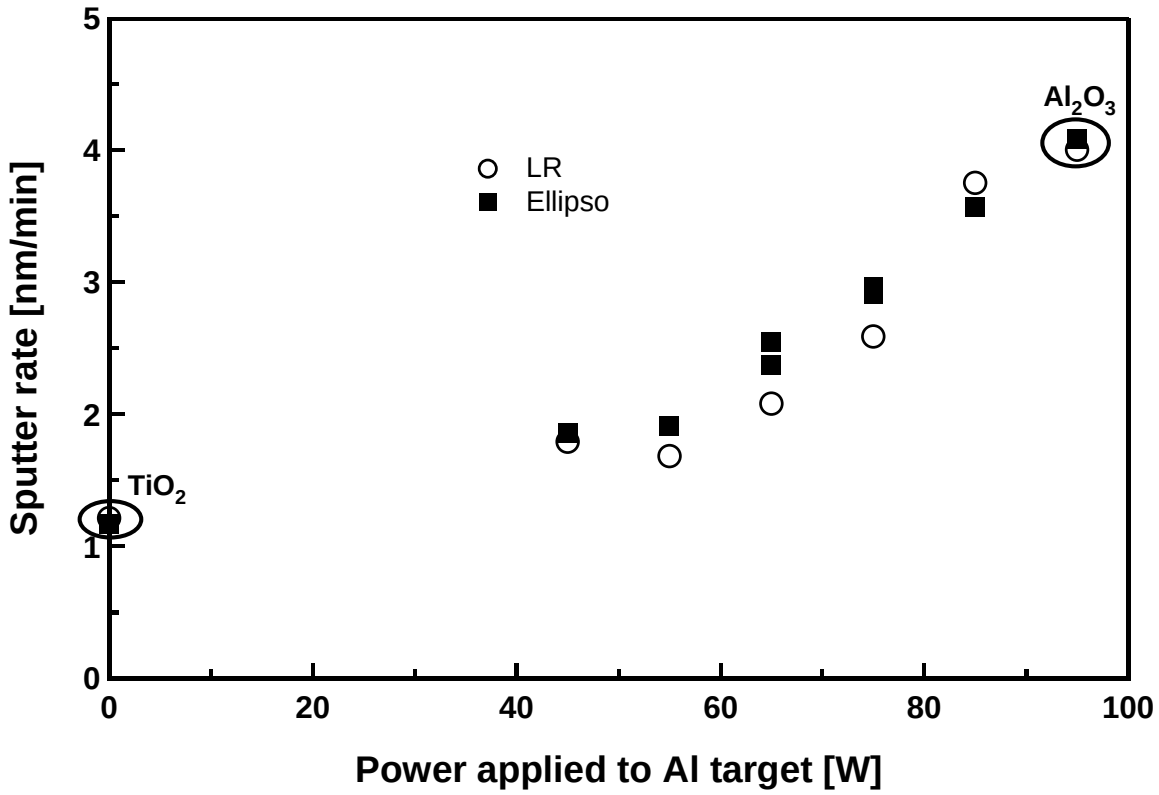

Figure 19: Sputtering rate deduced from real-time laser reflectometry and ellipsometric spectroscopy depending on the applied power to the Al target. The applied power to the titanium target was 100 W

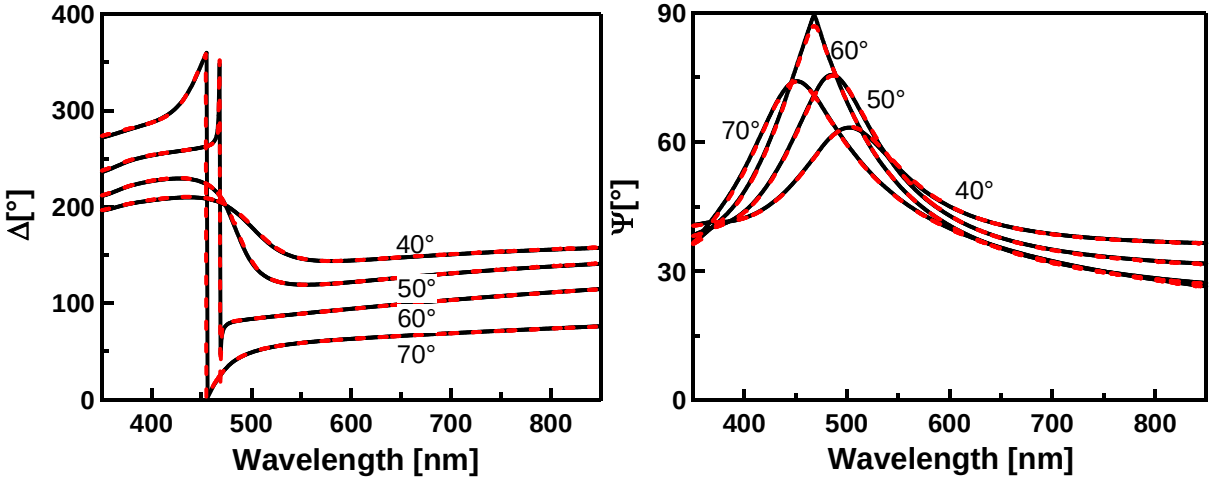

Figure 20: Ellipsometric spectrum of 1 layered mixed oxide film TiO_2 - SiO_2 // Si. The dashed line is the measure and the continuous line is the fit. The applied power to the Al and Ti targets were 75 W and 100 W, respectively. The refractive index of the represented sample is 1.74

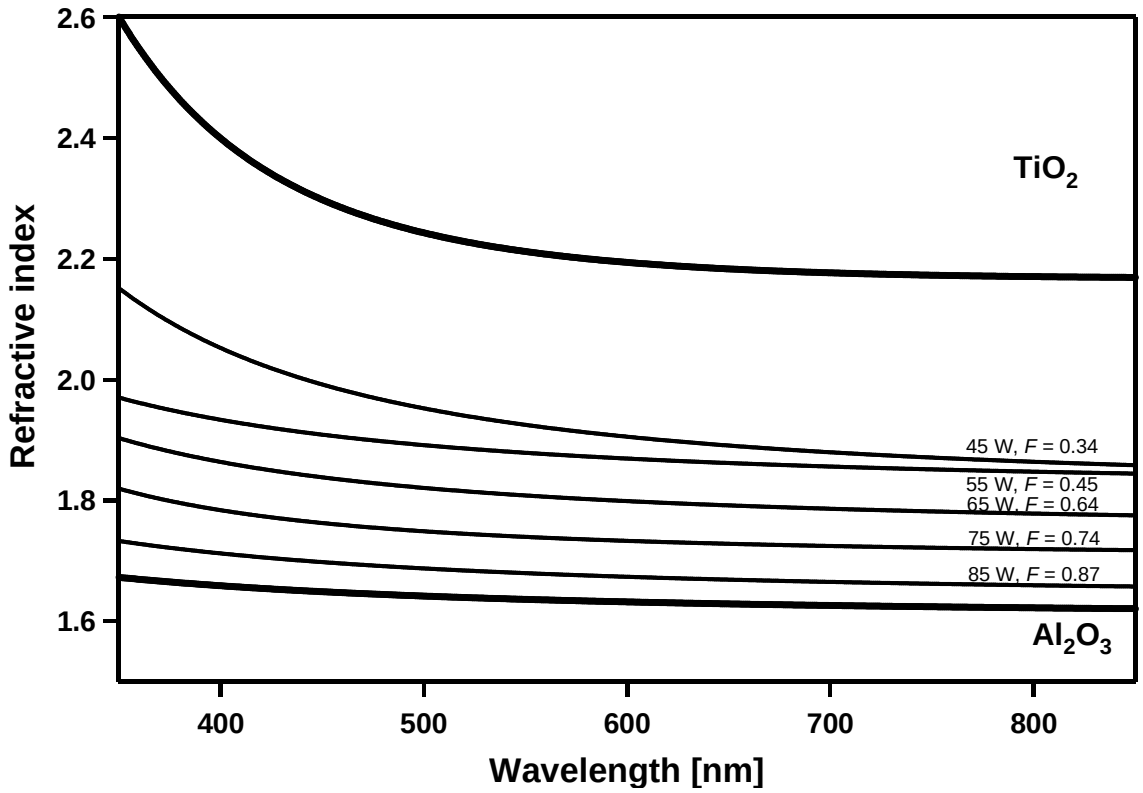

Figure 21: Refractive index dispersion in the visible region determined by ex-situ ellipsometry for a different power applied to the Al target. The applied power to titanium target was 100W

Figure 22 represents the refractive index of the mixed film as a function of the Al_2O_3 volume fraction at one given wavelength (532 nm). It regroups the measured data by both methods, ex-situ spectroscopic ellipsometry and in-situ laser reflectometry. The refractive index of Al_2O_3 at 532 nm is 1.63, which is consistent with the results reported by Kim et al [37]. The lower refractive index in the aluminium oxide film

obtained by the Sol-Gel method (1.54 at 532 nm) compared to sputtered and evaporated films is due to their porous structure [38, 39].

We compare the experimental optical properties data of the mixed films with the optical properties calculated from the individual constituents by the effective medium approximation model of Bruggeman [22]. The Bruggeman model assumes spherical unit cells for all constituents in the mixture. For a mixed material consisting of TiO_2 and Al_2O_3 with respective volume fractions $F_{TiO_2} = 1 - F_{Al_2O_3}$ and $F_{Al_2O_3}$ and dielectric functions ε_{TiO_2} and $\varepsilon_{Al_2O_3}$, the effective dielectric function ε_{eff} is defined using the following equation:

$$F_{Al_2O_3}\frac{\varepsilon_{Al_2O_3}-\varepsilon_{eff}}{\varepsilon_{Al_2O_3}+2\varepsilon_{eff}}+\left(1-F_{Al_2O_3}\right)\frac{\varepsilon_{TiO_2}-\varepsilon_{eff}}{\varepsilon_{TiO_2}+2\varepsilon_{eff}}=0$$

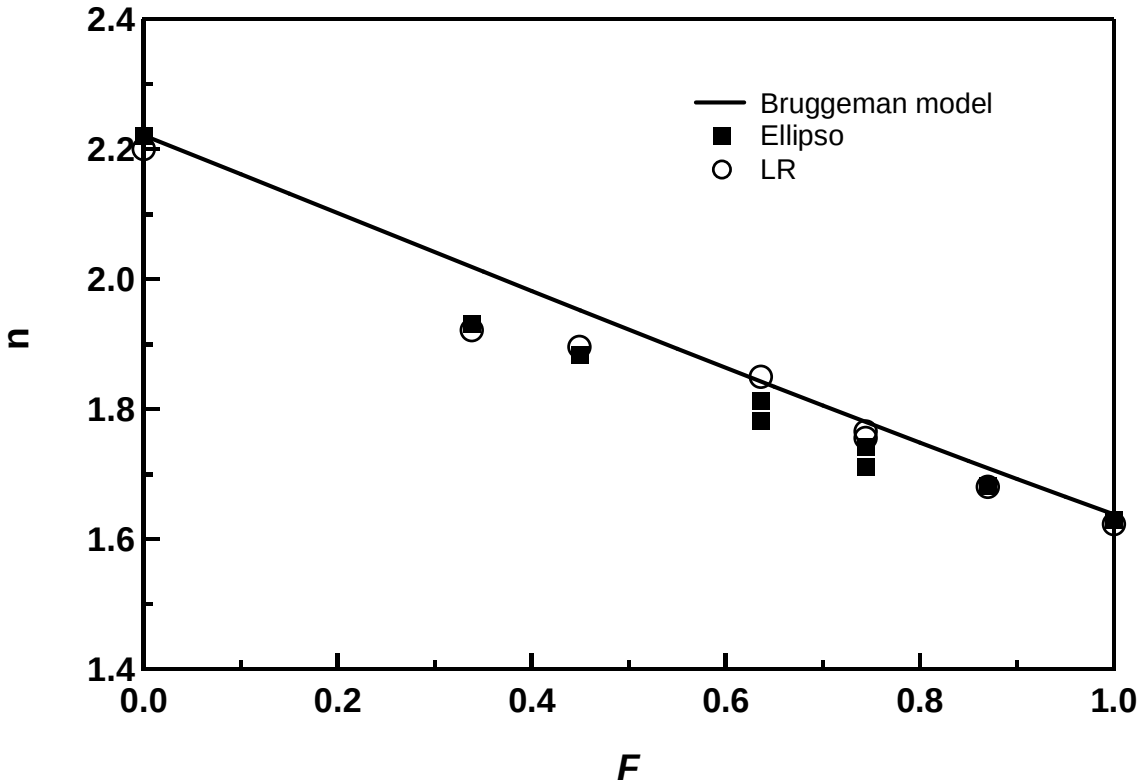

Figure 22: Refractive index at 532 nm determined experimentally by in-situ real-time laser reflectometry and ex-situ ellipsometry versus the Al_2O_3 volume fraction in the mixed oxide TiO_2-Al_2O_3. The solid line refers to the calculated refractive index using the Bruggeman model

The Al, Ti and O fractions determined by XPS were used to calculation the refractive index by Bruggeman theory. We have supposed that the surface fractions measured by XPS are identical to the bulk fractions. The volume fractions were then derived by using the bulk densities of TiO_2 and Al_2O_3 films (4.23 g cm^{-3} for TiO_2 and 4 g cm^{-3} for Al_2O_3). At first glance, it appears that the refractive index values deduced from laser reflectometry and ellipsometry methods are equivalent. An acceptable agreement between the experimental data and the Bruggeman model is observed, which confirm the homogeneity of the mixed oxide film and the absence of porosity in the layer. The difference might be due to the measurement error of the XPS concentrations and the calculated volume fraction.

2.4 Multilayered films with mixed oxide

2.4.1 Optical properties of multilayer films on silicon

The multilayered film on silicon was deposited by alternating the sputtering of several layers, 2, 3 and 5. The TiO_2-Al_2O_3 layer is produced by applying 75 W to the Al target and 100 W to the Ti target. The multilayered samples were fitted by using the refractive index determined previously for the TiO_2-Al_2O_3 and SiO_2 so that the unique fit parameters were the respective thicknesses. The fit to the measured data is reported in Figures 23 to 25.

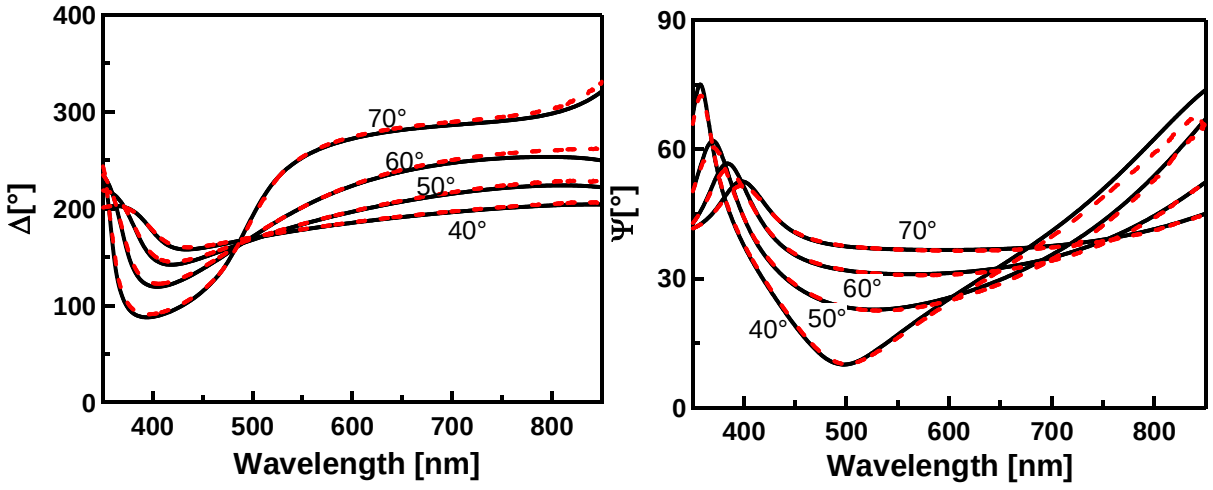

Figure 23: Ellipsometric spectrum of 2-layered sample SiO_2 / TiO_2 - SiO_2 // Si sample

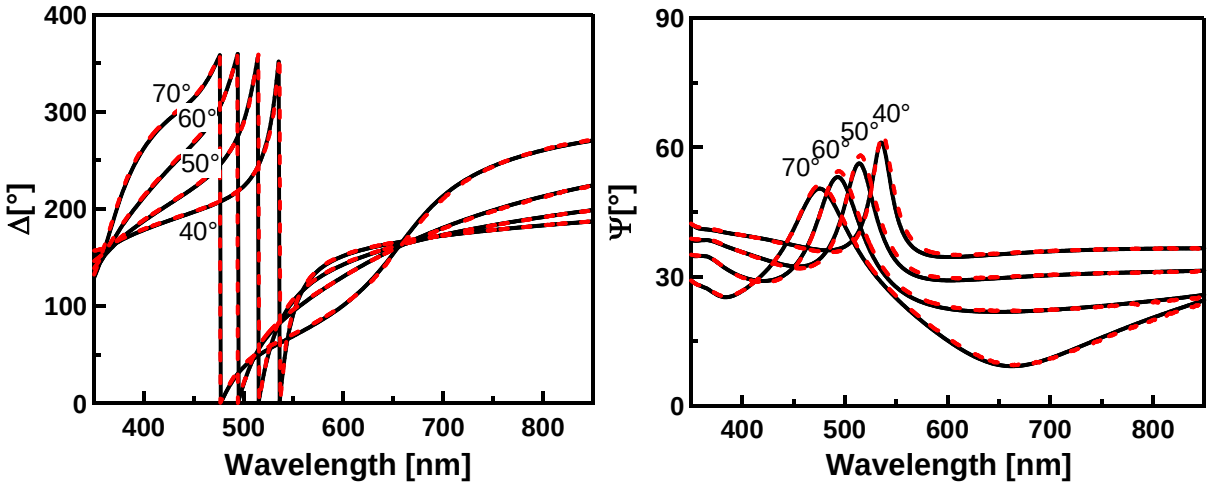

Figure 24: Ellipsometric spectrum of 3-layered sample TiO_2 - SiO_2 / SiO_2 / TiO_2 - SiO_2 // Si

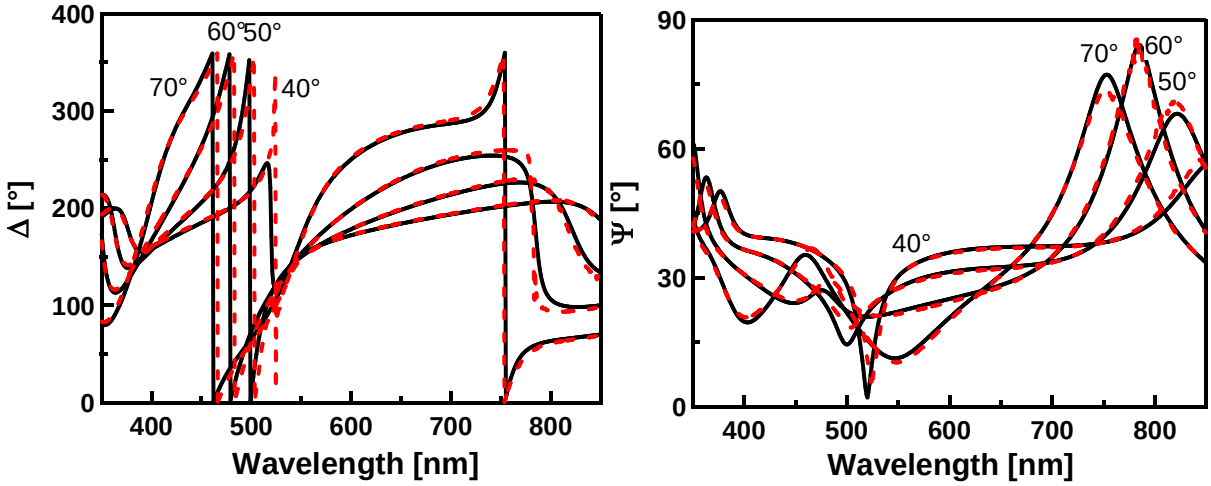

Figure 25: Ellipsometric spectrum of 5 layered sample TiO_2 - SiO_2 / SiO_2 / TiO_2 - SiO_2 / SiO_2 / TiO_2 - SiO_2 // Si

Layer (L) number	Thickness by LR (nm)	Thickness by ellipsometry (nm)	Fit results (nm)
1L TiO_2–Al_2O_3	74	76	76
1L SiO_2	120	115	115
2L	-	-	75/118
3L	-	-	75/116/73
5L	-	-	75/112/70/112/75

Table 2: Deduced thickness by ellipsometry and laser reflectometry (LR) for individual layer and multilayered samples (shown in figures 23-25)

Table 2 summarises the determined thickness by laser reflectometry and ellipsometry for a 1-layered sample of mixed oxide. For the multilayered samples, the thicknesses

of each layer calculated by the fit procedure are reported. These thicknesses are in good accordance with that determined by laser reflectometry and ellipsometric spectroscopy.

2.4.2 Optical properties of multilayer films on glass

Mixed TiO_2-Al_2O_3 oxides with two different refractive indexes were prepared to realise films with 3, 5 and 7 layers. The first series of multilayers were made by choosing a mixed TiO_2-Al_2O_3 with higher refractive index (the applied power to the Al target was 65 W) 1.81 at 532 nm, close to that of TiO_2. The thickness of a mixed oxides layer is fixed at 76 nm and that of SiO_2 at 90 nm. A mixed oxide layer was always first sputtered on the glass substrate.

A second series was made from a mixed TiO_2-Al_2O_3 oxide, having a lower refractive index (the applied power to the Al target was 75 W) 1.74 at 532 nm, close to that of pure Al_2O_3. The thickness of a mixed oxides layer is fixed at 79 nm and that of SiO_2 at 90 nm.

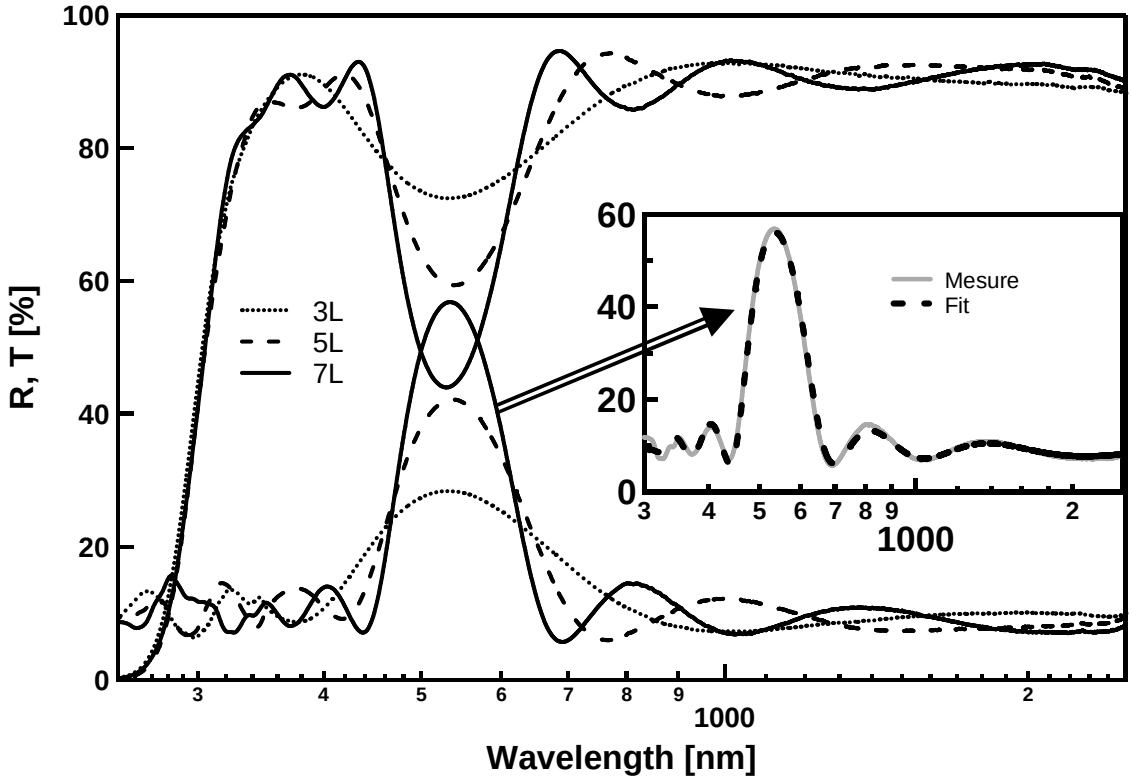

Figure 26: Total hemispherical reflectivity and transmission of the multilayered samples (3, 5 and 7 layers) deposited on glass. The used mixed TiO_2-Al_2O_3 oxide has a refractive index of 1.81 at 532 nm. In the insert: measured (the solid line) and predicted (dotted line) total hemispherical reflectivity of 7-layered sample

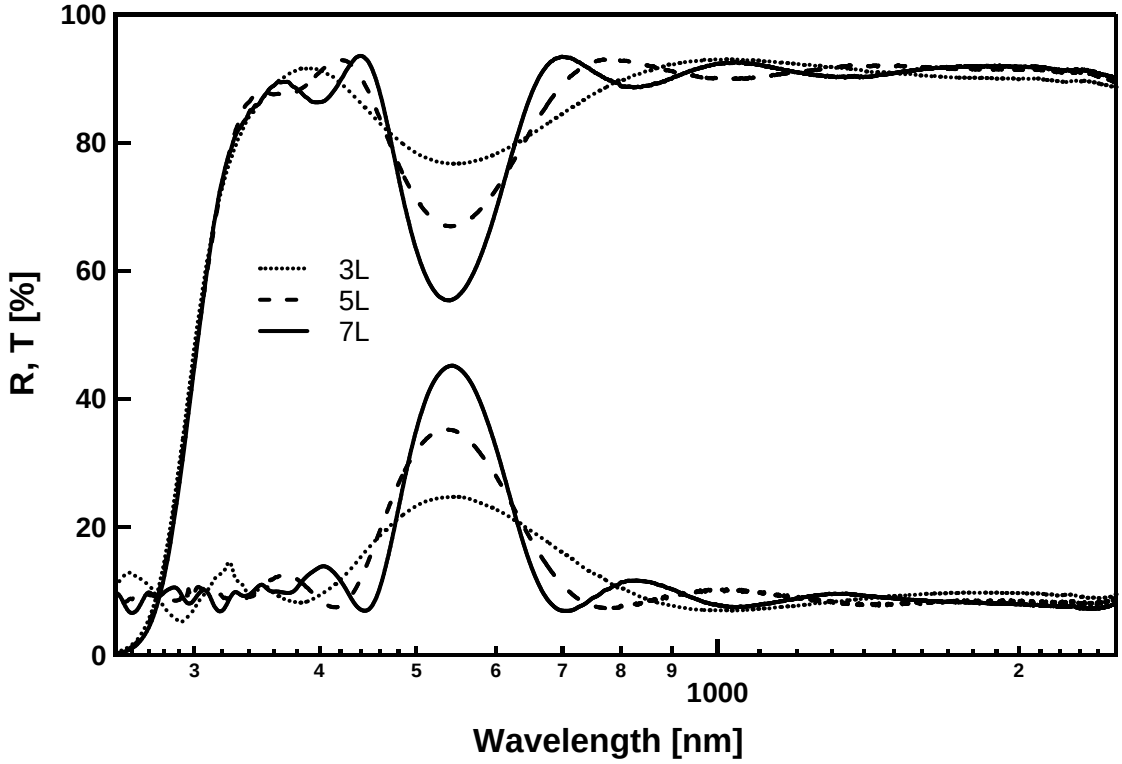

Figure 27: Total hemispherical reflectivity and transmission of multilayered samples (3, 5 and 7 layers) deposited on glass. The used mixed TiO_2-Al_2O_3 oxide has a refractive index of 1.74 at 532 nm

Figures 26 and 27 represent the total hemispherical reflectivity $R(\lambda)$ and transmission $T(\lambda)$ of several multilayered samples. All samples were deposited on a 40x40 mm^2 glass at room temperature.

***n* (Al_2O_3+TiO_2) = 1.81 at 532 nm, applied power to Al target = 65 W**							
nb. layers	**T_{sol} (%)**	**R_{vis} (%)**	**Peak position**	**FWHM (nm)**	**Colour coordinates**		
					L	***a***	***b***
3 L	84.6	26.8	533 nm	244	58.82	-9.55	9.30
5 L	83.0	37.5	537 nm	164	67.68	-22.78	25.54
7 L	81.3	46.9	534 nm	135	74.19	-39.44	40.22
***n* (Al_2O_3+TiO_2) = 1.74 at 532 nm, applied power to Al target = 75 W**							
3 L	86.3	23.5	545 nm	248	55.60	-8.67	11.41
5 L	85.3	31.3	537 nm	168	62.81	-20.94	23.17
7 L	84.1	37.8	543 nm	133	67.88	-31.39	42.01
Glass	91. 9	1.03	--		221.9	-0.89	-3.87

Table 3: Determined solar transmission (T_{sol}), visible reflectance (R_{vis}), reflectivity peak position, FWHM of the peak and Lab coordinates for multilayered samples reported in Figures 26 and 27

Table 3 summaries several parameters of the multilayer samples of both series, such as high reflectivity peak position, its FWHM (Full Width at Half Maximum), reflectivity peak height, solar transmission, visible reflectance of the samples as well as the Lab colour coordinates wherein *L*, *a*, *b* form a three-dimensional coordinate system.

For the first series the reflectivity peak position is situated at approximately 533 nm. By increasing the layers number, the FWHM (Full Width at Half Maximum) decreases from 244 nm to 135 nm and the reflectivity peak height (18.5% to 31.9%) increases. As a consequence, the solar transmission drops from 84.6% to 81.3% and the visible reflectance increases from 26.8% to 46.9%.

For the second series the reflectivity peak position is situated at approximately 540 nm. The FWHM is getting narrower from 240 to 133 nm and the reflectivity peak height increases (16.4% to 26.0%) by increasing the layers number from 3 to 7 layers. The solar transmission drops from 86.3% to 84.1% and the visible reflectance increases from 23.5% to 37.8%.

It is important to know that the reflectivity peak position, its maximum value and its FWHM depend on the layer thicknesses and on the number of layers. For example, the reflectivity peak position at a chosen wavelength of a multilayered sample increases by increasing layers number. The inserts of Figure 26 and 27 show the experimental total reflectivity (solid line) and the calculated reflectivity for the 7 layered samples having a refractive index of 1.81 and 1.74, respectively. To calculate the total reflectivity curve of the 7-layered sample, the thicknesses of the different layers determined by ellipsomety were used. To fit the ellipsometric parameters, the optical constants of the mixed oxide film were used; see Figure 21. A good accordance between the calculation and the measurement is obtained.

A comparison of both series shows on one hand that the solar transmission of the second series (86.3%) presents a 2-3% higher value compared to the first one (84.6%) for the same number of deposited layers. On the other hand, the second series shows a visible reflectance lower than that of the first one. However, more than 12% relative visible reflectance is considered to be a good value for a coated coloured glass. A high visible reflectance seems to be possible for a relatively small number of layers. The critical parameter in this case is the solar transmission, which should be as close as possible to the solar transmission of the glass (92%) to minimize the energy losses due to glass coatings.

Figure 28 shows that the total reflectivity of 7 layered samples realised using TiO_2-Al_2O_3 oxide with a refractive index of 1.74 and 1.81 at 532 nm depending on the angle of incidence 0°-60° predicted using the spectra ray tool based on the experimental parameters. This effect is particularly important for the integration of glazed solar collectors on the roof or on the building's sides. In both graphs, the reflectivity peak position shifts to low wavelength depending on the incident angle, which directly influences the colour seen by human eyes. It is important in the field of solar collector application to be able to choose the colour and to know the resulting colour depending on the incident angle. Table 4 summarises the solar transmission, the visible reflectance and the colour resulting from light reflection of the glazed samples. The solar transmission is increasing slightly by increasing the incident angle from 0° to reach its maximum at 40°. The incident angles of 60° results in a solar transmission lower than 0°. Therefore, the variation of angle of incidence is not always a drawback because the effect can be used to change the colour; see Figure 29.

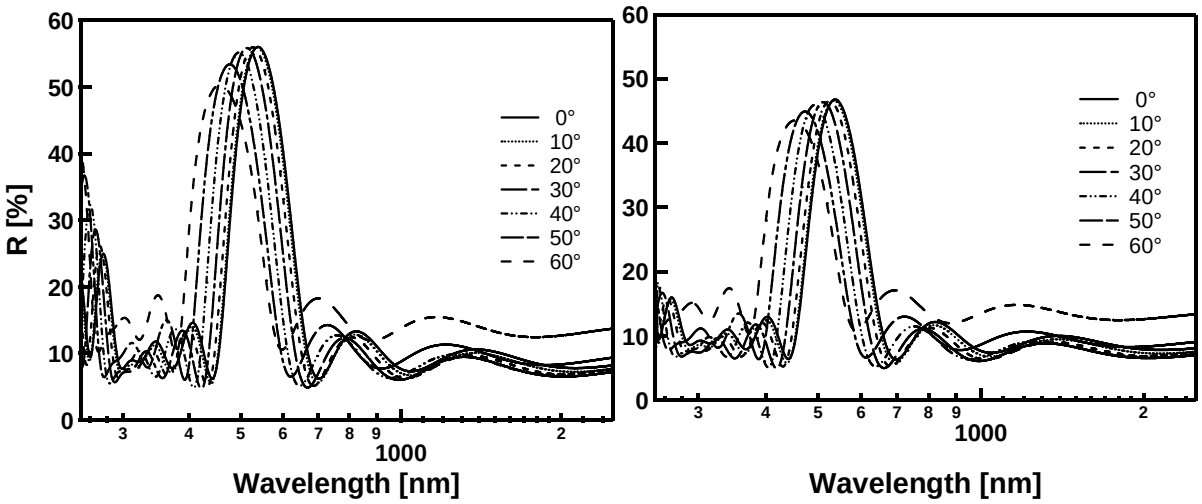

Figure 28: Theoretical total hemispherical reflectivity of two multilayered samples (7 layers) deposited on glass versus angle of incidence from 0° to 60°. The mixed TiO_2-Al_2O_3 oxide has a refractive index of 1.81 (left graph) and 1.74 at 532 (right graph)

n (Al_2O_3-TiO_2) = 1.81 at 532 nm					
7L layers	T_{sol} (%)	R_{vis} (%)	*L*	*a*	*b*
0°	81.1	47.3	74.41	-35.52	45.5
10°	81.6	46.8	74.07	-38.53	43.61
20°	82.1	45.2	73.04	-43.36	34.8
30°	82.6	41.6	70.59	-47.37	17.8
40°	82.7	35.4	66.10	-45.02	-4.27
50°	82.2	28.5	60.31	-32.52	-23.6
60°	79. 5	24.5	57.25	-6.04	-8.41
n (Al_2O_3-TiO_2) = 1.74 at 532 nm					
0°	83.7	38.83	68.66	-34.88	40.19
10°	84.2	38.2	68.21	-37.96	38.42
20°	84.7	36.6	66.97	-42.64	29.88
30°	85.1	33.1	64.24	-45.77	13.29
40°	85.2	27.6	59.56	-40.98	-8.19
50°	84.5	22.0	54.06	-24.82	-26.5
60°	81.4	19.9	51.96	-5.14	-32.2

Table 4: Determined solar transmission (T_{sol}), visible reflectance (R_{vis}) and Lab coordinates as a function of the incident angle for 7-layered samples reported in Figure 28

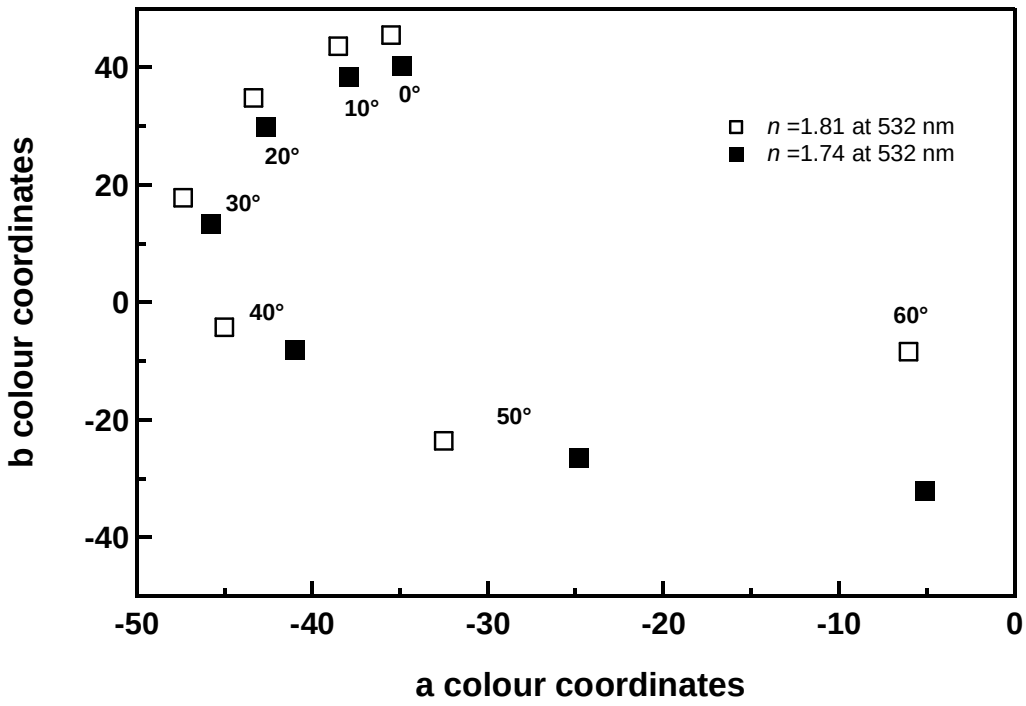

Figure 29: ab coordinates as a function of the incident angle for 7 layered samples

2.4.3 Ageing test

An accelerated ageing test was used to estimate the lifetime of multilayers on a glass sample. It was conducted under different high temperatures (275°C, 350°C, 450°C) in atmospheric air.

The results of the accelerating ageing test of three identical glass samples are summarized in Figure 30. The samples are prepared in a similar way and consist of 5 layers by alternating mixed TiO_2-Al_2O_3 oxide and silicon oxide SiO_2. The refractive index of mixed TiO_2-Al_2O_3 oxide film is 1.74 at 532 nm. The deposited thicknesses are 79 nm for mixed oxide and 90 nm for SiO_2. Each of the three identical samples underwent an annealing at three different temperatures (275°C, 350°C and 450°C) and for a different duration (from 2 h to 64 h).

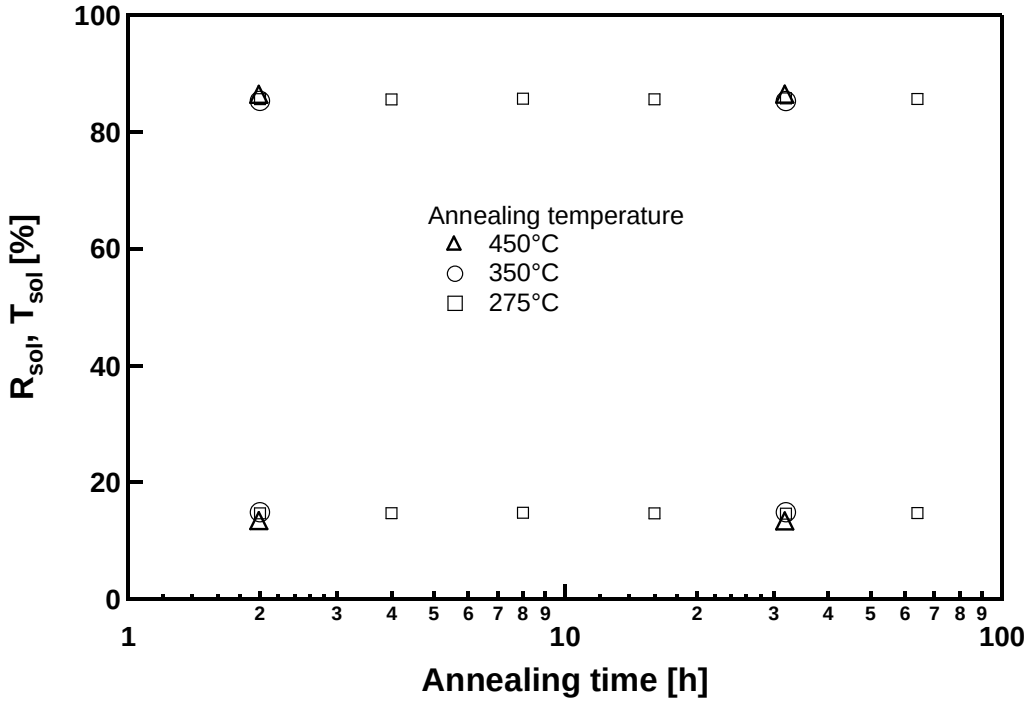

Figure 30: Solar reflectivity and transmission of three identical 5-layered samples after undergoing ageing test. The annealing took place at atmospheric air for different temperatures 275, 350 and 450°C for a heating time up to 64 h

The solar reflectivity and transmission of each sample were measured simultaneously after each annealing cycle to follow the influence of both the temperature and the heating time on the optical properties of the deposited multilayer. The experiments showed that no degradation is observed on the optical properties of 5-layered films whatever the heating time, up to 64 h and annealing

temperatures up to 450°C. Kuo at al [40] reported the same observation. They found that annealing temperature in the range 200-500°C has no apparent effect on dielectric properties of Al_2O_3-rich alumina-titania system. From the results of ageing cycles, we can conclude that the optical properties of mixed TiO_2-Al_2O_3 oxides, in our case, are not affected by annealing process at temperature up to 450°C. Moreover, the mixture of aluminium oxide with TiO_2 retards the crystallisation of the titanium oxide phase. The crystallization temperature of titanium oxide is shifted to a higher temperature depending on the Al_2O_3 content in the mixed TiO_2-Al_2O_3 oxide.

2.5 Conclusion

Mixed TiO_2-Al_2O_3 oxide films have been successfully deposited by sputtering method using a double ring magnetron. The applied power to the Ti target was fixed and that applied to the Al target was varied to obtain a mixed oxide with different refractive indexes combining the desirable properties of two different oxides, TiO_2 and Al_2O_3. The chemical composition in the co-sputtered TiO_2-Al_2O_3 was determined by XPS, which excludes the presence of other contaminants, such as carbon.

The laser reflectometry method has been used as a powerful in-situ measurement for extracting the optical properties at one wavelength 532 nm and the deposition rate of the mixed oxide. A complementary ex-situ ellipsometric spectroscopy has allowed the determination of the optical properties over the visible range 350-850 nm and the layers' thickness. The obtained refractive index at 532 nm can be described by the Bruggeman effective medium approximation.

Deposited periodic alternating multilayers with mixed TiO_2-Al_2O_3 oxide films and SiO_2 films on glass present a high reflectivity peak situated in the visible range at approximately 550 nm. The peak intensity is controlled by varying the fraction of Al_2O_3 in the mixed TiO_2-Al_2O_3 oxide film, the thickness of the films and the number of layers. Increasing the Al_2O_3 content in the TiO_2-Al_2O_3 and the layers number increases the visible reflectance while the solar transmission drops. The best solar transmission obtained was 86.3% for a 3-layered sample. The visible reflectance was 23.5% with a saturated green colour. We have demonstrated the effect of incidence angle on the solar transmission and visible reflectance. Ageing tests showed their stability and their resistance to heat treatments under air up to 450°C.

REFERENCES

[1] L. Martinu, D. Poitras, J. Vac. Sci. Technol. A, V. 18, N. 6, (2000) 2619
[2] J. Boudaden, R.S.-C Ho, P. Oelhafen, A. Schüler, C. Roecker, J.L. Scartezzini, Solar Energy Materials and Solar Cells, 84 (2004) 225
[3] A. Schüler, C. Roecker, J.L. Scartezzini, J. Boudaden, I.R. Videnovic, R.S-C. Ho, P. Oelhafen, Energy Materials and Solar Cells, V. 89 (2004) 241
[4] N. S. Gluck, H. Sankur, J. Heuer, J. DeNatale, W.J. Gunning, J. Appl. Phys. 69 (1991) 3037
[5] D. Brassard, D.K. Sarkar, M.A. El Khakani, L. Ouellet, Appl. Phys. Lett., V. 84. N. 13 (2004) 2304
[6] P.H. Giauque, H. B. Cherry, M-A. Nicolet, Thin Solid Films, V. 394 (2001) 136.
[7] R. Beyers, J. Appl. Phys., V. 56, N. 1 (1984) 147
[8] J-S. Chen, S. Chao, J-S. Kao, H. Niu and C-H. Chen, Applied optics, V. 35, N. 1 (1996) 90
[9] A. Brunet-Bruneau, S. Fisson, B. Gallas, G. Vuye and J. Rivory, Europto conference on advances in optical interference coatings, SPIE V. 3738 (1999) 188
[10] H. Sankur, W. Gunning, J. Appl. Phys. V. 66, N. 10 (1989) 4747
[11] Z. Jiwei, Y. Tao, Z. Liangying, Y. Xi, Ceramics International 25 (1999) 667
[12] W. Que, Y. Zhou, Y. L. Chan, C. H. Kam, Appl. Phys. A. 73 (2001) 171
[13] A. Y. Stakheev, E.S. Shpiro, J. Apijok, J. Phys. Chem. V 97. (1993) 5668
[14] A. Schüler, D. Dutta, E. De Chambrier, C. Roecker, G. De Temmerman, P. Oelhafen, and J. - L. Scartezzini, Solar Energy Materials and Solar Cells, V. 90 (2006) 2894
[15] H. Demiryont, Appl. Opt. V.24, N.16 (1985) 2647
[16] X. Wang, H. Masumoto, Y. Someno, T. Hirai, Thin Solid Films V. 338 (1999) 105
[17] M.F. Ouellette, R. V. Lang, K.L. Yan, R.W. Bertram, R.S. Owies, D. Vincent, J. Vac. Sci. Technol. A. 9 (1991) 1188
[18] D.A. Shirley, Phys. Rev. B. 5 (1972) 4709
[19] J.J. Yeh and I. Lindau, Atomic Data and Nuclear Data Tables 32 (1985) 1
[20] R. Hesse, T. Chassé, R. Szargan, Unifit 2002 - universal analysis software for photoelectron spectra, Anal. Bioanal. Chem. 375 (2003**)** 85
[21] See chapter I
[22] D.A.G. Bruggeman, Ann. Phys. 24 (1935) 636
[23] P.H. Giauque, H. B. Cherry, M-A. Nicolet, Thin Solid Films, V. 394 (2001) 136
[24] D-H. Kuo, K-H. Tzeng, C-H. Chien, J. Vac. Sci. Technol. A, V. 21, N.6 (2003) 1996
[25] G.B. Rayner, Jr.D. Kang, Y. Zhang and G. Lucovsky, J. Vac. Sci. Technol. B., V. 20, N. 4 (2002) 1748
[26] L. Martinu, D. Poitras, J. Vac. Sci. Technol. A, V. 18, N. 6, (2000) 2619
[27] A. Belkind, A. Freilich, G. Song, Z. Zhao, R. Scholl, E. Bixon, Surf. Sci. Technology, V. 174-175 (2003) 88
[28] J. Boudaden, P. Oelhafen, A. Schüler, C. Roecker and J. - L. Scartezzini, Solar Energy Materials and Solar Cells, V. 89 (2005) 209
[29] O. Auciello, W. Fan, B. Kabius, S. Saha, J. A. Carlisle, R. P. H. Chang, C. Lopez , E. A. Irene and R. A. Baragiola, Appl. Phys. Lett. 86 (2005) 042904
[30] R. Tomaszek, L. Pawlowski, J. Zdanowski, J. Grimblot, J. Laureyns, Surf. Coat. Technology, V. 185 (2004) 137
[31] J. Breeze, S.J. Penn, M. Poole and N.MCN. Alford, Electronics Letters, V. 36, N. 10 (2000) 883
[32] B. M. Reddy, B. Chowdhury, P. G. Smirniotis, Appl. Catalysis A: General, V.211 (2001) 19
[33] A. Schüler, J. Boudaden, P. Oelhafen, E. De Chambrier , C. Roecker and J. - L. Scartezzini, Solar Energy Materials and Solar Cells, V. 89 (2005) 219
[34] O.S. Heavens, Optical properties of thin solid films, (New York, 1991)
[35] A. von Richthofen, R. Cremer, R. Domnick, D. Neuschütz, Thin Solid Films, V. 315 (1998) 66
[36] P. Vitanov, A. Harizanova, T. Ivanova, K. Ivanova, J. Mater. Sci. : Materials in Electronics, V. 14 (2003) 757
[37] Y. Kim, S.M. Lee, C.S. Park, S.I. Lee and M.Y. Lee, Appl. Phys. Lett., V.71, N. 25 (1997) 3604
[38] A. Czapla et E. Kusior, Thin Solid Films, V. 214 (1992) 1
[39] P. Vitanov, Tz. Babeva, Z. Alexieva, A. Harizanova, Z. Nenova, Vacuum, V. 76 (2004) 219
[40] D.H. Kuo et K. D. Tzeng , Thin Solid Films, V. 460 (2004) 327

1 General conclusion

The aim of this work is to prove the applicability of the dielectric multilayered samples formed by alternating a first layer with a high refractive index and a second layer with a lower refractive index on glass as a cover to solar thermal collectors. Such a glazed coloured cover is expected to be an adequate solution for a successful architectural integration of solar thermal collectors into buildings.

A large fraction of power from the solar radiation must be transmitted through the coatings. The transparency of the film permits avoiding absorption energy losses within the coating. At the same time, the multilayer films should present a narrow reflection band in the visible range. This selective reflection fixes the colour of the reflected light. A combination of different refractive indexes and thicknesses makes it possible to realise a wide range of reflected colours with an acceptable solar transmission.

Transparent dielectric oxides TiO_2, SiO_2, Al_2O_3 as well as mixed oxides TiO_2-SiO_2 and Al_2O_3 -SiO_2 were deposited by reactive magnetron sputtering. For the deposition of TiO_2, SiO_2 or Al_2O_3 oxides, a circular magnetron capped with metallic titanium, silicon or aluminium targets was used. A ring magnetron capped with an inner target and an outer target was used to sputter mixed oxides.

Several in-situ and ex-situ experimental techniques were used to reach the fixed goal of our project. The photoelectron spectroscopy was an in-situ method to reveal the stoichiometric composition of oxides. In-situ laser reflectometry was employed to determine the refractive index, the extinction coefficient at one wavelength 532 nm as well as the deposition rate of the deposited oxides on silicon samples. Ex-situ ellipsometry was considered as a complementary method to the laser reflectometry to determine the refractive index dispersion in the range 300-850 nm and also the deposition rate. The hemispherical reflectivity and transmission of multilayered samples on glass were measured on the Cary spectrophotometer. For several multilayer films on glass we calculated the colour coordinates in the Lab system.

General conclusion

For a first series of multilayered samples with TiO_2 and SiO_2 layers, our conclusions are:

- The good agreement between the spectroscopic ellipsometry and transmission electron microscopy confirms the feasibility and the control of the multilayer thickness during sputter deposition process.
- The XPS study of the formed interface by sputtering TiO_2 on SiO_2 or SiO_2 on TiO_2 gave an estimation of the formed interfacial zone between TiO_2 and SiO_2 oxides, which is less than 1 nm for both systems TiO_2/SiO_2 and SiO_2/TiO_2. Once the interface is formed a layer-by-layer growth is observed.
- The ageing properties of the 5-layered TiO_2/SiO_2 films show a good resistance and lifetime stability at elevated temperature up to 550°C in atmospheric air.
- 5-layered samples $TiO_2/SiO_2/TiO_2/SiO_2/TiO_2$//Glass having a higher solar transmission between 85-88% and a pronounced visible reflectance between 20-40% were realised.
- The high refractive index difference makes it possible to use a low number of layers, but results in a broad reflectivity peak.

For a second series of multilayered samples with Al_2O_3 and SiO_2 that have been prepared, the following conclusions can be drawn:

- The XPS study of the formed interface by sputtering SiO_2 on Al_2O_3 and Al_2O_3 on SiO_2 revealed that its thickness is less than 1 nm.
- Multilayered samples Al_2O_3/SiO_2 show a higher solar transmission between 88-91%, and an acceptable visible reflectance higher than 12% was realised.
- The lower refractive index difference implies the need of a higher number of layers.
- A disagreement between the measured and expected reflectivity appears to be related to a higher number of layers which implies the need for a higher level of control of the sputtering process
- Ageing tests on 5-layered Al_2O_3/SiO_2 samples showed degradation in their visible reflectance, which is important by increasing the annealing temperature and time. As a consequence, the solar transmission slightly increased.

General conclusion

With a third series of samples consisting of multilayered mixed oxide TiO_2-SiO_2 and TiO_2-Al_2O_3 films, we arrived at the following conclusions:

- Mixed TiO_2-SiO_2 and TiO_2-Al_2O_3 oxides films have been successfully deposited by sputtering method using a double ring magnetron.
- The applied power to the inner targets Si (for TiO_2-SiO_2 mixed oxide) or Al (for TiO_2-Al_2O_3 mixed oxide) was varied to obtain a mixed oxide with different refractive indexes combining the desirable properties of two different oxides.
- A solar transmission higher than 89% and less than 91.4% was obtained for the multilayered TiO_2-SiO_2/SiO_2, which is close to that of uncoated glass (91.9%). The visible reflectance is higher than 11.8%.
- Ageing tests showed the stability of multilayered TiO_2-SiO_2/SiO_2 samples and their resistance to heat treatments under air up to 450°C.
- The best solar transmission obtained was 86.3% for a 3-layered TiO_2-Al_2O_3/SiO_2 sample. The visible reflectance was 23.5% with a saturated green colour.
- Ageing tests applied to multilayered TiO_2-Al_2O_3/SiO_2 samples showed their stability and their resistance to heat treatments under air up to 450°C.

The principal goals reached in this work are therefore:

- the successful use of magnetron sputtering to realize multilayer films using TiO_2, SiO_2, Al_2O_3 and mixed TiO_2-SiO_2 and Al_2O_3-SiO_2 oxides with a high visible reflectance and a solar transmission close to the glass substrate
- the control of the deposition rate and the optical properties
- an acceptable modelling of the optical properties for pure or mixed oxides
- the simulation of the hemispherical reflectivity of the multilayered samples on glass even before experimental realisation

Our project colleagues from LESO-EPFL prepared prototypes of coloured glazing on large solar glass panes (1.90 m x 3 m) by magnetron sputtering with the collaboration

of GLAS TRÖSCH Switzerland. A light blue glazing was cut to measure and for the first installed on a real-sized solar collector [1].

Further developments could be the use of other deposition techniques and other oxides or oxide mixtures. One could think about designing multilayered samples having a graded refractive index instead of a stepped refractive index. The graded refractive index profile decreases the ripples far from the reflected band. A challenge remains in the identification of multilayer designs with nearly angle-independent reflection colours.

[1] A. Schüler et al., Colored Solar Collectors, Phase II: from laboratory samples to collector prototypes, Final report of the SFOE Project-No. 43971, December 2007, http://www.bfe.admin.ch/dokumentation/energieforschung

ACKNOWLEDGMENTS

The completion of this thesis has ultimately been possible with the continued help and support of a number of people, and so to them I owe honest thanks.

I am greatly indebted to Prof. Dr. Peter Oelhafen, my supervisor, for providing valuable guidance, advice and criticism while doing research, writing papers and giving talks. I am extremely impressed by his ability to explain the most difficult subject in a very simple and comprehensible way.

I would like to thank Dr. Andreas Schüler. I am glad I was able to work in a close collaboration with him. He has been a great source of information and his ideas and suggestions have really helped me in my research.

I would like to thank Prof. Dr. Ernst Meyer for his kind acceptance to referee of this thesis.

I am grateful to Dr. Michael Gunnar Garnier and Dr. Teresa de los Arcos for introducing me to photoelectron spectroscopy as well as reactive sputtering deposition.

My thanks go to Roland Steiner for excellent technical facilities in the laboratory, Michael Steinacher, Werner Erni und Bernd Heimann for the electronic support.

I would like to take the opportunity to thank all my friends and colleagues in Basel and in France that have given me support and encouragement during my work.

The financial support of the Swiss Bundesamt für Energie, and of the Swiss National Science Foundation is gratefully acknowledged.

I am also very grateful for the love and support of my family. My children Yasmine and Yanis have been very accommodating in allowing me to work on my thesis. My husband Marc was helping me to get this work completed by his moral support. Finally, I am indebted to my parents and my family for their encouragement.